



TECHNISCHE
UNIVERSITÄT
WIEN

Vienna University of Technology

DISSERTATION

Investigations on structure-property relations of (La,Sr)CoO_{3-δ} thin film SOFC cathodes

ausgeführt zum Zwecke der Erlangung des akademischen Grades einer
Doktorin der technischen Wissenschaften
unter der Leitung von

Univ. Prof. Dr. Jürgen Fleig
E164

Institut für Chemische Technologien und Analytik, Fachbereich Elektrochemie

eingereicht an der Technischen Universität Wien
Fakultät für Technische Chemie

von
Dipl.-Ing. Judith Januschewsky
0226119
Pilgramgasse 22/30, 1050 Wien

Wien, am 22.11.2010

Unterschrift

Contents

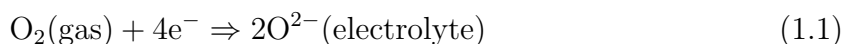
1	Introduction	1
2	Theoretical Aspects	4
2.1	Electrochemical considerations of cathodes in SOFCs	4
2.2	LSC as SOFC cathode material	5
2.2.1	Crystal structure	6
2.2.2	Defect chemistry and oxygen nonstoichiometry	6
2.2.3	Ionic conductivity and electronic conductivity	9
2.3	Preparative methods	9
2.3.1	Pulsed laser deposition (PLD)	9
2.3.2	Sol-Gel	11
2.3.3	Impedance spectroscopy (IS)	12
2.3.4	Transmission electron microscopy (TEM)	16
2.3.5	Atomic force microscopy (AFM)	17
2.3.6	X-ray photoelectron spectroscopy (XPS)	18
3	Experimental	19
3.1	Sample preparation	19
3.1.1	Pulsed laser deposition (PLD)	19
3.1.2	Sol-Gel	20
3.1.3	Micro-structuring	21
3.2	Sample Characterizations	22
3.2.1	AFM and film thickness measurements	22
3.2.2	Scanning electron microscopy (SEM)	23
3.2.3	Transmission electron microscopy (TEM)	24
3.2.4	X-ray diffraction (XRD)	24
3.2.5	Low energy ion scattering (LEIS)	24
3.2.6	X-ray photoelectron spectroscopy (XPS)	24
3.3	Electrochemical Experiments	25
3.3.1	IS measurements	25
3.3.2	Measurements of the electronic conductivity	27
4	Results and Discussion	28
4.1	PLD thin films on single crystalline YSZ	28
4.1.1	Thin film characterization	28
4.1.2	Electrochemical characterization	38

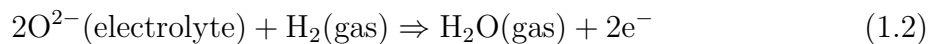
4.1.3	LEIS	57
4.2	Different A and B-site compositions	60
4.2.1	Thin film characterization	60
4.2.2	Electrochemical characterization	61
4.3	LSC thin films on polycrystalline YSZ and GDC	64
4.3.1	Thin film characterization	64
4.3.2	Electrochemical characterization	67
4.4	LSC sol-gel thin films	71
4.4.1	Thin film characterization	71
4.4.2	Electrochemical characterization	75
4.5	XPS measurements	80
5	Conclusions	86
6	List of Abbreviations	89
7	List of Symbols	90
	Bibliography	91
	List of Figures	97
	List of Tables	103
8	Acknowledgment	104
9	Curriculum vitae	106

1 Introduction

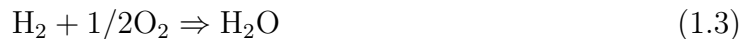
In the last decade technological progress and the change of living standard have increased demands of energy. As fossil fuels and nuclear power are under discussion due to safety reasons and global warming a lot of research in alternative ways of energy conversion has been done. Very promising devices for converting chemical into electrical energy are fuel cells. The first fuel cell was already invented in 1839 by Schönbein and Grove [1]. The basic principle is the direct conversion from chemical to electrical energy, without involving a thermal engine. So, much higher efficiencies not limited by Carnot's law are possible. The principle of a fuel cell is to spatially separate the oxidation and reduction process by an electrolyte, forcing the electrons to flow through an outer circuit. Different types of fuel cells are under investigation but the most important ones are polymer electrolyte membrane fuel cells (PEM), direct methanol fuel cells (DMFC), molten carbonate fuel cells (MCFC) and solid oxide fuel cells (SOFC). They differ in the type of electrolyte (polymer, molten carbonate, solid oxide ion conductor) and/or in type of fuel. Fuels such as hydrogen, methanol or even fossil fuels are possible. The gas at the cathode is normally oxygen or air.

Solid oxide fuel cells (SOFC) have a wide range of possible applications as they allow an efficient, pollution-free and flexible transformation of fuels such as natural gas, hydrogen or biomass into electrical power. The principle of a SOFC with hydrogen as fuel is shown in fig. 1.1. Typical cathode materials are $(\text{La}, \text{Sr})\text{MnO}_{3-\delta}$ (LSM) and other perovskites such as $(\text{La}, \text{Sr})\text{CoO}_{3-\delta}$ (LSC), $(\text{La}, \text{Sr})\text{FeO}_{3-\delta}$ (LSF) or $(\text{La}, \text{Sr})(\text{Co}, \text{Fe})\text{O}_{3-\delta}$ (LSCF), which are often porous or used as composites [2]. As anode composites of metals such as Ni together with YSZ are often used. On the cathode side oxygen is incorporated and the oxygen ions move through an oxygen ion-conducting electrolyte (e.g. yttria stabilized zirconia (YSZ) or gadolinia doped ceria (GDC)) to the anode. The electrons are flowing in the opposite direction in an outer circuit back from the anode to the cathode. The reactions on the cathode and the anode are:





leading to the overall reaction:



However, improvement of efficiency and stability of the cells is still needed and is the aim of numerous research activities. Despite of the higher theoretical (thermodynamic) efficiency at lower temperatures, fast electrochemical kinetics make high operation temperatures (800°-1000°C) necessary. However, stability requirements to interconnect and cell materials cause a strong driving force towards lower operation temperatures. High performance SOFC cathodes operating at temperatures as low as 500°-600°C are thus highly important [3]. Strontium doped lanthanum cobaltite (LSC) and related mixed conducting materials are promising candidates for cathode materials, [2, 4] especially for intermediate temperature SOFCs (500°-700°C). Shortcomings of LSC are its reactivity with yttria-stabilized zirconia (YSZ) at higher temperatures [5] and its high thermal expansion coefficient compared to YSZ. [2] Yet it may be applicable along with ceria-based electrolytes. Further it serves as an excellent model material for investigating electrochemical electrode kinetics [6–8]. In particular, thin film electrodes or microelectrodes have been employed for gaining a more detailed understanding of kinetic processes taking place during oxygen reduction on LSC-electrodes and similar mixed conducting electrodes [6–20]. It is generally agreed that mainly oxygen exchange on the mixed conductor surface determines the total electrochemical electrode resistance of such films [7–9]. However, many questions about the role of the surface structure/chemistry/morphology of LSC and other mixed conductors in oxygen reduction kinetics and thus about the essential structure-property relations remain open. For example, reasons for the degradation of the oxygen exchange rates of film electrodes [8, 21] as well as for drastic voltage activation phenomena [22, 23] are largely unknown. Also the origin of the very different electrode resistances reported for similarly prepared electrodes is unclear. Obviously, further systematic studies are required in order to identify the most relevant parameters determining the oxygen reduction kinetics of LSC and related materials.

In this PhD-thesis, the electrode resistance of thin LSC films prepared by pulsed laser deposition (PLD) on different substrates such as single crystalline YSZ (1 0 0), polycrystalline YSZ and polycrystalline GDC are investigated. A second approach to prepare LSC thin film electrodes was realized by a simple sol-gel route. The increase of

the resistance with time (degradation) at elevated temperatures is investigated in dependence of deposition temperature, film thickness, substrate and LSC composition. Additional XRD, SEM, AFM and TEM measurements determine structure-property relations emphasising the correlation between crystallinity and performance. The surface composition of the thin films was investigated by LEIS and XPS. These experiments revealed that optimising the deposition conditions can lead to thin film electrodes of extraordinary low electrode resistance and little degradation.

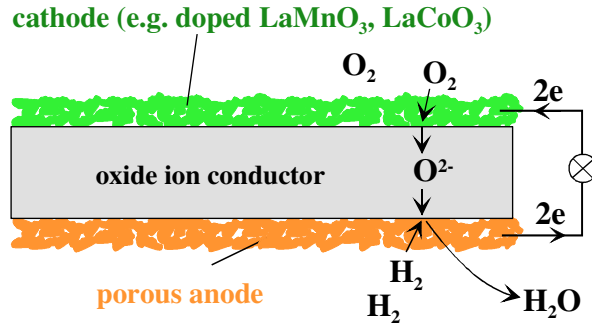


Figure 1.1: SOFC concept-oxygen and hydrogen react via a dense, oxide ion-conducting electrolyte (YSZ or GDC). [24]

2 Theoretical Aspects

2.1 Electrochemical considerations of cathodes in SOFCs

The main goal of this work is to better understand the electrochemical processes taking place when oxygen is incorporated into $(\text{La}, \text{Sr})\text{CoO}_{3-\delta}$ (LSC). Two general mechanisms for the cathode reaction



are the „surface path“ and the „bulk path“ (fig. 2.1). The surface path is the dominant mechanism taking place on pure electronic conductors (e.g. platinum) and often also on materials with mainly electronic conductivity (e.g. lanthanum strontium manganite (LSM)). Following the surface path the oxygen is adsorbed on the cathode surface and diffuses to the three phase boundary. There the oxygen is incorporated more or less directly into the electrolyte together with electrons from the cathode. Subsequently, the oxygen ions migrate through the electrolyte to the anode. A requirement for the bulk path is sufficient oxygen ion conductivity in the cathode material. LSC is a very good oxygen ionic and electronic conductor (=mixed conductor). So the oxygen can adsorb on the surface and be incorporated into the electrode. The oxygen ions diffuse through the cathode passing the electrode/ electrolyte interface and migrate through the electrolyte to the anode. In such cases the surface path still runs in parallel and depending on geometry and material one process usually dominates.

However, this is a very simplified model. The reactions mentioned above include many elementary steps such as oxygen diffusion to the surface, oxygen adsorption on the surface, dissociation of the oxygen molecule, charge transfer and ionization, incorporation of the oxygen species, diffusion through the cathode towards the electrode/electrolyte interface and transport across the interface. Each of these steps has a different kinetics

and the slowest step is the so-called rate determining step (rds). The rate-determining step depends on several parameters such as type of material, geometry and experimental conditions (oxygen partial pressure, temperature etc.). Although a lot of research has been done on different materials the rds is very often not known for a certain system. Also the order of reaction steps and the nature of oxygen species on the surface are still a scope of ongoing research all over the world. [2]

To quantify the processes of the bulk path in the case of mixed conducting cathodes mainly two parameters (k and D) are used, where k refers to the oxygen surface exchange (including adsorption, dissociation, charge transfer/ ionization and incorporation) and D to the oxygen ion diffusion through the material. The exact values of k and D are not only depending on the measured system but also on the measuring method. There are three methods to achieve k and D values: ^{18}O “tracer”, exchange experiments (k^* , D^*), „chemical“ (k^δ , D^δ) and „electric“ methods (k^q , D^q). [25, 26]

Most investigations are performed with porous electrodes, which are often not well defined in geometry. Thin film (micro)-electrodes exhibit the possibility to investigate well defined, model systems where the geometry (of microelectrodes) can easily be adapted to get additional information about the geometry dependence of the rate determining steps.

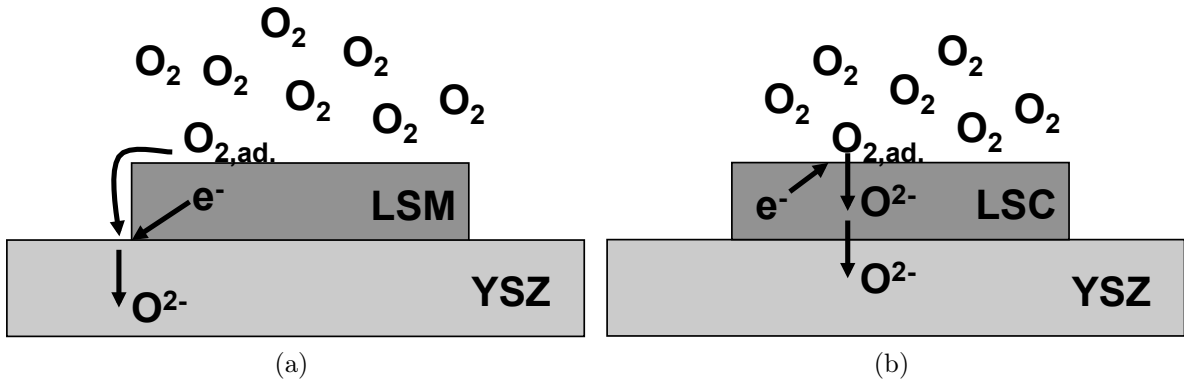


Figure 2.1: Schematic illustration of the surface path (a) and of the bulk path (b).

2.2 LSC as SOFC cathode material

The basic requirement for any electrode material is a high electronic conductivity and its activity towards oxygen reduction. Furthermore stability towards degradation of electrochemical performance and mechanical stability are necessary. Also the reactivity

with the electrolyte such as the zirconate formation between LSC and YSZ [5] has to be taken into account. The mechanical stability is strongly influenced by the differences in the thermal expansion coefficient between electrode and electrolyte. If the difference is large, strain will be induced during heating and cooling of the SOFC that can lead to cracks and final damage.

2.2.1 Crystal structure

Generally LSC crystallizes in a perovskite structure, named after the mineral perovskite CaTiO_3 [27, 28]. The group of ABO_3 perovskite forms a large group used in material science, as by doping and substituting the material properties can be varied over a wide range. The perovskite structure in the simplest case consists of a cube with the A ions on the corners of the cube (fig. 2.2a). The B ion is in the centre of the cube. The ideal cubic-symmetry structure has the B cation in 6-fold coordination, surrounded by an octahedron of oxygen ions, and the A cation in 12-fold cube octahedral coordination. The oxygen ions are at the face centred positions of the cube. The B ion typically is much smaller than the A ion. Perovskites are often distorted, for example when the oxygen octahedron is elongated in one axis. In LSC La is partially substituted by Sr. The stability of LSC increases with La content. $\text{La}_{0.6}\text{Sr}_{0.4}\text{CoO}_{3-\delta}$ (LSC64) at room temperature is rhombohedrally distorted and transforms to a cubic symmetry when heating above 450°C in air. Under reducing conditions an oxygen vacancy ordering occurs forming a brownmillerite phase [28]. The tendency of forming brownmillerite phases decreases with increasing La content [28]. The brownmillerite structure ($\text{ABO}_{2.5}$) is related to the perovskite structure where the BO_6 octahedra of the perovskite phase are alternating with BO_4 octahedra (fig.2.2b) [29]. At higher temperatures the brownmillerite phase transforms to cubic symmetry [28]. Depending on the composition and the oxygen partial pressure LSC at higher temperatures decomposes to Co, La_2O_3 and SrO or to CoO and LaSrCoO_4 [28].

2.2.2 Defect chemistry and oxygen nonstoichiometry

In the following, the defect chemistry of $\text{La}_{1-x}\text{Sr}_x\text{CoO}_{3-\delta}$ will be discussed. In the discussion the Kröger-Vink notation [30] will be used: Capitals denote defect ions or vacancies. The subscript gives information about the location (interstitial or lattice site) of an ion. The superscript is indicating the relative charge with respect to the perfect crystal lattice site. Dashes (|) represent negative charges, dots (•) are used for

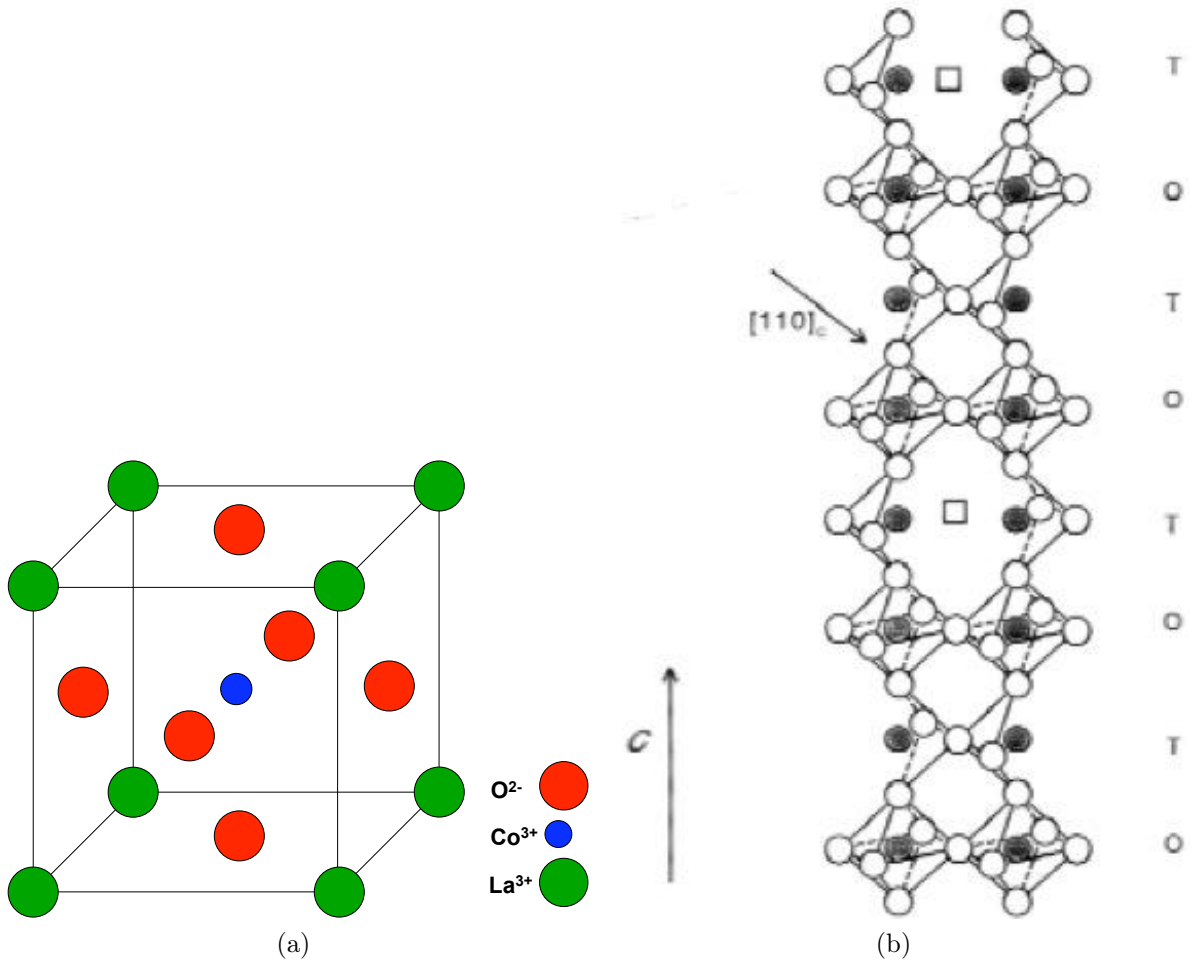
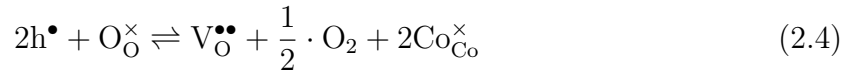
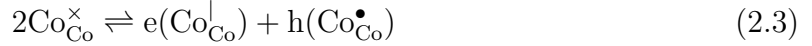


Figure 2.2: a) Perovskite structure b) Brownmillerite structure: Oxygen ions (white) in octahedral (O) and tetrahedral (T) coordination of the Co ions (black). Oxygen vacancies are shown as squares. [29]

positive charges and a cross (\times) is indicating electro-neutrality with respect to the ideal lattice site. An oxygen vacancy in the Kröger-Vink notation is $V_O^{\bullet\bullet}$ while an Sr^{2+} ion on a La^{3+} lattice site having a negative charge relative to La^{3+} is denoted as Sr_{La}^{\prime} . Electrons (e^{\prime}) and electron holes (h^{\bullet}) are written with lower case characters.

The discussion will be restricted to the system $La_{1-x}Sr_xCoO_{3-\delta}$. In lanthanum strontium cobalt iron oxide (LSCF) and lanthanum strontium iron oxide (LSF) Fe^{3+} plays a similar role as Co^{3+} . Defect chemistry not only plays a role in doped materials as there can also be intrinsic disorder in undoped materials. In LSC most defects are generated by doping when substituting La^{3+} with Sr^{2+} on the A-site of the $LaCoO_3$ lattice. In that case charge compensation is required. To regain electro-neutrality the system has two

possibilities. Either by a valence change of Co^{3+} and the creation of holes (electronic compensation) or by the formation of oxygen vacancies (ionic compensation). Normally both processes occur, but which of the compensation mechanisms will be the dominating one depends on oxygen partial pressure and temperature. The reactions in Kröger-Vink notation are the following [31]:



The first reaction will proceed completely as it describes the doping of LaCoO_3 with SrO . The second reaction (disproportionation) and third reaction (oxygen exchange) are in equilibrium. The equilibrium is dependent on the temperature and the oxygen partial pressure.

The most important property of cathodes in SOFC is the reactivity towards oxygen surface incorporation assuming that ion diffusion through the electrode and the oxygen ion exchange on the electrode/electrolyte interface can be neglected. As already mentioned, the oxygen exchange coefficient k can be achieved via several experiments. For mixed conductors with predominant electronic conductivity the values of the electrical (k^q) and tracer diffusion (k^*) experiments are expected to be quite similar. k^{δ} values from chemical experiments are much higher [25]. In ref. [25] a much more detailed discussion of the relation between the different k values is found. From a resistance value obtained in electrical impedance spectroscopy measurements k^q can be calculated according to [26, 32]:

$$k^q = \frac{kT}{4e^2 R_s c_{\text{O}}} \quad (2.5)$$

where k is the Boltzmann constant, T the temperature, e the elementary charge, R_s the area specific resistance and c_{O} the total concentration of lattice oxygen. This concentration can be calculated from the volume of the elementary cell ($6.07 \cdot 10^{-23} \text{ cm}^3$) achieved by x-ray diffraction data and is around $4.94 \cdot 10^{22} \text{ cm}^{-3}$. Assuming a R_s value

of $0.1 \text{ } \Omega\text{cm}^2$ at 600°C a k^a value of about $2 \cdot 10^{-5} \text{ cm/s}$ can be obtained. Kawada et al. [33] for example found values of about $5 \cdot 10^{-5} \text{ cm/s}$ at 800°C .

2.2.3 Ionic conductivity and electronic conductivity

The conductivity σ is in general depending on the concentration of charge carriers (c), the mobility μ and the charge ($z \cdot e$) where e is the elementary charge and z the charge number [24]:

$$\sigma = c \cdot \mu \cdot z \cdot e \quad (2.6)$$

In case of ion-conduction the conductivity often changes with temperature according to the Arrhenius equation:

$$\sigma = \sigma_0 \cdot e^{\frac{-E_a}{k_B \cdot T}} \quad (2.7)$$

where σ_0 is a proportionality factor.

LSC is a mixed conductor, so both electronic and ionic conduction take place. The charge carriers of the electronic conductivity are holes (see chapter Defect chemistry and oxygen nonstoichiometry). In literature electronic conductivities of $1000\text{--}1700 \text{ S/cm}$ between 600°C and 750°C , are found for different LSC compositions [31,34,35]. LSCF has a lower electronic conductivity ranging from 100 to 1000 S/cm in the same temperature range, depending strongly on the iron content. [27,36] The ionic conductivity is several orders of magnitude smaller than the electronic conductivity. Values around 0.3 S/cm at 800°C [37] for LSC46 ($\text{La}_{0.6}\text{Sr}_{0.4}\text{CoO}_{3-\delta}$) are reported. This value is still much higher than the ionic conductivity of the electrolyte YSZ [38].

2.3 Preparative methods

2.3.1 Pulsed laser deposition (PLD)

Pulsed laser deposition is a thin film deposition technique. In this technique a laser beam is focused on a solid target, which should be deposited as a thin film on a substrate (fig. 2.3). The substrate is often heated. In most cases the deposition process takes place in a certain background gas atmosphere, e.g. oxygen if oxides are to be deposited. The main advantage of PLD is the possibility of depositing thin films with a complex stoichiometry. As the energy per pulse implemented in the target is very high no preferential ablation

occurs and the stoichiometry is conserved during the deposition process. PLD is a highly complex method although the set up seems to be quite simple. The interaction of the laser beam with the target involves many different processes. When the target absorbs the laser pulse energy, energy is first converted to electronic excitation and then into thermal, chemical and mechanical energy resulting in emission of atoms/ions, ablation and plasma formation.



Figure 2.3: Image of working PLD.

The PLD process can be divided in different steps: Laser ablation of the target and deposition of the evaporated material on the substrate with nucleation and growth of the thin film. For the last step the most important parameters are the temperature of the substrate, the type and surface quality of the substrate, the pressure of background gas controlling the kinetic energy of the ions and the laser parameters pulse rate and laser spot size on the target, controlling the deposition rate. Further important parameters are the target material and the distance between substrate and target. Generally the whole geometry has an influence on the process and a slight change of the parameters has an impact on the results. The film thickness is proportional to the deposition time for constant deposition rate. Typical deposition rates are about several nm/second. The use of a carousel, housing a number of target materials, enables multilayer films to

be deposited without the need to break vacuum when changing between materials. But as the area of deposited material is also quite small, typically approx. 1 cm^2 , PLD is in general not suitable for industrial mass production. As the method is very complex and involves a lot of parameters deposition of novel materials usually involves a period of empirical optimization of deposition parameters. [39]

2.3.2 Sol-Gel

Sol gel processes are wet chemistry processes employed in a wide range of applications in material science and ceramic engineering. It is often used to prepare metal oxides. Typical precursors are metal alkoxides and metal chlorides, which undergo various forms of hydrolysis and polycondensation reactions. The precursors, a solvent and different additives form the so-called sol. During this process the sol gradually evolves towards the formation of a gel-like system containing a liquid and a solid phase. The consistency can range from discrete particles to continuous polymer networks. The sol-gel process is cheap and can be performed at low temperatures, which allows fine control of the chemical composition of the products. Even small quantities of dopants can be introduced in the sol ending up uniformly dispersed in the final product.

To prepare a film the sol can be either deposited on a substrate via spin coating (fig. 3.2), dip coating or other procedures. It is also possible to cast the sol into suitable molds, for example to obtain fibres or to prepare powders for different applications. Then, during a drying process the remaining liquid (solvent) is removed, typically accompanied by shrinkage and densification of the thin film, form or powder. The rate at which the solvent can be removed is determined by the distribution of porosity in the gel. The microstructure of the final component will be strongly influenced by this phase of processing. In a next step a thermal treatment is often necessary in order to favour further polycondensation, crystallization and grain growth. Mechanical properties and structural stability are improved and again a densification takes place. One of the advantages of sol gel technique is that densification is often achieved at a much lower temperature as during more traditional processing techniques. [40]

Spin coating is a method used to obtain thin films from a liquid solution on substrates. An excess amount of the solution is placed on a fast rotating substrate. The fluid is spread by centrifugal forces over the flat substrate. The higher the rotation speed of the substrate the thinner the film. The thickness of the film also depends on the concentration of the solution and the solvent.

2.3.3 Impedance spectroscopy (IS)

In DC measurements only the total resistance of a system is measurable. But most of the time many different processes such as bulk and grain boundary conduction in electrolytes contribute to the total resistance. In four-electrode arrangements the impact from electrodes can be eliminated by using separated electrodes for current supply and voltage measurement. Today, impedance spectroscopy is a well-established method and the main method for investigating electrochemical resistances and processes in solid state ionics. The first impedance spectroscopic study on a solid electrolyte was performed in 1969, when Bauerle separated bulk, grain boundary and electrode resistances of doped ZrO_2 [41].

By varying the frequency ω over several orders of magnitude, individual resistive processes can be distinguished due to differences in their relaxation times. The word resistance is used in a wide range of meanings. Often a „resistance“ corresponds to chemical reactions and not to an ohmic resistance. The interpretation of impedance spectra can be quite difficult. Mostly an electrical network representation is constructed, which is called equivalent circuit. The simplest case is one RC element (resistance parallel to a capacitance) with the total complex impedance

$$Z_{RC} = \left(\frac{1}{R} + i\omega C\right)^{-1} = \frac{R}{1 + i\omega RC} \quad (2.8)$$

which leads to one semicircle with the diameter R in the complex impedance plane. Every point refers to one certain frequency. The semicircle is formed because at very low frequencies (nearly DC condition) the current goes just through R . At higher frequency the capacitance C is „opened“ and R is short-circuited. The frequency where the current via R and C is equal is the maximum of the semicircle. This frequency is called the relaxation frequency, given by

$$\omega_r = \frac{1}{RC} \quad (2.9)$$

If two different processes have very different relaxation frequencies they appear as two well separated semicircles. This condition is often fulfilled as the characteristic relaxation frequency (e.g. for electrode processes compared to transport across grain boundaries) typically differ by some orders of magnitude in solid-state electrochemistry. The resistance and capacitance of each process can be determined by fitting the semicircles.

Usually measured impedance spectra differ from ideal semicircles. Two semicircles may

have similar relaxation frequencies and overlap or semicircles are depressed. To improve the fit of depressed semicircles the capacitor in the equivalent circuit is replaced by a constant phase element with the impedance:

$$Z_Q = \frac{1}{(i\omega)^n Q} \quad (2.10)$$

For $n=1$ the constant phase element is a perfect capacitance. n values below 0.7 are not reasonable for calculating C . The capacitance with n between 1 and approximately 0.7 can be calculated from the constant phase element by [42]

$$C = (R^{1-n} \cdot Q)^{\frac{1}{n}} \quad (2.11)$$

The interpretation of impedance spectra is often not straightforward. Partly the data are fitted with a suitable equivalent circuit without a real physical meaning. In ref. [43] a very general equivalent circuit describing oxygen exchange and diffusion in mixed conducting electrodes is described (fig. 2.4a). This very complex equivalent circuit was further adapted and simplified in [9] for LSCF (fig. 2.4b and c). In fig. 2.4a the horizontal paths correspond to the conductivity of ionic and electronic charge carriers. The vertical paths indicate reactions. Chemical capacitors reflecting the oxygen stoichiometry changes in the bulk of the mixed conductor electrode connect the electronic and ionic rail. Terminal parts refer to different experimental boundary conditions. Assuming a very high ionic and electronic conductivity (as in LSC) the ionic and electronic rail are shortcircuited. Chemical capacitors are combined to one capacitance C_{chem} . A geometry where the overall reaction is limited by interfacial processes (thin film geometry) leads to a further simplification of the equivalent circuit (fig. 2.4b) [9]. More details are found in ref. [9,43]. For fitting impedance data the double layer capacitor $C_{\text{dl,ion}}$ which is much smaller than the chemical capacitance C_{chem} in many mixed conducting electrodes can be neglected. Further R_b is added to take the contribution of the oxygen ion conduction in the solid electrolyte into account. All capacitances are replaced by constant phase elements Q . The final equivalent circuit is shown in fig. 2.4c.

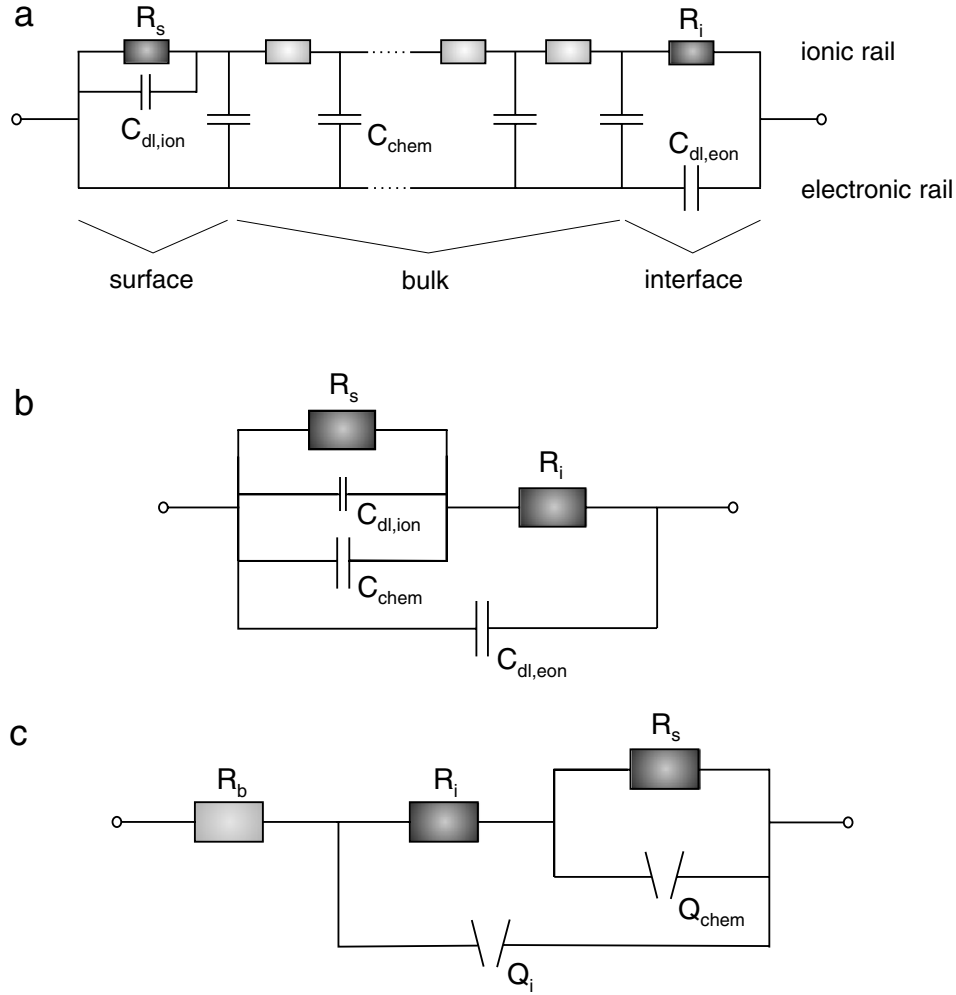


Figure 2.4: Equivalent circuit for a mixed conducting electrode on a solid electrolyte derived (a), simplified circuit (b) and circuit used in this thesis (c). [9]

As already discussed, R_s is the oxygen surface exchange or in cathodic direction the oxygen incorporation process which can be divided into several individual steps such as adsorption and dissociation of the oxygen molecule, ionization and the oxygen incorporation of O^{2-} into a vacancy of the electrode material. From R_s the effective surface exchange rate k^a can be calculated (see formula 2.5 in chapter 2.2.2). In this thesis the surface was removed by chemical etching which resulted in a decrease of R_s . This indicates that R_s is really related to a process taking place on the surface of the electrode. From an electrical point of view, the change of the oxygen content in the electrode bulk is a capacitive process [9]. So it has been referred to as a chemical capacitance C_{chem} [43] and scales with the volume of the electrode. R_i represents the ionic transfer resistance at the electrode/electrolyte interface. The corresponding capacitance C_i is associated

with the interfacial double layer and/or with stoichiometric changes at the interface. In experiments R_b is not only referred to the oxygen ion conduction in the electrolyte but also to the lateral electronic sheet resistance in a thin film and to the resistance between electrical contact (needle or foil) and mixed conducting electrode. [9]

Microelectrodes in impedance spectroscopy

Although a lot of research has been focused on LSC and similar materials the mechanisms of the processes taking place during oxygen exchange are still not well understood. Systems with porous electrodes or consisting of composites are often too complex to separate all the different processes. An approach to obtain further mechanistic information is to simplify the system as much as possible. One possibility is to prepare dense well-defined thin film electrodes via PLD [6,9,11,20,44,45], radio frequency sputtering [46,47] or a sol-gel route [48–53].

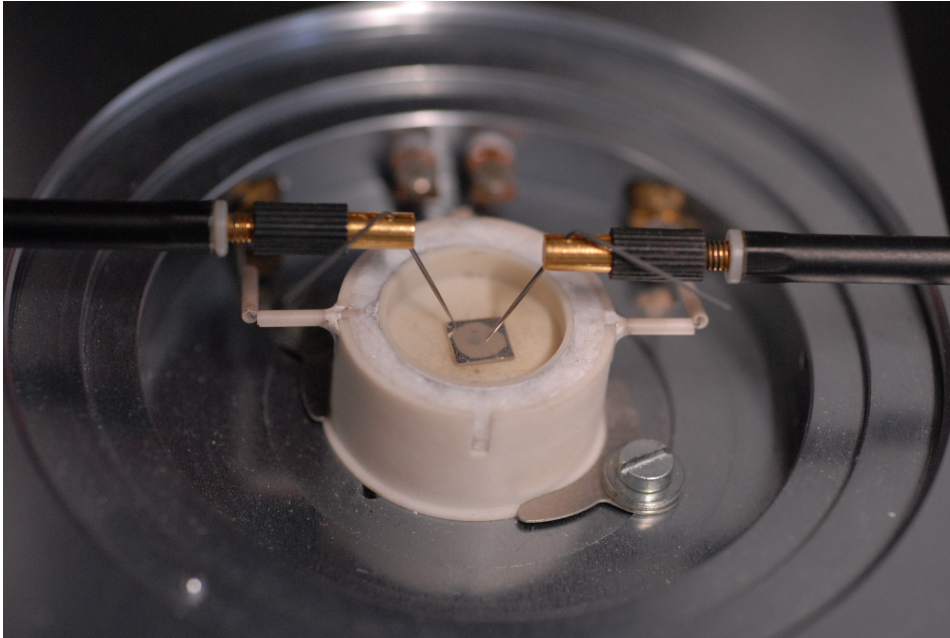


Figure 2.5: Image of a microstructured sample contacted with tips.

These thin films can then be micro-structured for impedance measurements. This provides better statistics, as a lot of identical electrodes can be measured in very short time on one sample. When measuring against a much larger counter electrode the counter electrode has not to be taken into account and only a volume beneath the working electrode contributes to the impedance signal. This is also of advantage if the impedance

is measured under dc bias as the cathode and the anode would not be separable in a symmetric set up.

Another advantage is that the electrode to electrolyte resistance ratio is increased. In the bulk path the electrode resistance scales with the inverse electrode area while the electrolyte resistance between the counter electrode and circular microelectrode is proportional to the inverse microelectrode diameter [24, 54]. Under dc bias the voltage drop at the electrode and in the electrolyte is proportional to the ratio between electrode and electrolyte resistance. As a consequence sometimes polarization measurements are hardly possible with a macroscopic set up but still with microelectrodes.

2.3.4 Transmission electron microscopy (TEM)

Transmission electron microscopy (TEM) is a microscopy technique where an electron beam is transmitted through a thin specimen. The electrons are interacting with the sample and an image is formed. The image is then magnified and focused with electronic lenses onto an imaging device, such as a fluorescence screen, on a photographic film or on a CCD camera. In a TEM different techniques are possible. The most common techniques are bright field (BF), scanning transmission electron microscopy (STEM), selected area diffraction (SAD) analysis and high resolution TEM (HRTEM). In the BF mode the sample is illuminated under a broad electron beam and the transmitted electrons form an image. The image has a thickness and atomic number contrast. HRTEM allows the imaging of the crystallographic structure of a sample at an atomic scale. The contrast arises from the interference of the electron wave with itself in the image plane. For SAD the diffraction pattern is obtained under broad, parallel electron illumination. An aperture in the image plane is used to select the diffracted region of the specimen, so SAD can obtain diffraction information from relatively small volumes. The SAD pattern can be used to identify the crystal structure and the lattice parameters can be determined. Lattice reflections show sharp diffraction spots while nanocrystals give ring patterns. Amorphous materials have SAD patterns consisting of diffuse rings as the lattice parameters are not exactly defined but in a certain range. In the STEM mode the electron beam is scanned with scan coils over the sample similar to SEM. The image is not simultaneous formed on the imaging device as in the former methods. When combined with EDXS and EELS, STEM is a powerful technique for analyzing compositional variations on nanometric to micrometric scales. [55]

2.3.5 Atomic force microscopy (AFM)

Atomic Force Microscope (AFM) was invented from Binnig, Quate, and Gerber in 1985 [56]. The big advantage of AFM in contrast to the already existing STM was the possibility to image nearly any type of surface including those of ceramics, composites, polymers and glasses and not only conducting surfaces.

An AFM consists of a cantilever with a sharp tip at its end, which is used to scan the sample surface. The AFM tips and cantilevers are usually micro-fabricated from Si, SiO₂ or Si₂O₃. Through the interaction of the tip with the sample the cantilever is deflected. The deflection is detected by a laser, which is reflected from the back of the cantilever onto a detector. The force between the tip and sample can then be calculated over Hooke's law from the deflection and the known stiffness of the cantilever. The tip radius determines the resolution, which is in the nm range. The typical lateral resolution is up to 1 nm and up to 0.01 nm in the vertical direction. As the tip scans over the sample surface a three-dimensional image of the surface is achieved. There are different modes used to image the surface of a sample. In the contact mode the tip is always in contact with the sample and electrostatic forces between the electron shell of the tip and the sample reject the tip. During the constant height mode the tip is rejected by the surface structure of the sample. In constant force mode the force between the tip and the sample is kept constant. The force is measured and through a feedback loop the deflection of the cantilever is corrected with piezoelements. With this method the force on the sample is reduced but the scanning speed is lower. In the dynamic or non-contact mode the tip does not contact the sample surface. Instead, the cantilever oscillates at resonance frequency. Forces between the surface of the sample and the tip change this resonance frequency. The change in resonance frequency is the signal used to image the sample. Generally, the non-contact mode is used in vacuum or ultra high vacuum to get the best resolution. In ambient conditions it is difficult to get the tip close enough to the sample to detect short-range forces without getting the tip stuck to the surface. For ambient conditions the tapping mode was invented. It is also a dynamic mode where the cantilever is oscillating at a certain frequency and the cantilever is oscillated closer to the sample than in non-contact mode. Part of the oscillation extends into the repulsive regime of forces, so the tip intermittently touches or „taps“ the surface of the sample. The advantage compared to the contact mode is that the sample surface is less damaged. [57]

2.3.6 X-ray photoelectron spectroscopy (XPS)

XPS is also known as Electron Spectroscopy for Chemical Analysis (ESCA). It is a method for investigating the surface composition and the chemical and electronic states of the elements. The sample surface is irradiated with a monochromatic x-ray beam and all photoelectrons emitted from inner shells are detected. The spectrum recorded is the number of electrons versus their kinetic energy. The kinetic energy is characteristic for the element. The fundamental formula is:

$$E_{kinetic} = h\nu - E_{binding} - e \cdot \phi \quad (2.12)$$

where $h\nu$ is the energy of the x-rays, $E_{binding}$ the binding energy of the photoelectron and ϕ the work function. A small shift of the kinetic energy gives information about the chemical and electronic state of the element in the material. The typical information depth of XPS is the top 1-10 nm of the surface region. By varying the angle between the x-ray source and the sample surface the generation depth can be controlled. The surface roughness is certainly a limiting factor to this angle resolution. For depth profiling the surface can be sputtered away with an ion gun between two measurements. Artefacts due to selective sputtering can occur during this procedure. All measurements have to be performed in ultra high vacuum in order to get a minimum error in the detection of the kinetic energy of electrons.

For the peak integration a background subtraction is necessary. Furthermore, every element has a specific relative sensitivity factor (RSF). These factors are known just for well-established materials and often standards have to be prepared and measured for a specific or new material. The procedure of background subtraction, peak integration, quantification with RSF while taking into account also other factors such as full width at half maximums (FWHM), chemical shifts of a single peak, peak shapes, the instrument design and experimental settings make the data analysis very complex and difficult. [58]

3 Experimental

3.1 Sample preparation

3.1.1 Pulsed laser deposition (PLD)

The LSC and LSCF targets used for pulsed laser deposition (PLD) were synthesized by the Pechini method [59]. Solutions of calcined La_2O_3 (Sigma Aldrich) and dried SrCO_3 (Merck) were prepared in diluted HNO_3 (25%). The Co powder (Sigma Aldrich) and Fe powder (Sigma Aldrich) were dispersed in water, and concentrated HNO_3 was added until the metal was dissolved. All solutions were mixed, heated, and citric acid was added to the boiling solution. After evaporation of water, the mixture started to form a viscous gel, which decomposed with further heating in a spontaneous combustion. The powder obtained after the combustion was calcinated for 20 h at 1000°C , isostatically pressed into a pellet (diameter: 1cm, thickness: 0.1 cm), and sintered for another 12 h at 1200°C in air. Targets with the composition $\text{La}_x\text{Sr}_{1-x}\text{CoO}_{3-\delta}$ with $x=0.8, 0.6, 0.4$ and $\text{La}_{0.6}\text{Sr}_{0.4}\text{Co}_y\text{Fe}_{1-y}\text{O}_{3-\delta}$ with $y=1, 0.7, 0.5, 0.3, 0$ were prepared.

Different LSC and LSCF films were deposited on single-crystalline (100)-oriented YSZ substrates (9.5 mol% Y_2O_3 , CrysTech GmbH, Germany) or on pressed, sintered (1200°C , 5 h) and polished polycrystalline 8YSZ (Tosoh) or GDC (10mol% Gd_2O_3 , Treibacher) substrates. The 50 ns laser pulses were supplied by an excimer laser (Lambda Physics, COMPexPro 201), working at 248 nm with a pulse frequency of 5 Hz (fig.3.1). The fluence on the target surface was about 1.5 Jcm^{-2} . The deposition times were varied from 5 to 75 min. As the deposition rate was changing and dependend on uncontrollable parameters, films with thicknesses between 10 and 1000 nm were deposited. A constant flow of oxygen was applied during the deposition providing an oxygen pressure of 0.4 mbar. Different substrate temperatures were used during deposition and varied from room temperature to 730°C . The temperature was monitored by a pyrometer (Heitronics KT, Germany) on the substrate surface. A temperature difference of about 200°C between the furnace set up temperature and the measured pyrometer temperature was

observed in vacuum. The substrate target distance was kept at 3 cm. All samples were cooled down in vacuum (0.001 mbar).

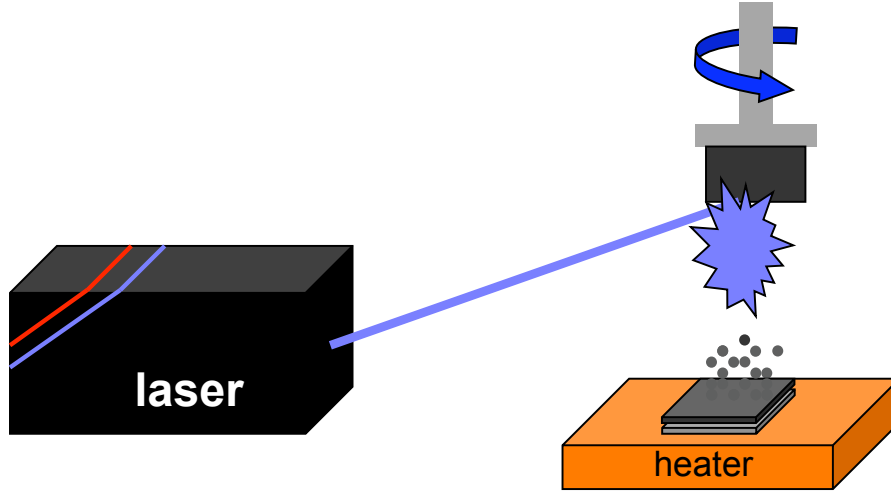


Figure 3.1: Schematic illustration of the PLD process.

3.1.2 Sol-Gel

The LSC thin films were prepared from the starting materials lanthanum acetate $[\text{La}(\text{CH}_3\text{COO})_3 \cdot 1.5\text{H}_2\text{O}]$ (Alfa Aesar), strontium acetate $[\text{Sr}(\text{CH}_3\text{COO})_2 \cdot 0.5\text{H}_2\text{O}]$ (Alfa Aesar) and cobalt acetate $[\text{Co}(\text{CH}_3\text{COO})_2 \cdot 4\text{H}_2\text{O}]$ (Alfa Aesar). The different acetates were mixed in a molar ratio of 1:1:2 and dissolved in glacial acetic acid. The solution was then diluted with glacial acetic acid and either deionized water (1ml for 10 ml solution) or polyvinyl alcohol (140 mg for 10 ml solution) and formamid (0.5 mg for 10 ml solution) to a concentration of 0.27 and 0.3 mol (related to Co). The solution with deionized water was only mixed in an ultrasonic bath but the other solution was heated to 95°C and stirred for about one hour until the polyvinyl alcohol was completely dissolved.

The thin films were then deposited on single-crystalline (100)-oriented YSZ substrates (9.5 mol% Y_2O_3 , CrysTech GmbH, Germany) or on pressed, sintered and polished polycrystalline 8YSZ (Tosoh, Japan) or CGO (10mol% Gd_2O_3 , Treibacher, Austria) substrates by spin coating. 0.1ml of the sol were deposited with 3000 or 6000 rpm for 33 seconds spinning time. A schematic illustration of the process is shown in fig. 3.2. The films were dried at 180°C for 3 minutes, preannealed at 360°C for 3 minutes and finally annealed at 500°C, 600°C or 700°C for another 3 minutes.

For all thin films the procedure of spin coating and heat treatment was repeated in order

to get thicker films. The second layer has to be applied after the whole heat treatment since otherwise the film thickness was not increasing. It seems as if the new sol washes away the old not crystallized sol. This was already reported for LSM thin films from Zhu et al. [60].

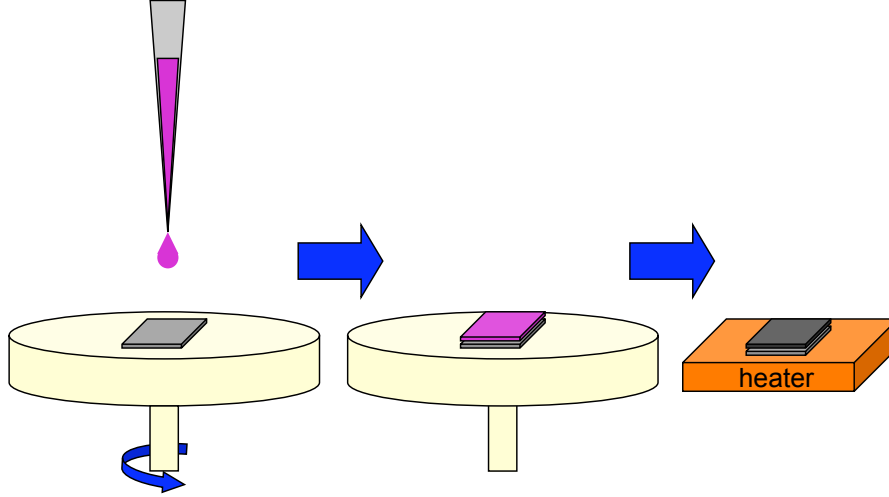


Figure 3.2: Schematic illustration of the sol-gel process.

3.1.3 Micro-structuring

For micro structuring the LSC thin films 60 μl of photo resist (ma-N 1420 negative photo resist, micro resist technology GmbH) was spin coated with 3000 rpm for 33 seconds on the thin films. The photo resist was dried for 2 minutes at 100°C and 80 seconds illuminated by UV-light through a photo mask (Rose Fotomasken, Germany) with circular electrodes (60 μm in diameter). The photo resist was then developed for 60 seconds (developer: ma-D 533 S, micro resist technology GmbH) to remove the unexposed resist. The uncovered parts of the LSC thin film were removed by etching in diluted HCl (0.14 mol/L) (for a few seconds) or with argon ion beam etching (10^{-4} mbar argon, 2 mA argon ions with an energy of 2 keV).

The etching time was determined optically. As this is not a very precise method YSZ was also removed during argon ion beam etching. An over-etching in diluted HCl resulted in a decrease of the microelectrode diameter but no etching of the YSZ occurred in that case. Therefore the micro structuring with chemical etching was also used to determine the film thickness by AFM. After the etching process the remaining photo resist was removed with acetone in an ultrasonic bath. A schematic illustration of the lithography

process is shown in fig. 3.3.

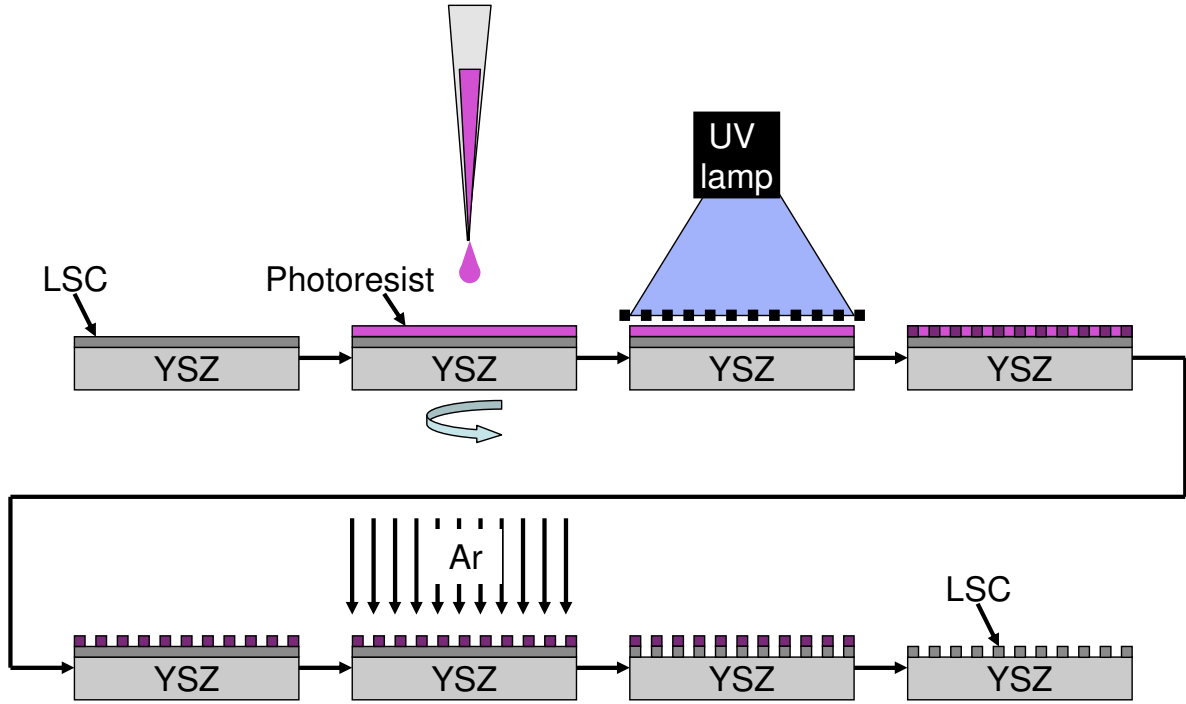


Figure 3.3: Schematic illustration of the photolithography process. As prepared sample; spin coating of the photo resist; illumination under the UV lamp; sample before treatment with developer; sample after treatment with developing solution; ion beam etching; sample after etching; sample after removing the photo resist in acetone.

3.2 Sample Characterizations

3.2.1 AFM and film thickness measurements

Atomic force microscopy (AFM) was performed on a NanoScope III multimode SPM from Digital Instruments (Veeco Metrology Inc.). Measurements were conducted in tapping mode under ambient air using single-crystal silicon cantilevers (Arrow NC cantilevers, NanoWorld, spring constant 42 N/m, resonance frequency 285 kHz), and a J-scanner (maximum scan range $125 \mu\text{m} \times 125 \mu\text{m}$), operating at a scanning rate of 2 or 4 Hz and an imaging resolution of $512 \text{ pixels} \times 512 \text{ pixels}$. The data were evaluated with the NanoScope 6.10b20 software (Digital Instruments, Veeco Metrology Inc.).

For measuring the film thickness PLD thin films were micro structured and chemically

etched. As the substrate was not affected by etching the step height between substrate and LSC surface is the film thickness. By AFM a whole microelectrode was measured and from the cross-sectional view the film thickness can be determined (fig. 3.4a). As the deposition rates of the used PLD-system were unintentionally ranging between 0.2 and 20 nm/min it was very difficult to know the film thickness of every sample. In the end it was possible to find several trends but for more quantitative results better control of the deposition parameters is essential.

For sol gel films etching in HCl could not be used to determine the film thickness as selective etching of the layers appeared (fig. 3.4b). The first layer is already over-etched and the third layer is only partially etched. Therefore the film thickness was determined from the TEM images.

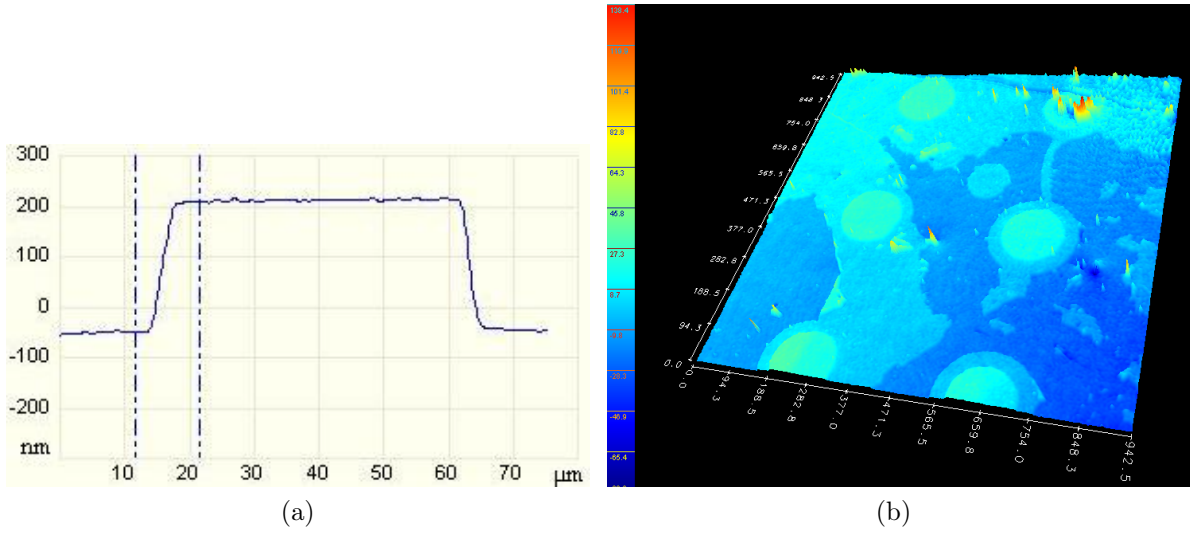


Figure 3.4: Cross-sectional view of an AFM image (a) and digital holographic microscope image of a sol-gel film consisting of three layers after micro-structuring and chemical etching (b).

3.2.2 Scanning electron microscopy (SEM)

For the SEM measurements the thin films were covered by some nm of gold to avoid local charging of the thin films on the at room temperature insulating substrates. The used microscope was a FEI Quanta 200 FEGSEM at USTEM of Vienna UT. The focused ion beam cut was prepared by a FEI Quanta 200 3D DBFIB.

3.2.3 Transmission electron microscopy (TEM)

TEM characterization was performed on a FEI TECNAI F20 (FEGTEM) or a G20 (LaB₆-TEM). Samples were prepared either as cross section FIB lamella (YSZ poly and GDC polycrystal, sol-gel sample) or as cross section specimen by grinding (YSZ singlecrystal). Finally all samples were ion milled.

3.2.4 X-ray diffraction (XRD)

The structure of the prepared LSC powder, the PLD target, and the PLD thin films and sol gel thin films were determined using an X'Pert PRO diffractometer PW 3050/60 (Philips) with Bragg-Brentano geometry and Cu K α radiation. Additional measurements were performed using a D8 DISCOVER diffractometer with a general area detector diffraction system (GADDS) from Bruker.

3.2.5 Low energy ion scattering (LEIS)

The LEIS measurements were performed at IONTOF by Philipp Br uner on a LEIS FE3 with ⁴He⁺ and ²⁰Ne⁺ as primary ions. By means of the helium beam the impurities were detected and for the quantification of the La to Sr ratio the neon measurements were used.

3.2.6 X-ray photoelectron spectroscopy (XPS)

XPS measurements were performed in Prof. Yildiz group at MIT Department of Nuclear Science and Engineering (Cambridge, Massachusetts, USA). For measurements an Omicron EA 125 hemispherical analyzer and Omicron DAR 400 Mg (1253.6 eV) anode non-monochromated x-ray source were used. Measuring was performed in two angles. In the normal angle the analyzer is perpendicular to the sample. When tilting the sample by 60° the sampling depth is only half of the sampling depth in the normal angle (fig. 3.5). So the measurement is more surface sensitive. Information from the first 3 nm (60°) and from the first 6 nm (normal angle) are achieved in this measuring set up. Before the measurement the samples were cleaned by annealing ex-situ in air at 600°C for 1.5 hours in order to remove carbon species from the surface as much as possible.

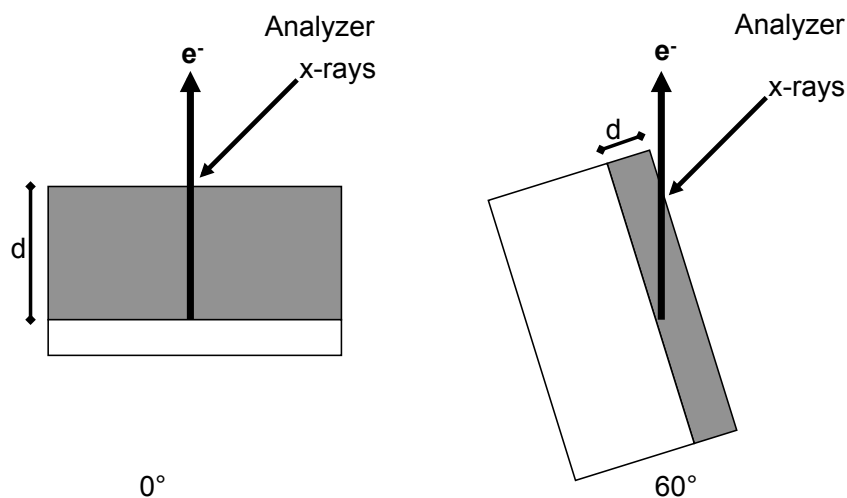


Figure 3.5: Sampling depth in XPS for different angles.

3.3 Electrochemical Experiments

3.3.1 IS measurements

Measurements on microelectrodes

As after the spin coating process a very thick photo resist film remained on the edge of the samples this part of the thin film was also protected from etching and could be used as counter electrodes (CE) for the electrochemical measurements (fig. 2.5). For impedance measurements the sample was placed on top of a heating stage and heated to the desired temperature (400°C to 700°C). Then, one microelectrode (ME) and the large LSC counter electrode were contacted under an optical microscope by gold covered steel needles (EGON, 0.4 mm, Pierkenkemper GmbH, Germany) positioned by micromanipulators (Süss, Germany). The impedance was measured in air using an Alpha-A high performance frequency analyzer (Novocontrol) in the frequency range from $10^6 - 10^{-1}$ Hz with amplitudes of 10 to 20 mV. The real furnace temperature was calculated of single crystalline YSZ and its known conductivity. The formula for calculations was obtained from measurements with platinum electrodes instead of LSC electrodes on the same YSZ substrates to avoid measuring artefact from LSC electrodes [61]. A much better quality of impedance spectra was obtained in closed and more shielded microscopic set-ups (fig. 3.6). Impedance spectra measured in open set-ups were often not fittable.

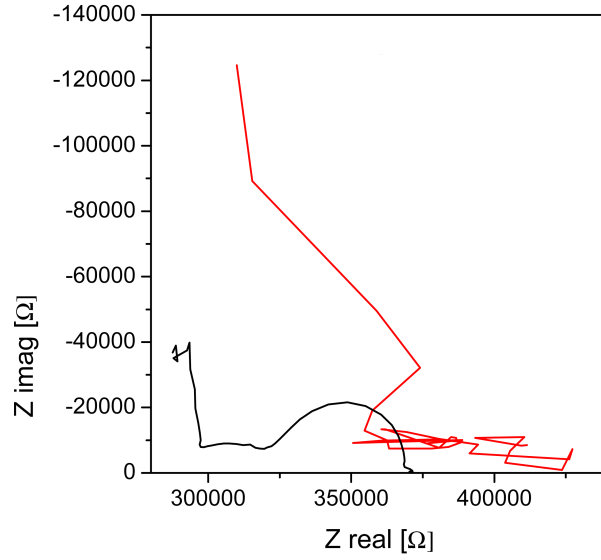


Figure 3.6: Impedance spectra of the same sample recorded at 500°C in an open set-up (red) and a closed set-up (black).

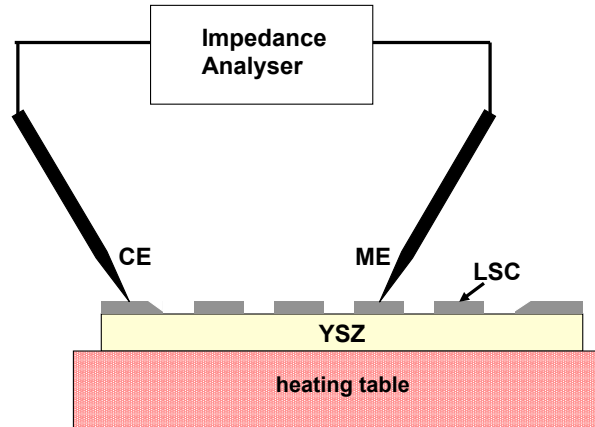


Figure 3.7: Schematic illustration of the microscopic set up.

Macro-measurements

For the macro-measurements YSZ and GDC substrates coated on both sides by LSC electrodes were spring-loaded between two platinum foils in a standard sample holder and placed in an alumina tube furnace.

A schematic illustration is shown in fig. 3.8. Impedance spectra were either recorded using a Phase Sensitive Multimeter 1735 (Newtons4th Ltd.) and a current amplifier (femto, DHPLA-100) or using an Alpha-A high performance frequency analyzer (Novo-

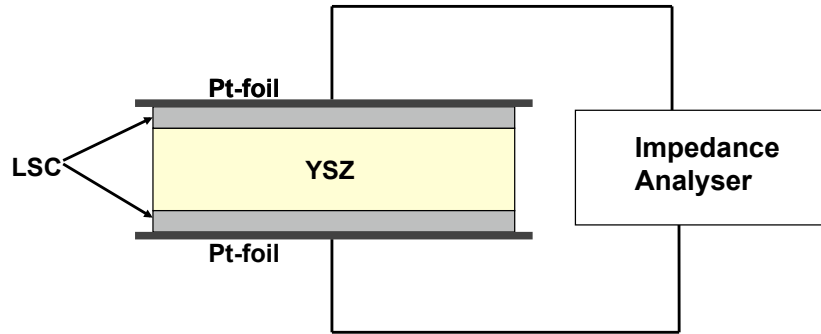


Figure 3.8: Schematic illustration of the macroscopic set up.

control) in the frequency range from $10^6 - 10^{-1}$ Hz with an amplitude of 10 mV. The temperature was measured by a K-type thermocouple.

Due to higher stability of the system the macro-measurements were most useful to investigate the long term behavior of the samples. In the microscopic set-up needles often lost contact with the sample after several hours.

3.3.2 Measurements of the electronic conductivity

The electronic conductivity as a function of temperature between 20 and 700° was determined by the four point van-der-Pauw method [62,63] of E. Bucher in Prof. Sittes group (Montanuniversität Leoben, Austria). A combined precision dc current source/high-impedance multimeter (Keithley model 2400) was used for providing currents and measuring the sample voltage. All experiments were performed with a constant current of 700 μ A. Temperature was adjusted by use of a temperature controller (Eurotherm model 2204e). For data acquisition and instrument control, the software LabView 8.0 (National Instruments, USA) was used.

The samples were fixed to a quartz sample holder by applying small contacts of Ag-paste (dmc2, Leitsilber 200) which also served as electrical contacts for the measurements, at the four corners of the LSC-layers. The sample holder was placed in a quartz apparatus in a furnace (Heraeus, ROF 4/25). The electrical contact between the sample holder and the instruments was established by four Pt-tips. The temperature was measured by a S-type thermocouple placed close to the sample.

4 Results and Discussion

4.1 PLD thin films on single crystalline YSZ

4.1.1 Thin film characterization

XRD

The diffraction patterns (fig. 4.1) of LSC thin films on single crystalline YSZ prepared by PLD show peaks of rhombohedral LSC (pdf 87-1081, R-3c) and cubic YSZ. The large peak at 35.5° and the K_β peak at 31° correspond to the $[1\ 0\ 0]$ direction of the single crystalline YSZ substrate. The LSC thin film deposited at 630°C is crystalline and highly textured. The strongest peak at 33.8° refers to $(1\ 1\ 0)$ index (hexagonal setting).

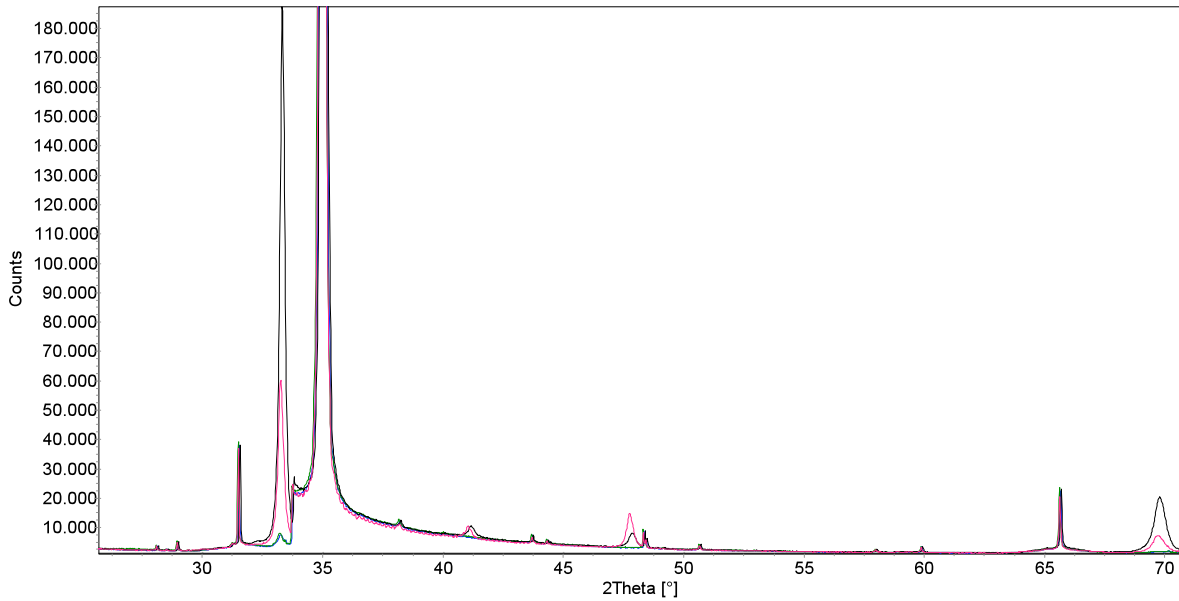


Figure 4.1: X-ray diffraction (XRD) patterns of 200 nm LSC films deposited on single crystalline YSZ at 630°C (red and black) and 470°C (blue and green) before (red and blue) and after (black and green) heat treatment at 600°C for 72 h.

The $(0\ 1\ 2)/ (0\ 2\ 4)$ index at $23^\circ/ 47.7^\circ$ and a further peak at 41.2° ($(2\ 0\ 2)$ index)

were found. All other peaks correspond to the YSZ substrate, which was proven by measurements of a blank substrate. Neither the as prepared nor the samples after heat treatment show any indication of zirconate formation [5]. The heights of the main peak (1 1 0) of the films prepared at 630°C (label a and b) significantly increased after annealing at 600°C for 72 h (b) which indicates that even layers deposited at 630°C are not fully crystalline. The film deposited at lower temperature (470°C) (c and d), exhibits only a very small peak at 33.8° and this peak is not increasing in intensity during the heat treatment (d). The small peak height suggests that the 470°C films exhibit a very low degree of crystallinity and are mainly XRD amorphous or nanocrystalline. Thin films deposited below a temperature of 400-450°C do not show any signal of crystalline LSC in the diffraction pattern. Further crystallographic investigations were performed by TEM with selected area diffraction.

SEM

Fig. 4.2a displays cross sectional and top views of 200 nm thin films prepared at 470°C before and after annealing for 72 hours at 600°C. The same images for a 200 nm thin film deposited at 630°C are shown in fig. 4.2b. In all SEM images a columnar growth of LSC on the YSZ substrate is observable and pronounced differences are neither obvious for different deposition temperatures nor before and after heat treatment. Cracks are not observed and conclusive statements on the existence of pores are hardly possible from these images. The samples deposited at 630°C exhibit an average particle size (diameter of the columns) of about 70 nm while the lower deposition temperature (470°C) leads to smaller particles (ca. 35 nm). The particle sizes did not change significantly during annealing. Information about the grain size within the columnar particles is not available.

The SEM images of a 40 nm thin film deposited at 520°C (fig. 4.3, left) display no significant differences compared to the thicker films. After a heat treatment of 22 hours at 700°C (fig. 4.3, right) crystallites of about 200 nm in diameter have grown on the surface. In SEM images of a 160 nm thick LSC film deposited at 420°C before (fig. 4.4a) and after a heat treatment of 500 hours at 600°C (fig. 4.5a) a growth of crystallites on the surface after this long heat treatment can also be observed. Comparing SEM images of a 270 nm thick LSC film deposited at 650°C before (fig. 4.4b) and after 140 hours at 600°C (fig. 4.5b) a change in the microstructure but no obvious growth of crystallites can be found. The crystallites are not found on any as prepared samples (fig. 4.2a top, 4.2b top, 4.3 left, 4.4).

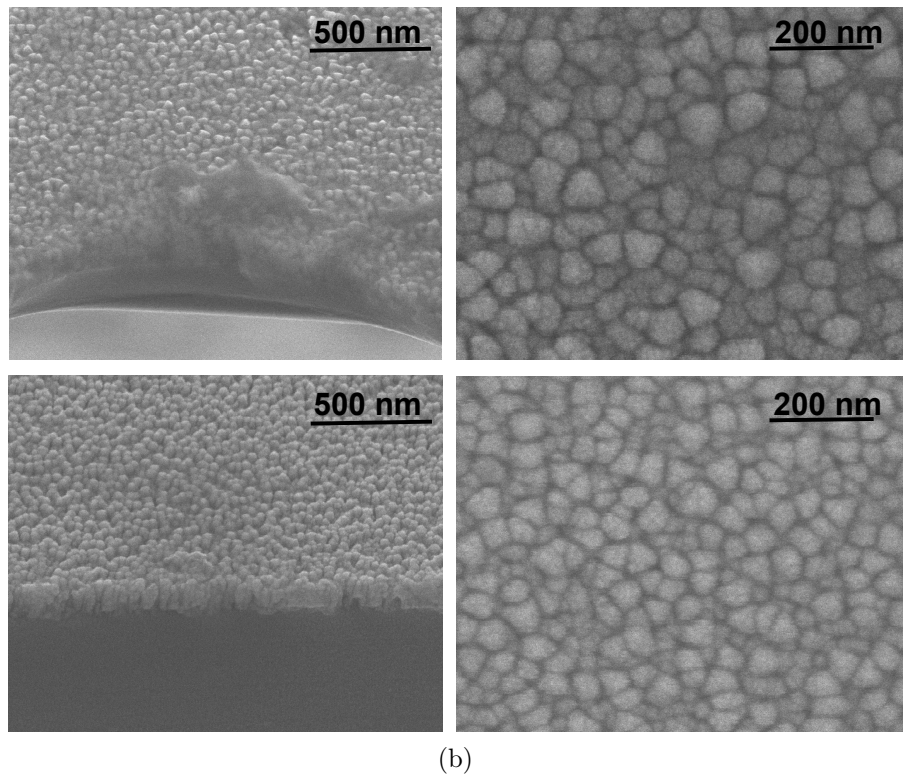
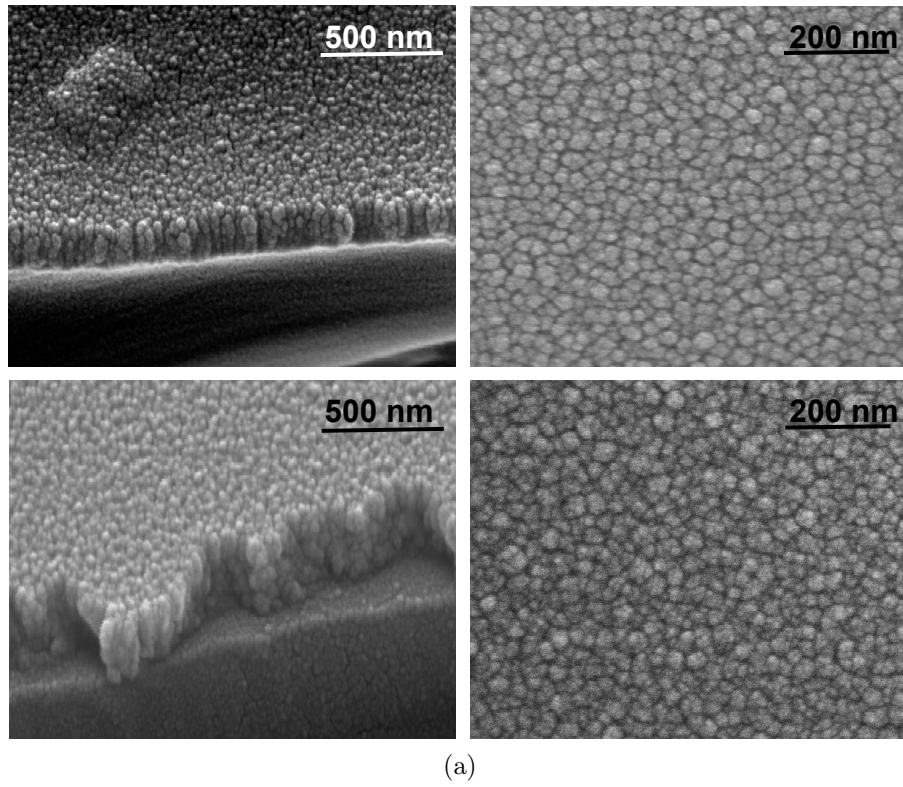


Figure 4.2: a) Scanning electron microscopy (SEM) images (cross-sectional and top views) of 200 nm LSC films deposited at 470°C before (top) and after (bottom) annealing for 72 h at 600°C.
b) Scanning electron microscopy (SEM) images (cross-sectional and top views) of 200 nm LSC films deposited at 630°C before (top) and after (bottom) annealing for 72 h at 600°C.

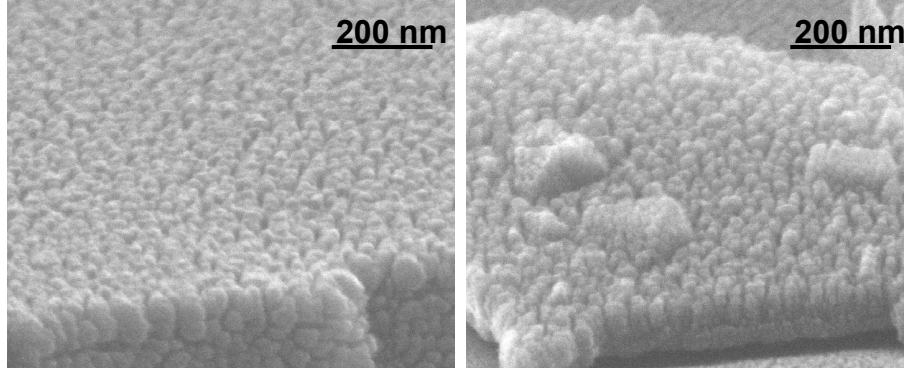


Figure 4.3: SEM images of a 40 nm LSC film deposited at 520°C before (left) and after (right) annealing at 700°C 22 h.

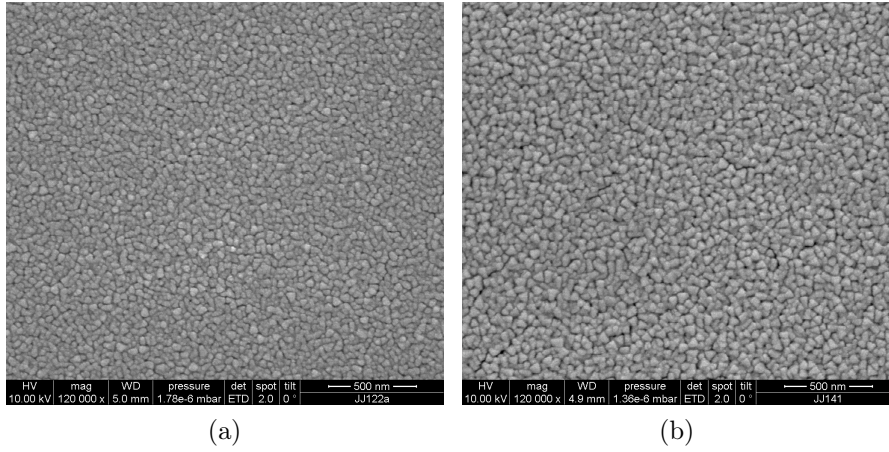


Figure 4.4: SEM images of a 160 nm thick LSC film deposited at 420°C (a) and of a 270 nm thick LSC film deposited at 650°C (b).

The crystallites seem to grow during a heat treatment at 600°C rather soon on very thin samples (40 nm) and much slower on thicker samples (150 nm) after e.g, more than 100 hours of heat treatment. Accordingly the thinner a LSC film is the faster the crystallites grow on the surface. Whether the deposition temperature has an influence on the growth of crystallites is not clear yet.

A FIB cut of a 360 nm thick LSC film deposited at 440°C was prepared and investigated in the SEM (fig. 4.6). In this side view several closed pores and pores along the column boundaries running from the substrate to the LSC surface are visible.

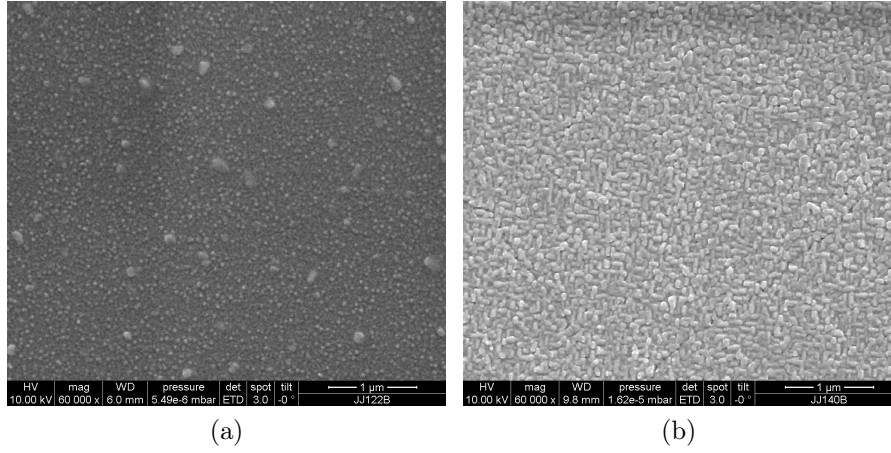


Figure 4.5: SEM images of a 160 nm thick LSC film deposited at 420°C after an annealing of 500 hours at 600°C (a) and of a 270 nm thick LSC film deposited at 650°C after an annealing of 140 hours at 600°C (b).

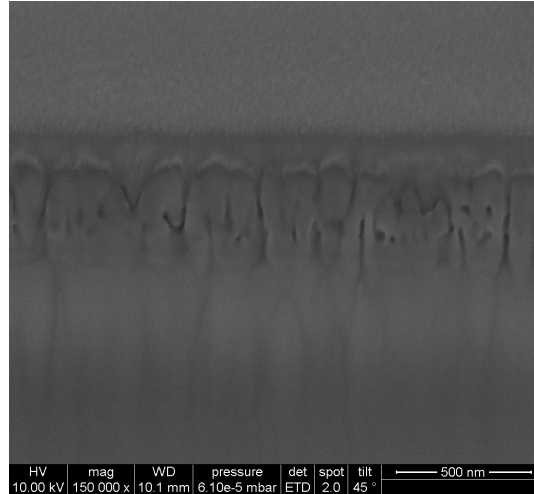


Figure 4.6: FIB cut and cross-sectional view of a 360 nm LSC thin film deposited at 440°C.

AFM

In fig. 4.7a and fig. 4.7b the 3D AFM images of a 410°C and 610°C deposited LSC thin film on single crystalline YSZ are shown. The grains are homogeneously distributed and the surface morphology is in accordance to the findings of the SEM investigations (see chapter SEM). The thin film deposited at higher temperature has larger grains compared to the thin film deposited 200°C lower. The rms roughness is 3.3 nm for the

410°C deposited thin film and 5.9 nm for the 610°C deposited thin film.

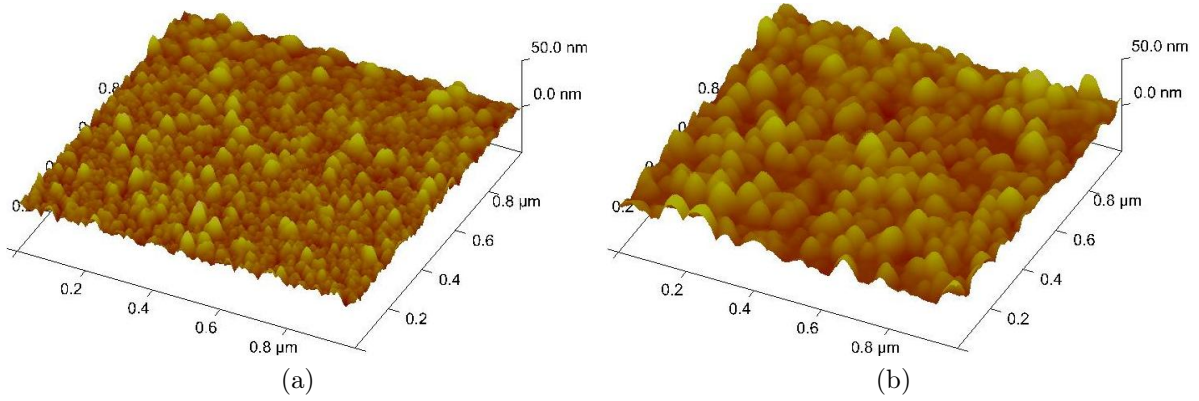


Figure 4.7: 3D AFM image of a PLD thin film deposited at 410°C (a) and at 610°C (b).

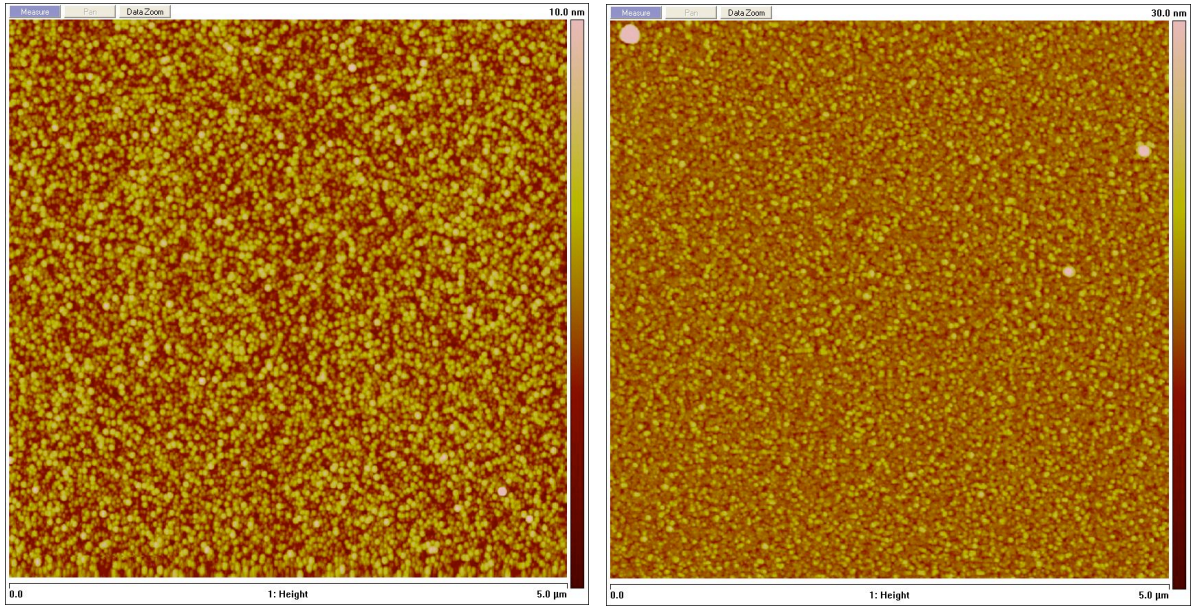


Figure 4.8: AFM images of a 40 nm LSC thin film deposited at 540°C (left) and 730°C (right).

The AFM images of 40 nm thin films deposited at 540°C and 730°C are shown in fig. 4.8. In the AFM image the surface morphology is similar to the images shown in fig. 4.7a and fig. 4.7b. The sample deposited at lower temperature is smoother when taking into account that the vertical scale is only 10 nm compared to 30 nm for the 730°C deposited thin film. In fig. 4.9 the same samples are shown after 20 hours at 700°C. On

the initially smoother surface crystallites have grown during the heat treatment. The height of the larger crystallites on the surfaces are on both samples the same (ca. 50 nm) (fig. 4.10) but additionally a lot of small crystallites were found on the 540°C deposited sample. This growth of crystallites was already observed in SEM investigations (fig. 4.3).

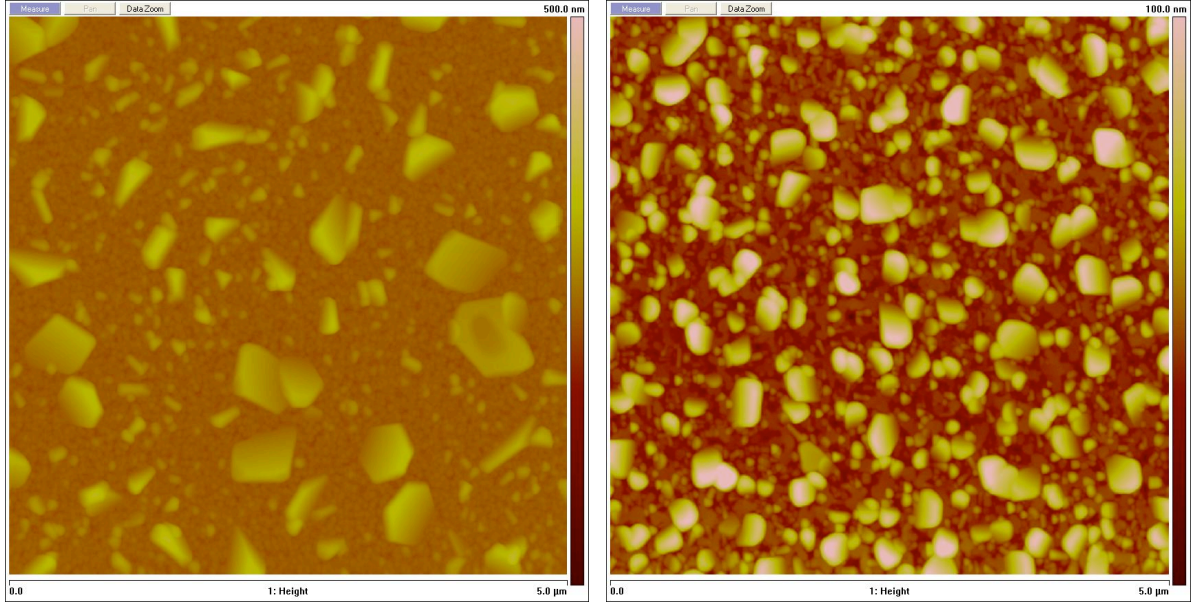


Figure 4.9: AFM images of a 40 nm LSC thin film deposited at 540°C (left) and 730°C (right) after 20 hours at 700°C.

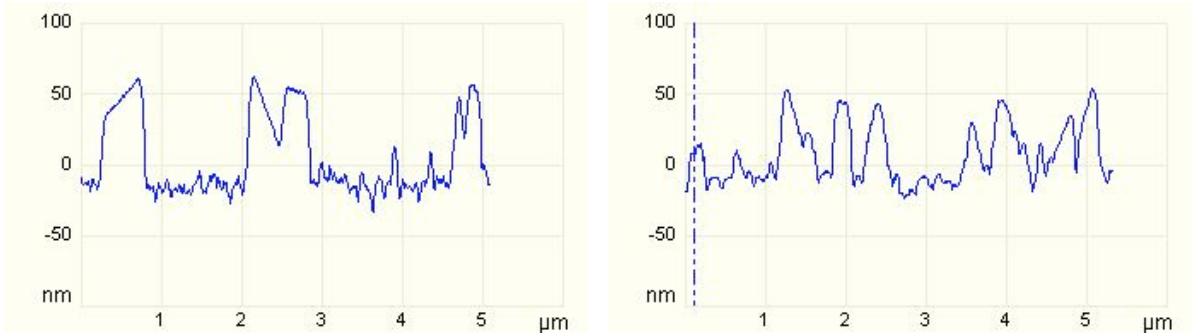


Figure 4.10: Cross section of the AFM images of a 40 nm LSC thin film deposited at 540°C (left) and 730°C (right) both after 20 hours at 700°C.

In all experiments it was never observed that the mismatch in thermal expansion coefficients between LSC and YSZ caused any extended cracks although the samples were

exposed to heating and cooling rates above $130^{\circ}\text{C}/\text{min}$, often several times. The thin films are amorphous or nanocrystalline exhibiting even some pores and this seems to reduce the mismatch or helps the material to avoid cracking. A similar behavior was already observed in literature [64].

LSC thin films deposited at 410°C and 610°C (40 nm) have been polarized by +3 and -3 V for 15 minutes. The corresponding AFM images are shown in fig. 4.11 and 4.12. The electrodes of both samples activated with +3 V exhibit bubbles on the surface. The electrodes deposited at 540°C activated with -3 V show no significant differences compared to the as prepared thin film (fig. 4.8). The changes in the surface morphology will be discussed together with the electrochemical results.

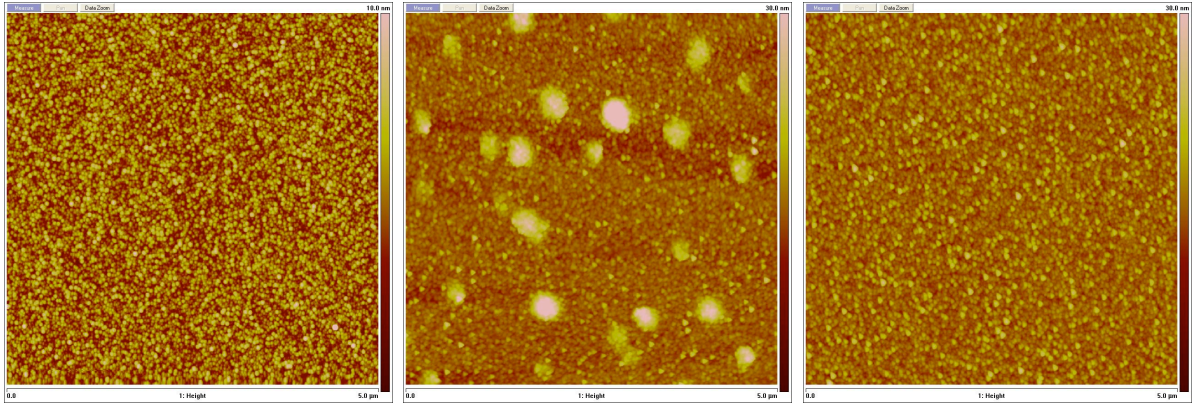


Figure 4.11: AFM images of a 40 nm LSC thin film deposited at 540°C as prepared (left), after +3 V (middle) and -3 V (right) for 15 minutes.

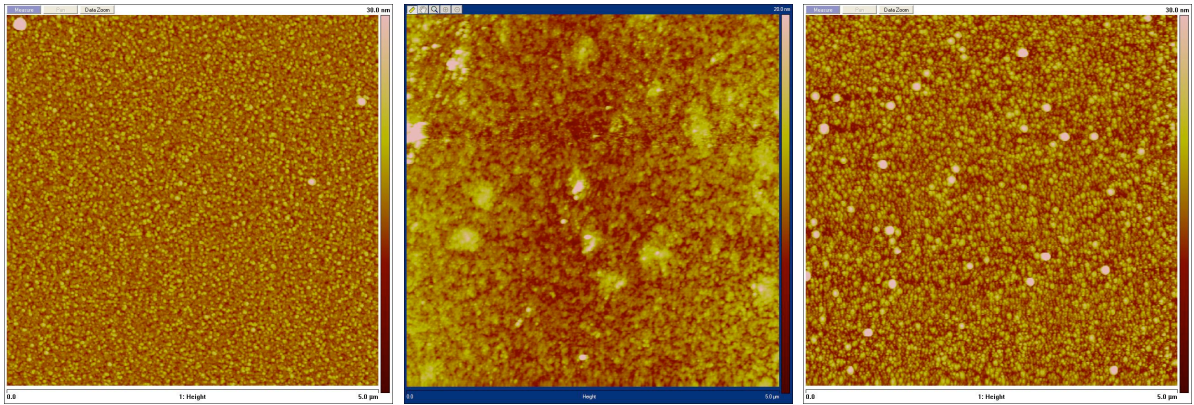


Figure 4.12: AFM images of a 40 nm LSC thin film deposited at 730°C as prepared (left), after +3 V (middle) and -3 V (right) for 15 minutes.

TEM

Fig. 4.13b shows the TEM image at low magnification of a 80 nm thick LSC film deposited at 440°C on single crystalline YSZ. The layer on the top is a protection layer needed for preparation. The thin film surface is quite smooth and the thickness homogeneous. Pores can be found in fig. 4.13b and even more obvious in fig. 4.16a.

In fig. 4.13a a high-resolution TEM image of the same thin film is shown. Most areas of the film are amorphous and only some crystallites with an average size of 10 nm are visible within an amorphous matrix. The diffraction image (fig. 4.14a) of a selected area shows the (1 0 0) diffraction pattern of single crystalline YSZ and a diffuse diffraction ring containing small sharp diffraction spots corresponding to amorphous and randomly oriented polycrystalline regions in the LSC thin film.

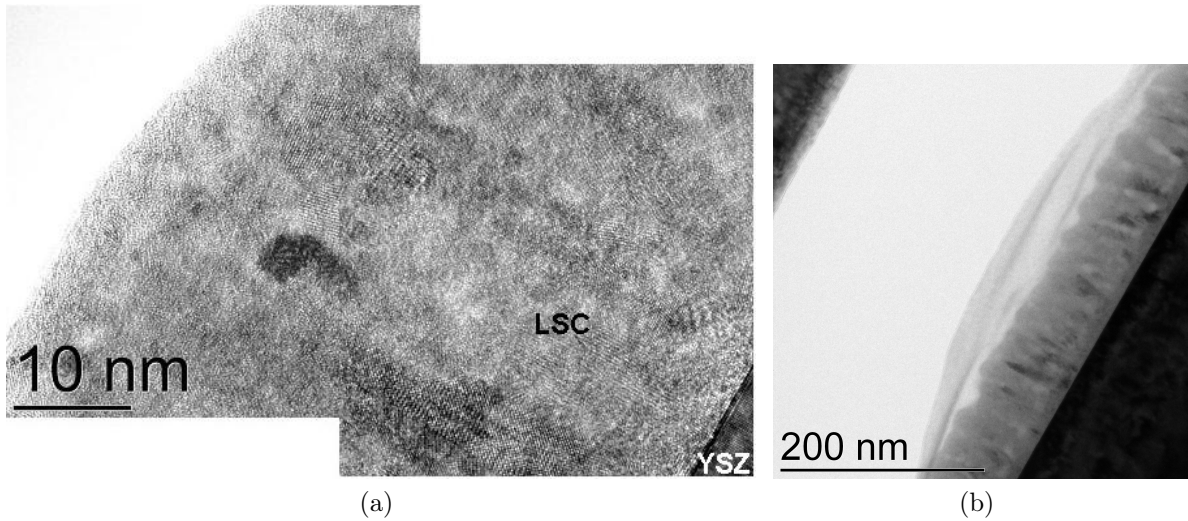


Figure 4.13: HRTEM image (a) and STEM image (b) of a 80 nm thick LSC film deposited at 440°C.

A cross sectional view over a 80 nm thick sample deposited at 720°C (fig. 4.15b) shows a rougher surface compared to the sample deposited at 440°C. The orientation of the YSZ substrate and the LSC thin film are marked with white lines. The film thickness is homogeneous and pores are again observable. In the HAADF STEM image and its integrated profile (fig. 4.16b) pores are even more obvious.

In fig. 4.15a a high-resolution TEM image of the same sample is shown. In the middle of the thin film most of the LSC is crystalline with only small amorphous regions between the crystalline areas. In the selected area diffraction image (fig. 4.14b) only sharp spots corresponding to polycrystalline LSC with a preferential orientation in [1 1 0] direction

and single crystalline $[1\ 0\ 0]$ YSZ are observable. No „amorphous ring“ is found.

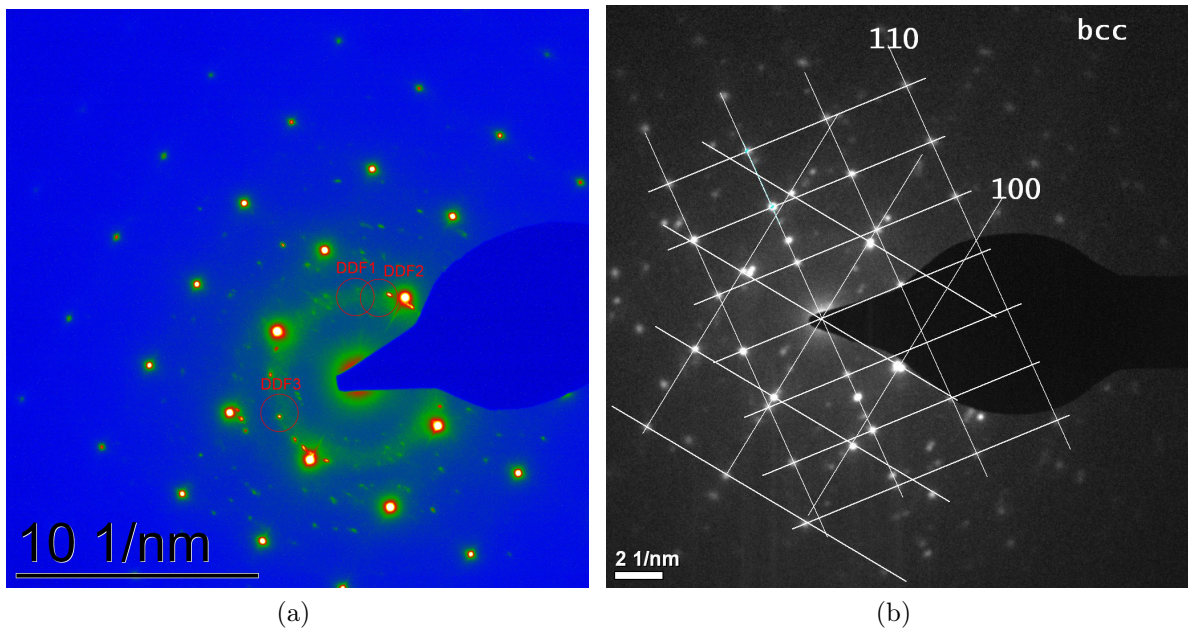


Figure 4.14: SAD pattern of 80 nm thick LSC films deposited at 440°C (a) and 720°C (b).

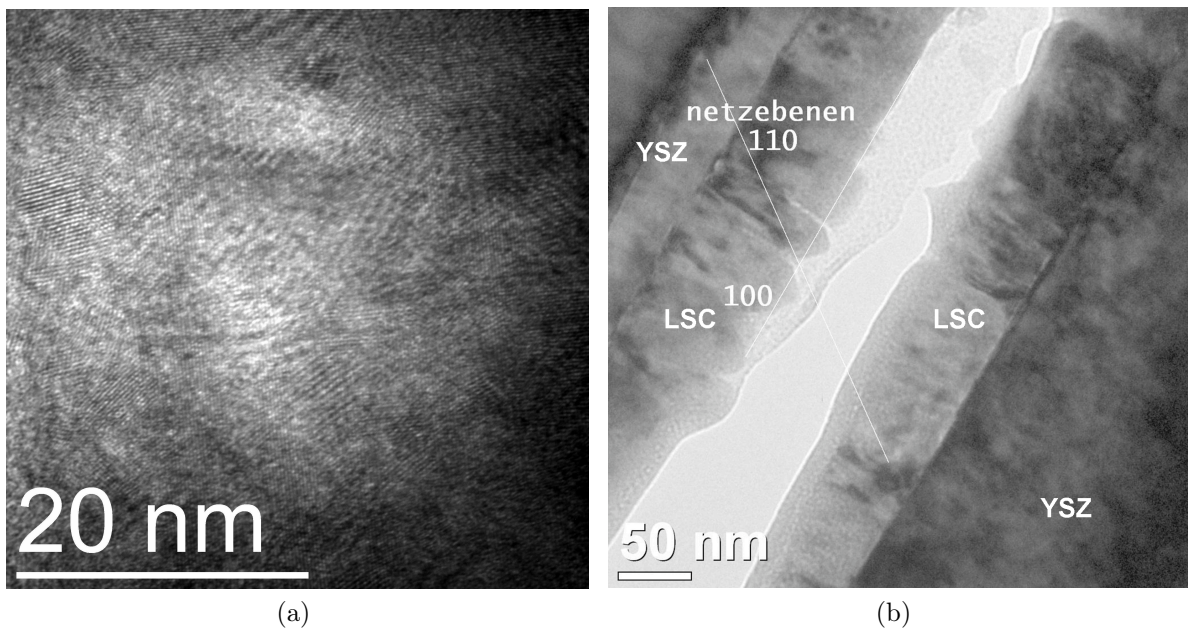


Figure 4.15: HRTEM image (a) and STEM image (b) of a LSC thin film deposited at 720°C.

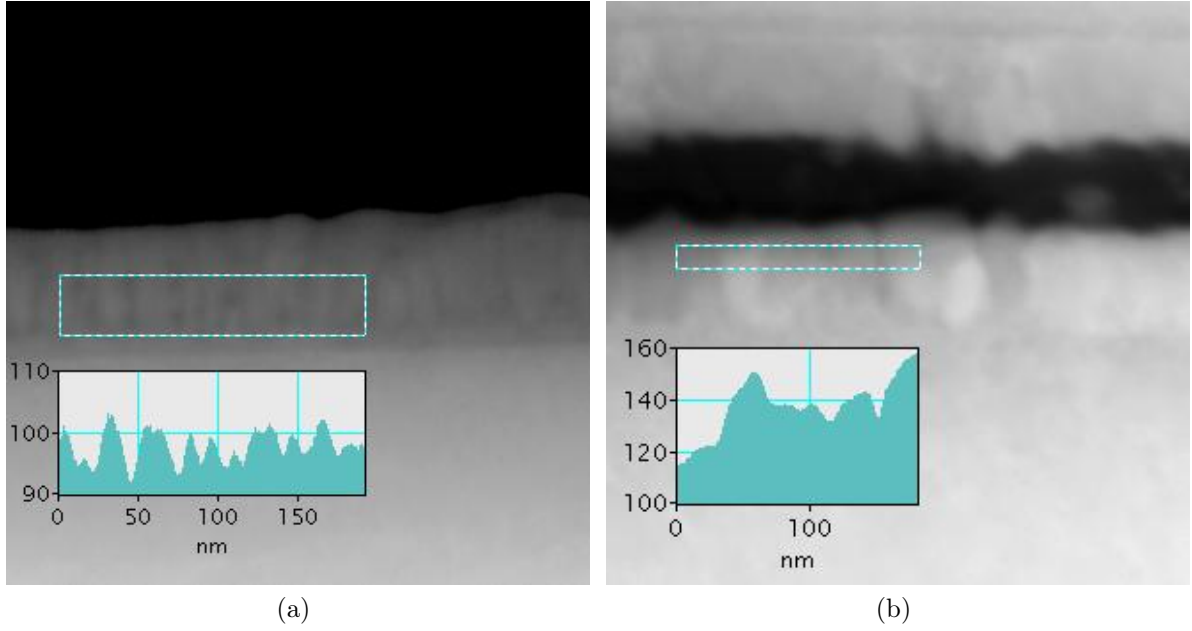
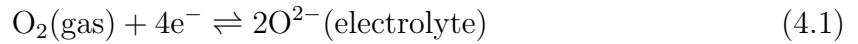


Figure 4.16: HAADF STEM images with profile of 80 nm thick LSC films deposited at 440°C (a) and 720°C (b).

4.1.2 Electrochemical characterization

Impedance spectroscopy

Impedance spectra were measured on single crystalline YSZ covered by two large LSC electrodes (macro-measurements) and on single crystalline YSZ substrates with LSC microelectrodes on one side (micro-measurements), respectively. Spectra (fig. 4.17a) always exhibit a high frequency intercept and a distinct arc at low frequencies, which represents the electrochemical electrode resistance due to oxygen exchange:



Usually electrodes exhibiting higher resistances show spectra consisting of two overlapping semicircles (fig. 4.17b) while electrodes exhibiting smaller resistances show spectra with only one depressed semicircle (fig. 4.17a). In literature a model exists for analyzing the spectra of mixed conducting thin film electrodes in terms of surface and interface processes [9, 16, 65]. Here, however the corresponding equivalent circuit failed to fit the data in case of very small resistances and thus only a total electrode resistance (R_e) was obtained from a fit and will be considered in the further discussion. For all other

electrodes R_e is the sum of all electrode resistances (R_s and R_i). The equivalent circuits used in this study to extract R_e are shown in fig. 4.18b and 4.18c. From the constant phase element Q with impedance

$$Z_Q = \frac{1}{(i\omega)^n Q} \quad (4.2)$$

(ω : angular frequency) the electrode capacitance C was calculated by the formula [42] .

$$C = (R^{1-n} \cdot Q)^{\frac{1}{n}} \quad (4.3)$$

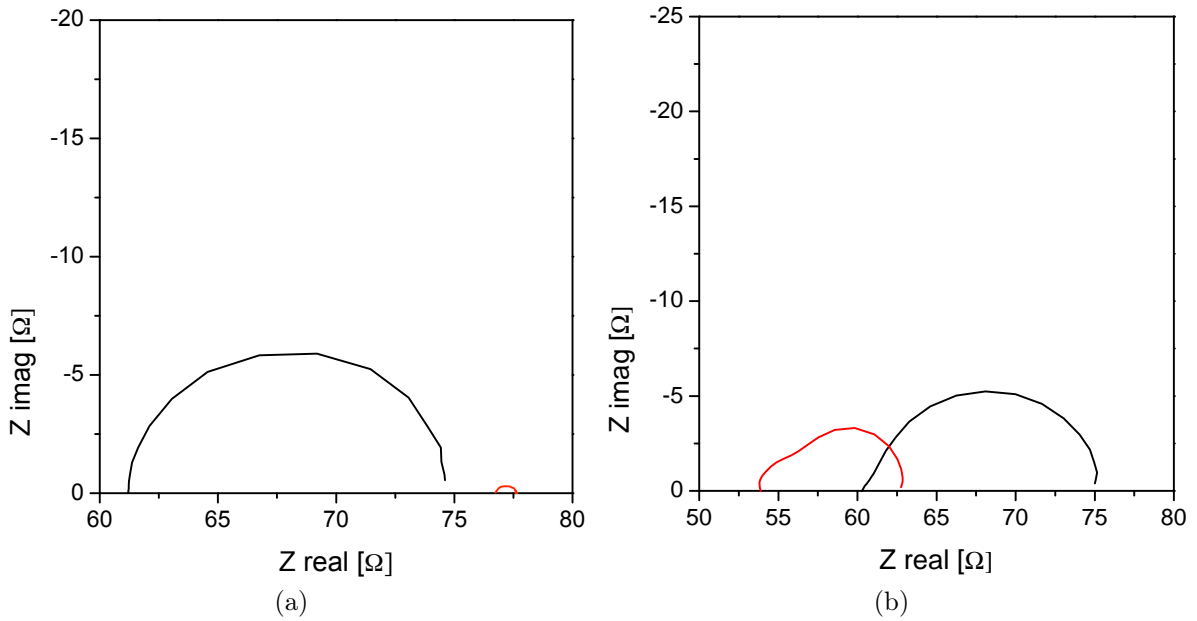


Figure 4.17: Impedance spectra recorded at 600°C on 200 nm LSC thin films deposited at 510°C (red) and 630°C (black) as prepared (a) and of thin films deposited at 500°C (black) and 630°C (red) after several hours at 600°C (b).

In some cases two serial RQ elements were used to fit the electrode response and R_e then corresponds to the sum of the two resistances. As the larger capacitance is the chemical capacitance only this capacitance is measurable in case of only one semicircle. Evaluating impedance spectra of macro-measurements the area-specific electrode resistances were calculated by scaling the total electrode resistance to the area of two electrodes while in micro-measurements only the working electrode significantly contributes to R_e which thus can be directly used for determining the area specific resistance. To prove that

microscopic and macroscopic measurements fit well together, area scaled impedance spectra of a 160 nm thick LSC film deposited at 420°C and measured in both set-ups at 600°C are shown in fig. 4.19.

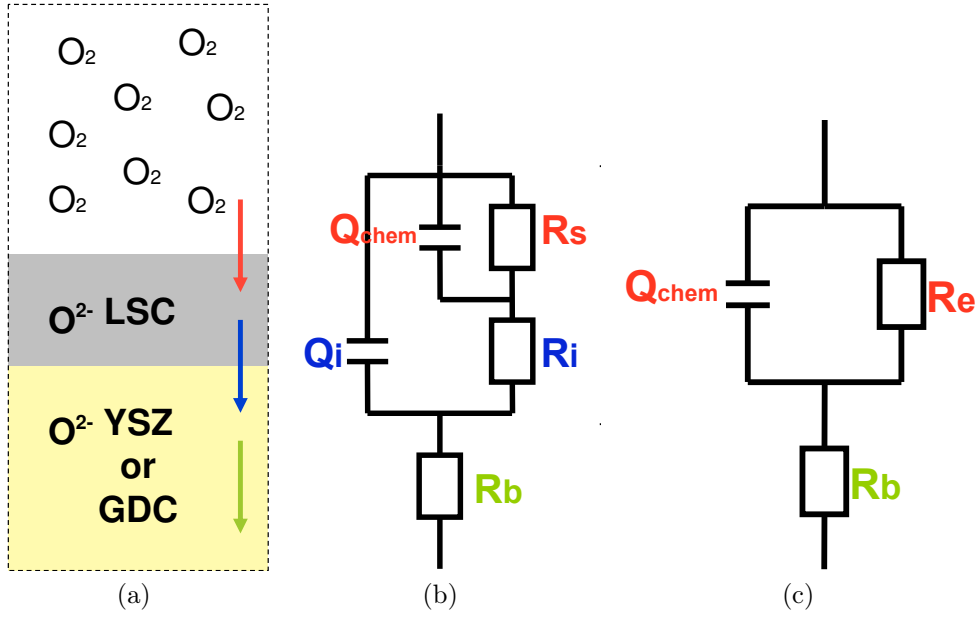


Figure 4.18: a) Schematic illustration of the oxygen reduction on LSC and b) complex and c) simplified equivalent circuits used to fit the data.

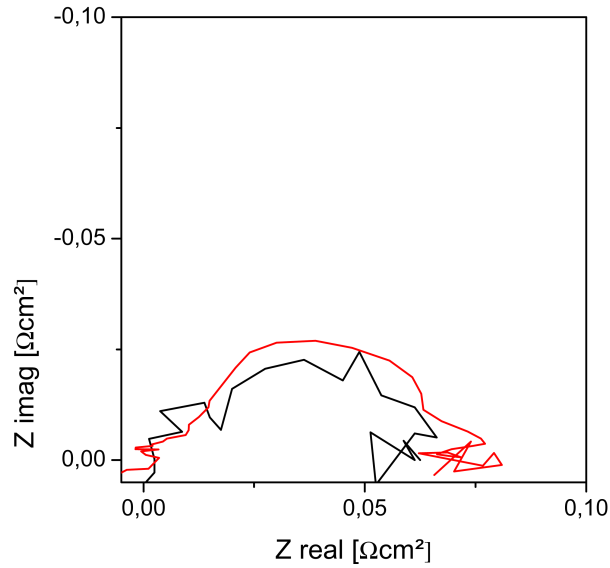


Figure 4.19: Area scaled impedance spectra of LSC electrodes deposited at 420°C measured microscopically (red) and macroscopically (black) at 600°C.

Dependence on deposition temperature and thickness

The normalized electrochemical electrode resistance of the samples strongly depends on the deposition parameters. Values between 0.1 and $24 \Omega\text{cm}^2$ were found for as-prepared samples at 600°C . Deposition temperature and time (and hence film thickness) were varied while all other parameters, such as laser intensity, pulse frequency or oxygen partial pressure, were kept constant. In fig. 4.20 the dependence of the electrode resistance on the deposition temperature is shown for two different film thicknesses. Solid lines are guides to the eye rather than fitting results. The thicker films (200 nm) show impressively low electrode resistances for deposition temperatures in the range of 340°C - 510°C . Films deposited at much lower or much higher temperatures have a significantly higher electrode resistance. For the 40 nm thin films a similar behavior is observed although the resistance values are most of the time higher.

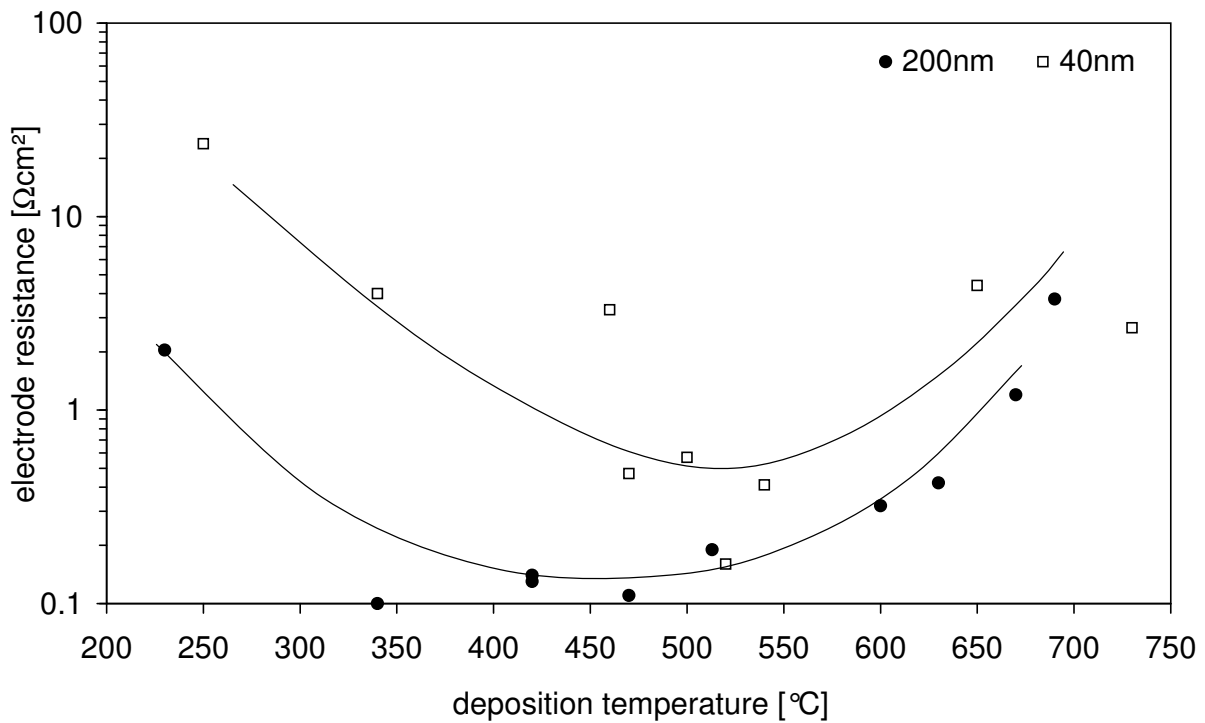


Figure 4.20: Dependence of the electrode resistance at 600°C on the deposition temperature for 200nm and 40nm films. (All measured macroscopically.)

When comparing electrical and structural properties, it becomes evident that thin films exhibiting the lowest electrode resistances were deposited between 340°C and 510°C and thus at temperatures where almost no signal is found in XRD measurements. Accordingly, more or less XRD-amorphous thin films exhibit the best electrochemical perfor-

mance.

Further, it is worth to emphasize that these XRD-amorphous films have electrode resistances of only $0.1 \Omega\text{cm}^2$ at 600°C which is two to three orders of magnitude smaller than resistances reported in literature for LSC films deposited at high temperature [6, 8, 13, 14, 16, 21, 65]. Although these films exhibit some pores in TEM and FIB prepared SEM images, two to three orders of magnitude are not explainable solely by an increase in real surface area.

In Ref. [66] dense LSCF films covered by porous micro-sized LSCF current collectors also showed similar low polarization resistances even though an effect of the LSCF current collector on the low R_e was not explicitly excluded. A much smaller polarization resistance for nano-crystallized than for sub-micron crystallized samples was reported from Sase et al. [14]. Another interesting result reported in literature was an enhanced oxygen surface exchange at heterointerface of $(\text{La}, \text{Sr})_2\text{CoO}_4/(\text{La}, \text{Sr})\text{CoO}_3$ [67]. In Ref. [15] impedance spectra of amorphous LSC and LSM were already measured.

Capacitances

The capacitances of the single electrode arc or of the low frequency arc, in case of two overlapping arcs, exhibit values between $5\text{-}50 \text{ mF}/\text{cm}^2$ at 600°C . The capacitances of intermediate frequency arcs are most of the time not fittable and only very little samples show reliable capacitance values of around $50 \mu\text{F}/\text{cm}^2$ which is in accordance to literature [9]. A difference between microscopic and macroscopic measurements is not observed.

So a few conclusions can be drawn regarding the processes possibly determining the electrode resistance which may be surface processes (R_s), ion transport through the electrode or interfacial processes (R_i) (fig. 4.18a): The capacitance values calculated from the electrode impedances are more or less constant in time and rather independent of the deposition parameters. When normalizing the capacitances of the low frequency arc to the electrode volume they become independent of film thickness and a value of about $2 \cdot 10^3 \text{ F}/\text{cm}^3$ results, which is in accordance with chemical capacitances of LSC films reported in literature [9, 16, 21]. Since a chemical capacitance due to stoichiometry changes only plays a role in case of rate limiting surface reaction or slow ion diffusion through the film, either one or both of these processes contribute to the electrode resistance [43]. As thicker electrodes (200 nm) show similar or even smaller electrode resistances compared to thinner films (40 nm), a diffusion limitation is ruled out. So the surface process seems to determine the total electrode resistance, i.e. the diameter

of the electrode arc.

Activation energy

In order to gain information about the activation energy of electrodes having a rather low electrode resistance, the temperature dependence of several samples deposited between 400° and 470°C were micro- and macroscopically investigated. In fig. 4.21 a sample with two 200 nm LSC layers deposited at 420°C was investigated between 383°C and 582°C. From the slopes of the $\log R_e - T^{-1}$ Arrhenius plot an average activation energy of 1.34 (± 0.06) eV was calculated. The activation energy for a 70 nm thick film deposited at 650°C was also investigated. Four temperature sweeps between 447° and 550°C were performed and the average activation energy was calculated to be 1.77 eV (± 0.30) (fig. 4.22). After 3 days at 600°C an activation energy of 2.43 (± 0.26) eV was obtained (fig. 4.23). However, this activation energy was measured between 770°C and 830°C.

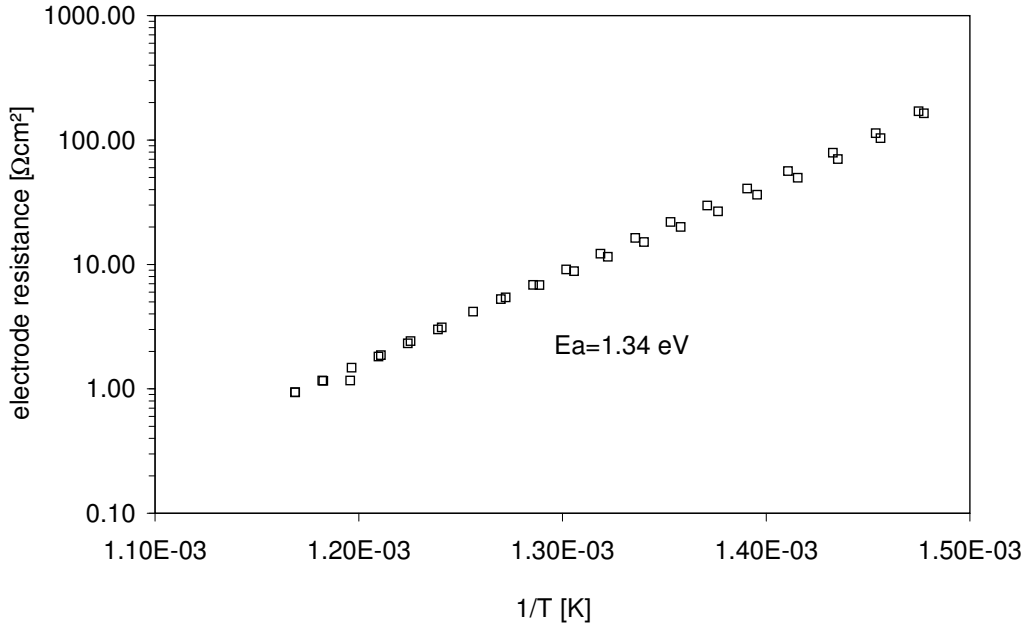


Figure 4.21: Arrhenius plot of a LSC layer deposited at 420°C after 3 days at 600°C; measured macroscopically.

In literature activation energies for LSC thin films of 1.3-1.54 eV [21,68,69] can be found, which is in accordance with the results of the lower deposited thin films. The higher activation energy for the 650°C deposited sample is surprising but for a more detailed discussion the investigation of more samples is necessary to gain more reliable data.

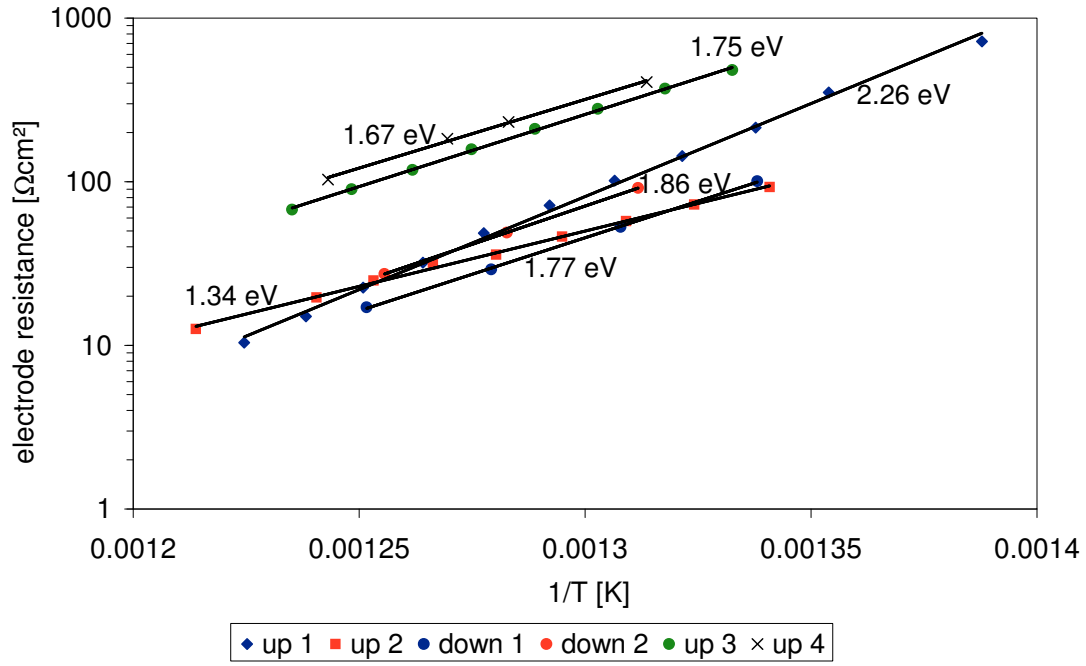


Figure 4.22: Arrhenius plot of a LSC layer deposited at 650°C; measured microscopically.

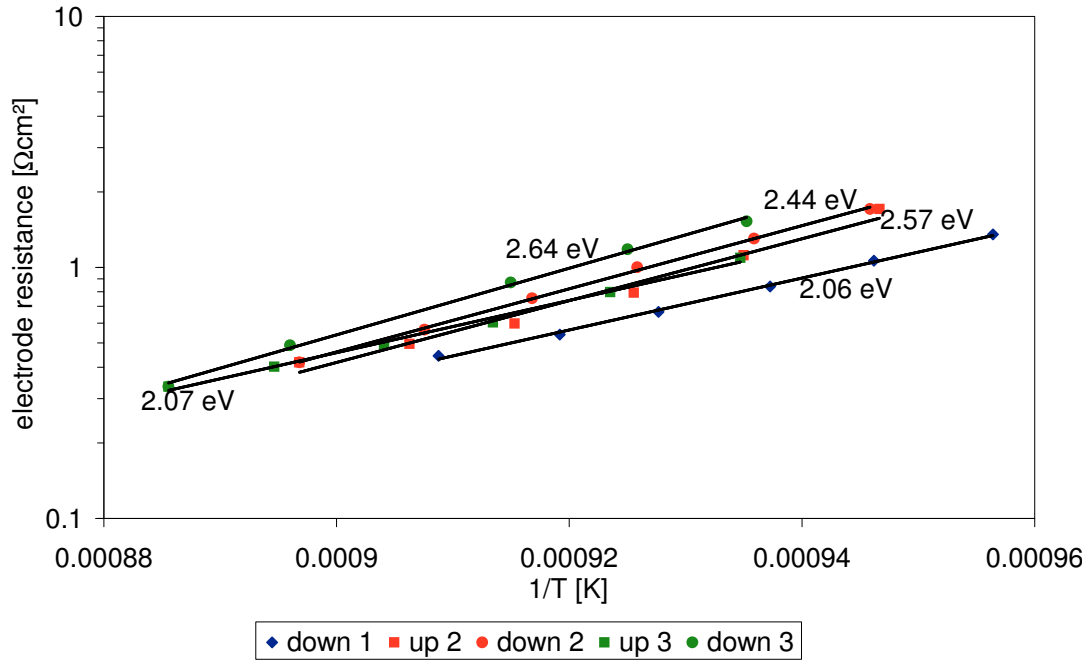


Figure 4.23: Arrhenius plot of a LSC layer deposited at 650°C after 3 days at 600°C; measured microscopically.

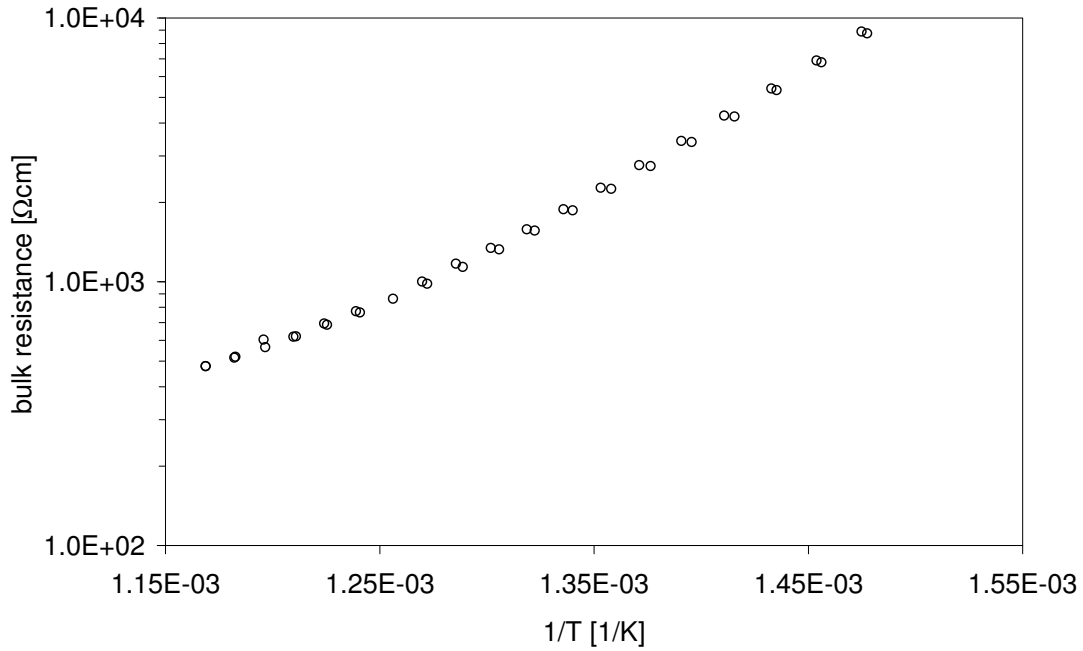


Figure 4.24: Arrhenius plot of YSZ (bulk resistance); measured macroscopically.

The activation energy for YSZ (bulk resistance) was calculated to be $0.99 (\pm 0.18)$ eV in the temperature range between 383°C and 582°C (fig. 4.24), which is in accordance with 0.93 eV, reported in literature [21]. For the capacitances and the interface resistances it was not possible to calculate reliable activation energies due to the low quality of the spectra.

Electronic conductivity and bulk resistance

One could expect that the high frequency intercepts (R_b) of the spectra correspond to the ohmic resistance of oxide ion transport in the electrolyte. In fig. 4.25 R_b for 200 nm and 40 nm LSC films macroscopically measured is shown as a function of deposition temperature. R_b is slightly above the bulk resistance of YSZ obtained from measurements using Pt electrodes. Significantly higher resistance values are found for most 40 nm thin films, especially for those deposited at lower temperatures; also a 200 nm film deposited at 230°C exhibits a large high frequency intercept. The same sample, micro-structured, exhibits a specific R_b value increase by only a factor of 2. In that case the electrode resistance, obtained in micro-measurements, increased by a factor of 2 to 3 compared to the results achieved in macro-measurements. For all other samples measured microscopically no increased bulk resistance was observed.

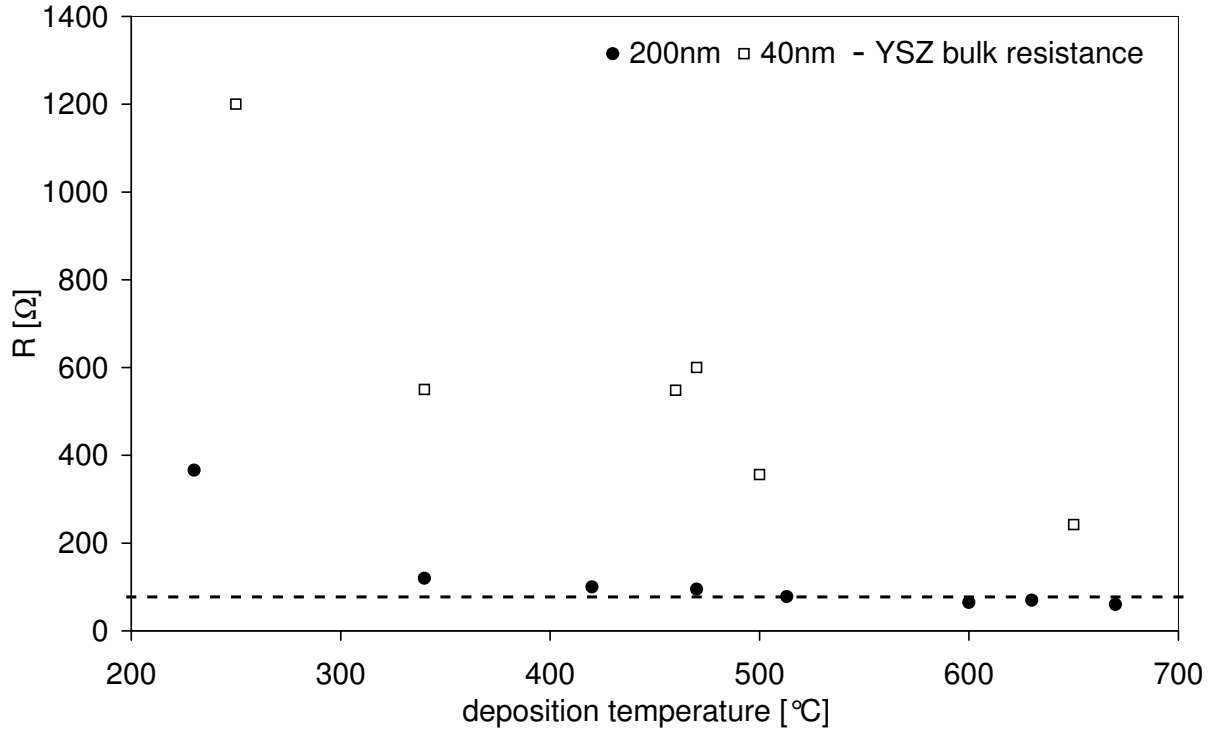


Figure 4.25: High-frequency intercept (R_b) of the impedance spectra in macro measurements at 600°C for 200 and 40nm LSC films deposited at different temperatures.

All strongly enhanced R_b resistances measured macroscopically showed less pronounced temperature dependences compared to the true ohmic resistance of YSZ. The bulk resistance of 420°C deposited samples (shown later in fig. 4.30) changed from 110 Ω at 600°C to 75 Ω at 700°C while the sample deposited at 650°C (fig. 4.31) changed from 80 Ω at 600°C to 22 Ω at 700°C. The increased R_b of 40 nm films and to a lesser extend also of 200 nm films deposited at lower temperatures (fig. 4.25) is most probably caused by the lateral sheet resistance of electron transport in these films. In particular the poor crystallinity of films deposited at low temperatures may reduce the electronic conductivity of LSC. The electron transport from point contacts between film and Pt foil to sites where oxygen is incorporated is thus hindered. This causes an additional (electronic) bulk resistance, which cannot be separated from the YSZ bulk resistance in the impedance spectra. However, it causes an apparently lower temperature dependence of R_b since the electronic conductivity of LSC is less temperature dependent than the ionic YSZ bulk resistance [70]. Similarly, an enhanced lateral resistance due to some porosity would be reflected in R_e .

With three samples (deposited at 340°C, 470°C and 630°C, 320 nm) van-der-Pauw measurements were performed by Prof. Sittes group in Leoben. The results are shown in fig. 4.26. The sample deposited at the highest temperature has the highest electronic conductivity. The lower the deposition temperature, the lower is the electronic conductivity in the thin film. During the measurement of the sample deposited at 470°C the contact between thin film and gold wire broke. So the measurement was only performed up to 400°C. The corresponding electrode resistances of the samples are 0.3 and 0.5 Ωcm^2 for the 340°C and 470°C deposited sample and 5 Ωcm^2 for the sample deposited at 630°C.

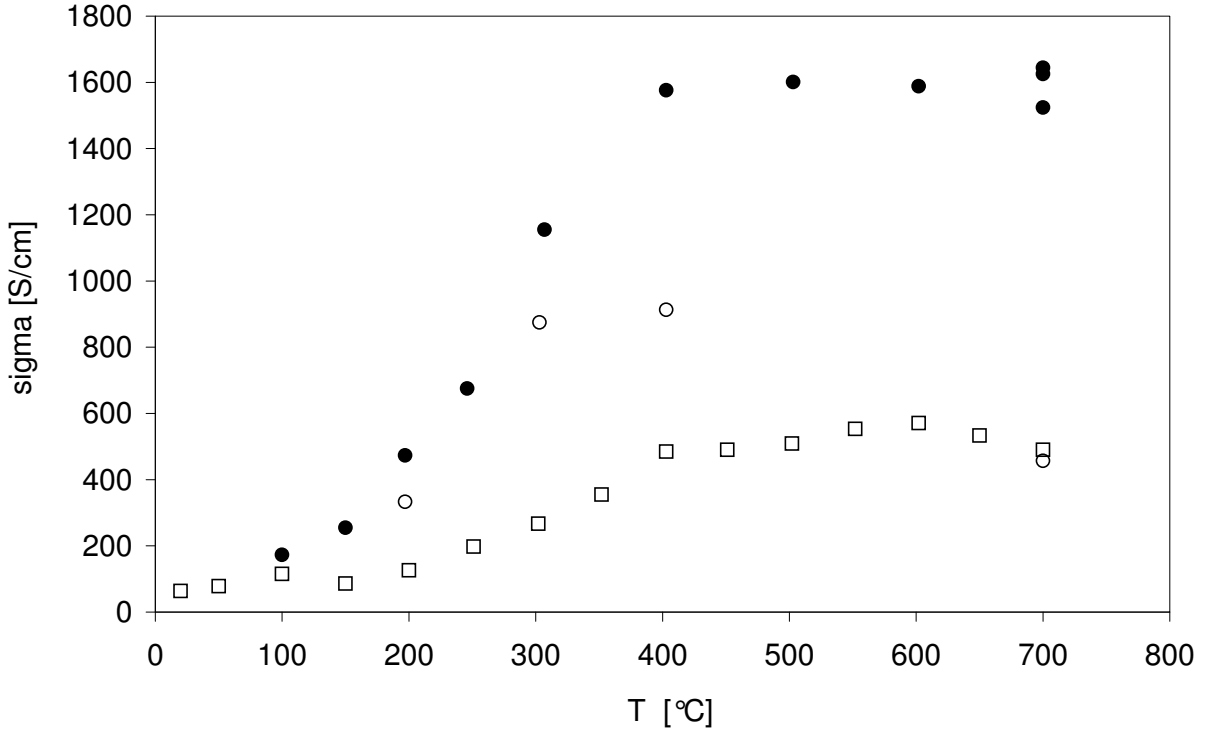


Figure 4.26: Electronic conductivity measured in van-der-Pauw geometry for a 470°C (white spots), 630°C (black spots), 340°C (white squares) deposited sample (320 nm) as a function of temperature.

The van-der-Pauw measurements confirm the assumption of an increased lateral sheet resistance for low film deposition temperatures. The difference between the highest and lowest conductivity was more than a factor of three in the temperature range between 400°C and 700°C. However, this also shows that for these LSC electrodes the electronic conductivity is not directly correlated with the oxygen incorporation process. Only if the electronic conductivity is too low this might affect the oxygen incorporation process (in case of the sample deposited at 230°C). An increased electronic conductivity does

not influence or accelerate the oxygen incorporation.

This increase of bulk resistance due to a decreased electronic conductivity is mainly observable in the macroscopic set up as the stiff Pt foil does not allow enough contact points to the thin film. In the microscopic set up the electrodes are much smaller and electrons are more easily spread over the whole electrode area. Hence, these effects are much less pronounced or negligible. This also suggests that the average distance of contact spots in macroscopic measurements is much larger than ca. $30\text{ }\mu\text{m}$, i. e. the distance electrons have to flow in micro-contact measurements.

Degradation of electrode resistance

The electrode resistances of many films increased while keeping the sample at 600°C or higher temperatures (degradation). Impedance spectra for a 200 nm film deposited at 630°C and measured once per hour at 600°C are exemplarily shown in fig. 4.27. The reason for the slight change of the high frequency intercept is probably a temperature fluctuation in the furnace. The degree of resistance degradation strongly depends on the deposition parameters.

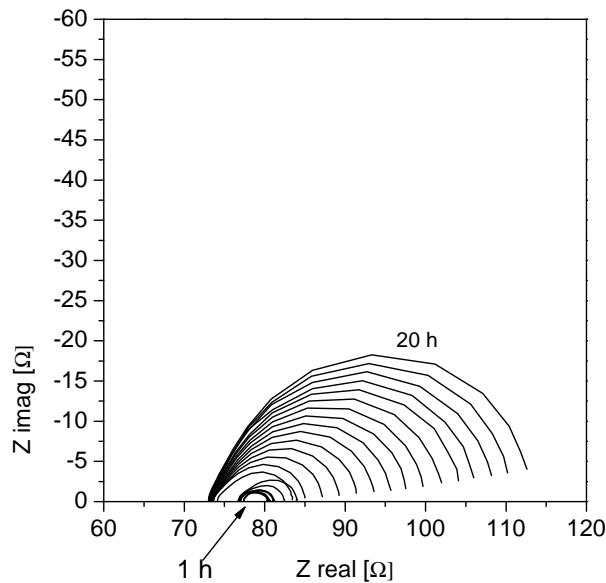


Figure 4.27: Impedance spectra for 200 nm LSC electrodes deposited at 630°C recorded once per hour while keeping the sample at 600°C (macro measurements).

The values of thicker films (fig. 4.29) only moderately increased whereas the resistances of the 40 nm thin films (fig. 4.28) on average became one to two orders of magnitude larger within 24 hours, meaning that the electrodes are less active with respect to oxygen

reduction after such an annealing. It becomes obvious that thicker films are generally more stable against degradation. The strongest degradation of 200 nm layers is found for films deposited at higher temperature while comparably little or almost no degradation is observed for 200 nm films deposited at temperatures between 340° and 510°C.

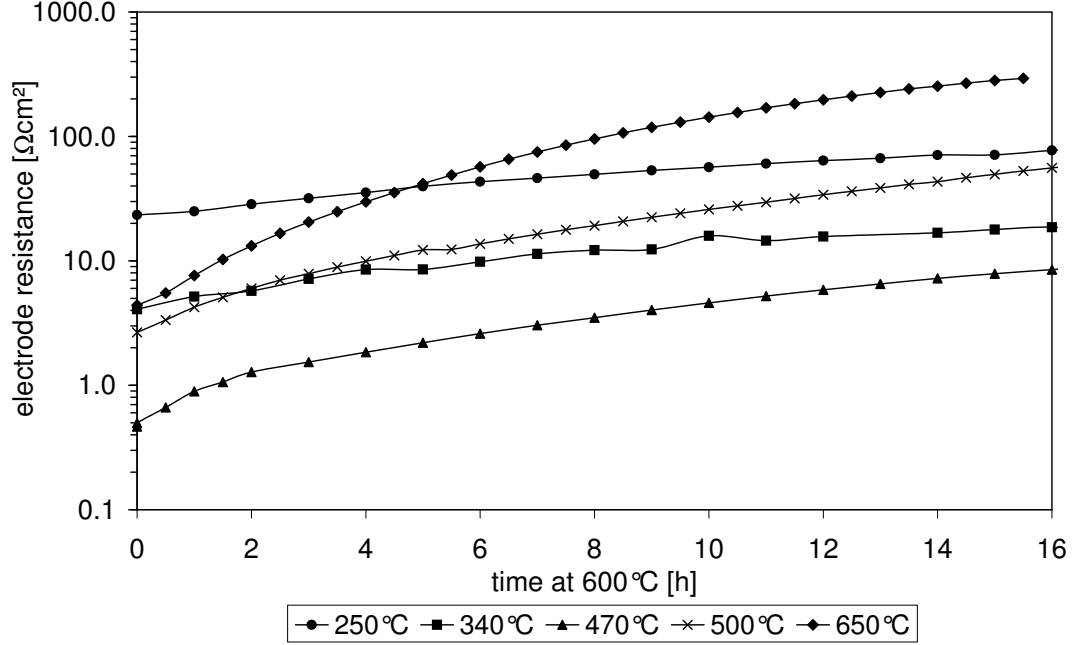


Figure 4.28: Degradation of the electrode resistance at 600°C for 40 nm LSC films deposited at temperatures between 250° and 650°C.

The phenomenon of long-term degradation of LSC electrodes is well known in literature [2, 21]. Some possible explanations suggested so far are changes in the morphology, contamination, growth of a second phase and thermal or chemical mismatches [2]. A second phase on the surface in form of crystallites, observed with SEM (fig. 4.3) and AFM (fig. 4.9), is found especially for very thin films (40 nm) though not for all films. Higher deposited thin films with a thickness of 200 nm have a degradation of resistance but no visible growth of crystallites on the surface within 72 hours at 600°C (fig. 4.2a and 4.2b). The nature of the crystallites grown on top of the surface of 40 nm thin films is not known. SrO, SrCO₃ or crystalline LSC are possible phases. The microstructural qualities visible in SEM investigations (e.g. particle size) stay constant for thicker films during degradation. So a correlation between degradation and the growth of crystallites on the surface cannot be proven but as the LSC films shown in fig. 4.2a and 4.2b are very stable it cannot be fully excluded. Hence a segregation and changed surface composition

is not ruled out as a reason for degradation. Further the most stable films (deposited between 340° and 510°C, 200 nm) show no increase of crystallinity, shown by XRD, during a heat treatment. In comparison higher deposited films show degradation and an increase of crystallinity. So it is obvious that good performance stability correlates with low electrode resistances and little crystallinity (XRD-amorphous films). Degradation of films is accompanied by an increase in crystallinity.

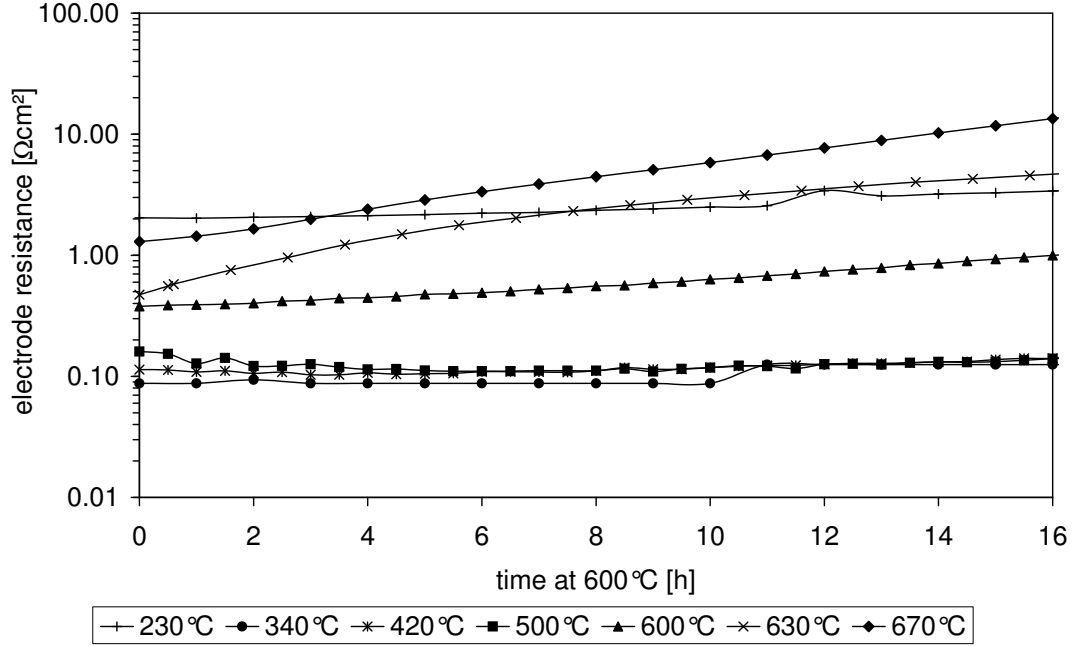


Figure 4.29: Degradation of the electrode resistance at 600°C for 200 nm LSC films deposited at temperatures between 230° and 670°C.

The degree of degradation further depends on the temperature. In fig. 4.30 three identical samples (deposited at 420°C, 160 nm) were measured once per hour at 500°, 600° and 700°C over three weeks. The electrode resistance is shown as a function of time at each temperature. At 700°C at the beginning the samples have the lowest resistance but already after less then one hour the resistance is larger than the resistance of the same sample at 600°C. After 15 hours the resistance is larger than the resistance of the same sample measured the whole time at 500°C. The sample measured at 600°C is degrading faster than the sample measured at 500°C and slower as the sample measured at 700°C. After 65 hours the sample measured at 600°C has a higher resistance than the sample measured at 500°C. The sample measured at 500°C is degrading slower and after 500 hours at 500°C the resistance increased from 0.7 Ωcm^2 to 4 Ωcm^2 .

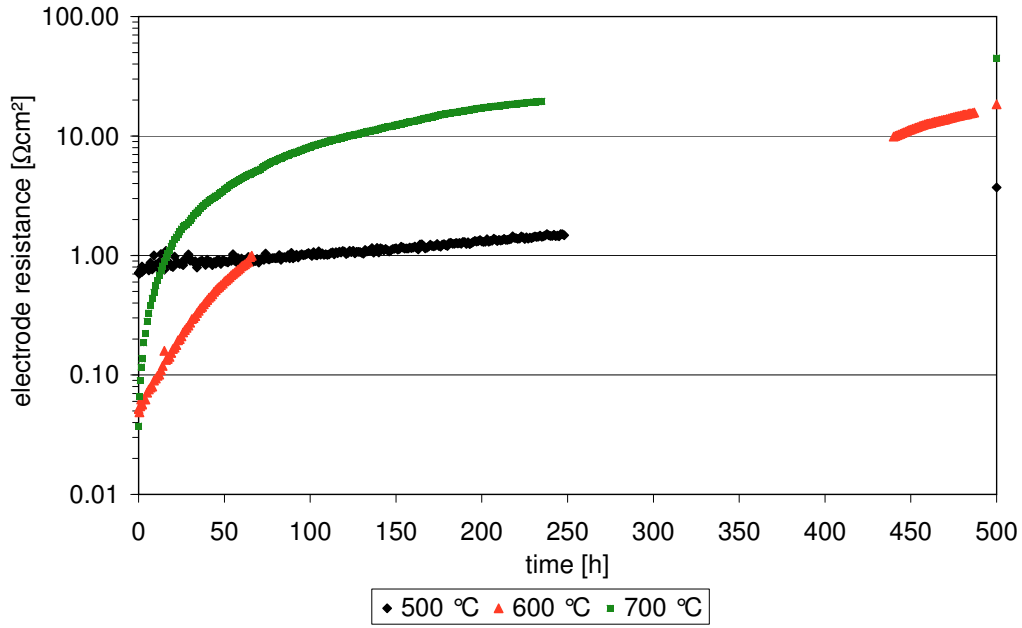


Figure 4.30: Degradation of the electrode resistance at 500°C, 600°C and 700°C of a 160 nm thick LSC film deposited at 420°C.

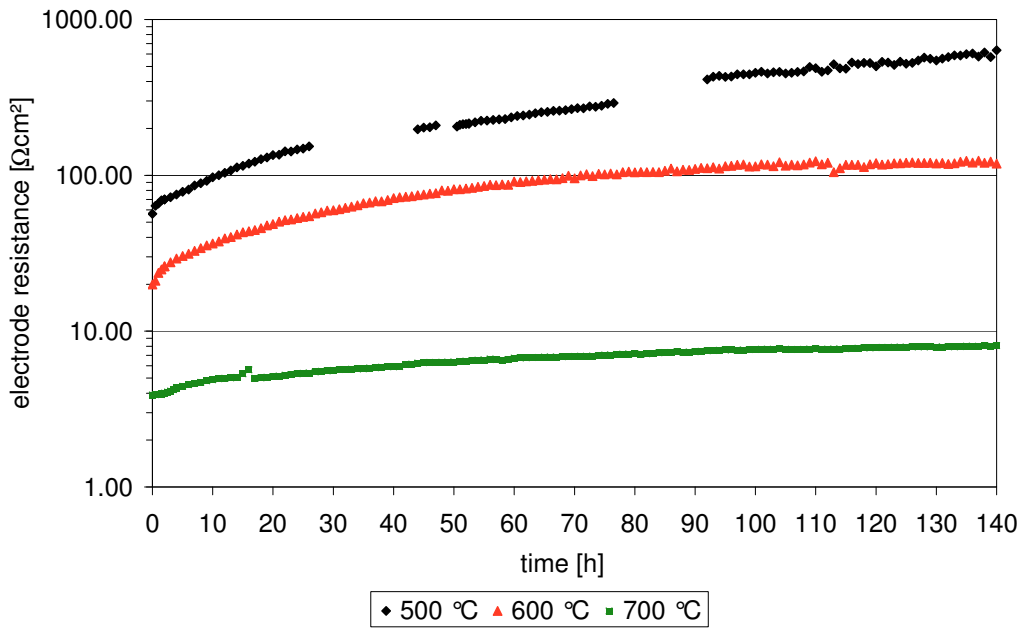


Figure 4.31: Degradation of the electrode resistance at 500°C, 600°C and 700°C of a 270 nm thick LSC film deposited at 650°C.

It is worth noting that degradation at 600°C was faster than that shown in fig. 4.29.

Reasons for this may be related to some uncontrolled (and unknown) parameters during film deposition or the somewhat smaller thickness (160 vs. 200 nm).

In fig. 4.31 the same degradation curves are shown for three samples deposited at 650°C (270 nm).

All starting values are higher (4-60 Ωcm^2) compared to the 420°C deposited samples (0.04-0.7 Ωcm^2). After 140 hours the resistance value of the sample measured at 700°C has increased by a factor of 2, the resistance of the sample measured at 600°C by a factor of 6 and the resistance of the sample measured at 500°C by a factor of 10. So the sample at 500°C shows the strongest degradation. However, after an initial strong increase of resistance of the samples at 500°C and 600°C all samples seem to increase parallel in resistance. The final values (after 140 hours) of the higher deposited sample are similar to those already reported in literature by Baumann et al. [21]. All samples deposited at 650°C have resistance values orders of magnitude higher than the samples deposited at 420°C, except the sample measured at 700°C. Differences in starting values are more pronounced than in fig. 4.29 which may be again related to unknown deposition parameters. The relative degree of degradation is smaller for the 650°C deposited sample (between 2 and 10 times within 140 hours) compared to the 420°C deposited sample (between 1.5 and 250 times within 140 hours). The lowest degree of degradation has the 420°C deposited sample at 500°C and the 650°C sample at 700°C. The resistance values as prepared and after 140 or 500 hours are summarized in table 4.1 and 4.2.

SEM images of the 420°C and 650°C deposited samples after 500 and 140 hours at 600°C are shown in fig. 4.5a and 4.5b (see chapter SEM). On the lower deposited sample crystallites are found on the surface while on the higher deposited sample after 140 hours morphological changes but no explicit growth of such crystallites are visible. So a direct correlation between degradation and the growth of crystallites on the surface is not possible at the moment.

However, the exact value of electrode resistance and the degree of degradation are certainly not only influenced by the deposition temperature [71] and time (thickness). In literature a lot of investigation on the dependence of properties on background oxygen pressure [18, 20, 72–74], laser pulse duration [74], laser fluence [73], laser spot size [20], and substrate orientation and composition [13, 46, 73, 75] have been performed and show that the PLD process is very complex and dependent on many parameters. So further investigations have to be carried out to get representative data for the exact value of electrode resistance and the exact degree of degradation as a function of the deposition parameters.

Table 4.1: Electrode resistance values in Ωcm^2 of a sample deposited at 420°C

Degradation at	After 0 hours	After 140 hours	After 500 hours
500°C	0.7	1	4
600°C	0.05	4	18
700°C	0.04	11	45

Table 4.2: Electrode resistance values in Ωcm^2 of a sample deposited at 650°C

Degradation at	After 0 hours	After 140 hours
500°C	60	640
600°C	20	120
700°C	4	8

Activation with voltage

A decrease of electrode resistance under voltage or after applying voltage is already known in literature for LSM [44, 76–79] and also for LSC [22, 23].

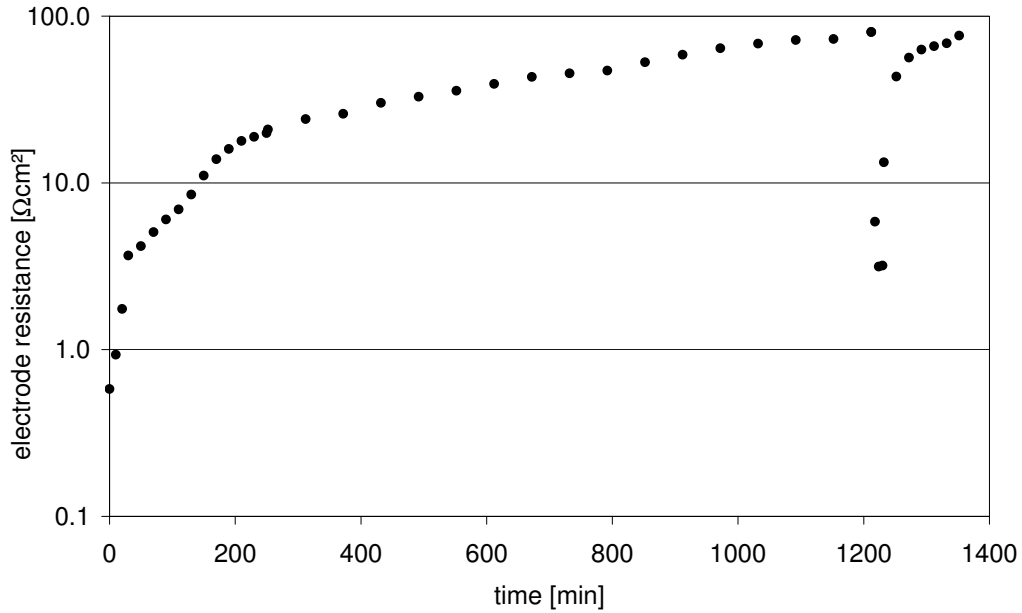


Figure 4.32: Electrode resistance as a function of time of a 40 nm thick LSC electrode deposited at 730°C and measured at 700°C. After 1200 minutes -2V were applied for 5 minutes.

In fig. 4.32 the electrode resistance at 700°C is shown as a function of time. The sample has a thickness of 40 nm and was deposited at 730°C. After 1200 minutes -2 V were applied for 5 minutes. Afterwards the impedance was measured every 5 minutes. A rapid decrease followed by gradual degradation (increase) of the resistance, much faster than before the activation, are found. During applying bias a darkening of the microelectrode is observed using microscope (fig. 4.33a). The darkening remains after removing bias. Fig. 4.33b displays the corresponding impedance spectra.

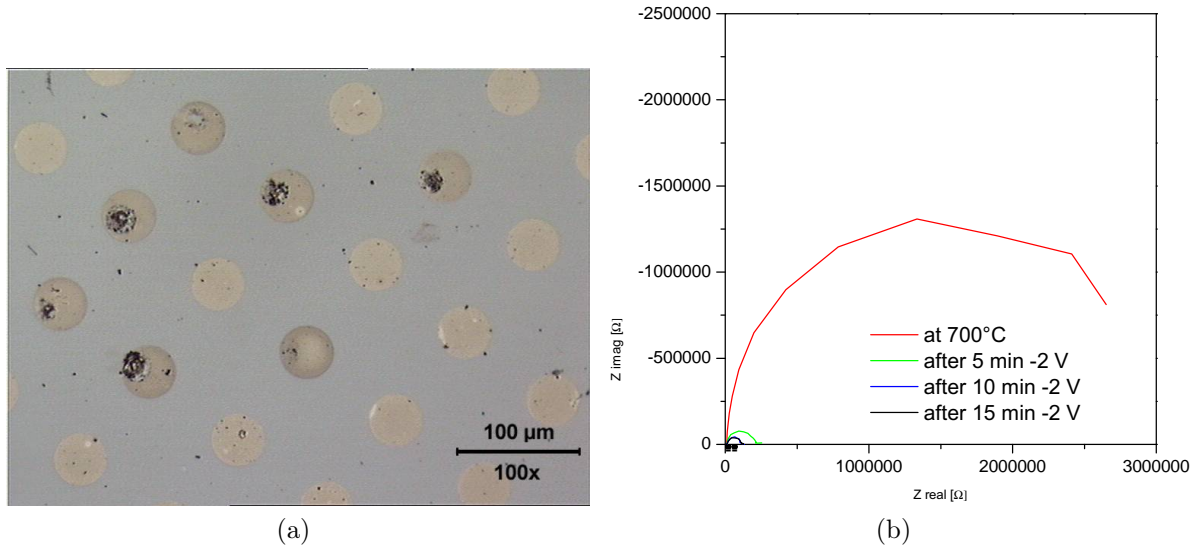


Figure 4.33: a) Darkening of microelectrodes under the microscope b) Impedance spectra of a 40 nm thick LSC film deposited at 730°C and measured at 700°C as prepared and after applying bias.

Table 4.3: Electrode resistances in Ωcm^2 measured at 600°C of two 40 nm thick LSC samples deposited at 540°C and 730°C, before and after 20 hours at 700°C

Sample deposited at	as prepared	After 15 min -3 V	After 15 min +3 V
540°C	6.5	4.4	-
540°C after 20 h at 700°C	111.6	10.1	31.1
730°C	55.3	3.4	3.6
730°C after 20 h at 700°C	114.6	8.7	14.3

The electrode resistance of 4 samples deposited at 540°C and 730°C before and after a heat treatment (20 hours, 700°C) was investigated. All samples have a thickness of 40 nm. The impedance was measured after some hours at 600°C and again after

applying +3V or -3V for 15 minutes. The results are shown in table 4.3. After the heat treatments of 20 hours at 700°C the resistance has increased compared to the as prepared sample. Applying bias reduced the electrode resistance in every case but applying cathodic voltage reduced the electrode resistance much stronger.

As many other parameters such as deposition temperature and thickness cause strong variations in the surface incorporation resistance and these resistances are changing very strongly over time due to degradation at measuring temperatures (500° – 700°C) only little efforts were done to investigate polarization behavior of these samples. In any case it is interesting that only an activation of samples with already higher electrode resistance is possible. The darkening was already observed in literature [80]. A color change is a result of a change in the electronic properties of a material; further possible explanations are a change of surface composition due to cation diffusion [76, 81] or a change in microstructure and morphology [76] which was only partially observed in this work. The detailed mechanisms are still unknown and need further investigations. The bubbles, observed in AFM after applying anodic bias might have formed when the chemical potential of oxygen in the electrode became too large and thus the transport through the LSC is no longer fast enough. The same phenomenon was already reported for LSM [24]. Other significant changes in surface morphology are not observed.

Activation with chemical etching

The influence of a chemical etching with diluted HCl (0.14 mol/L) was investigated. A sample deposited at 650°C (40 nm) measured in a macroscopic set up at 600°C is shown in fig. 4.34a. After 15 hours the sample was etched for 20 seconds with diluted HCl and impedance was measured again. A strong decrease nearly to the resistance of the as-prepared sample is observable. After etching an increased bulk resistance in the impedance spectra is also found (fig. 4.34b).

The same activation effect was observed for a 500°C deposited thin film (40 nm) measured using a microscopic set up (fig. 4.35a). The sample was etched for 10 seconds, impedance was measured and then the sample was etched for another 20 seconds in diluted HCl. The strong decrease to nearly the initial value of resistance is again observable but without an increase in bulk resistance. The activation of the resistance is nearly as strong as in the macroscopic experiment but the degradation afterwards proceeds much faster. The corresponding impedance spectra are shown in fig. 4.35b.

Removing the surface by chemical etching seems to recover the activity of the surface to a value very close to the initial one of an as prepared sample deposited at low temper-

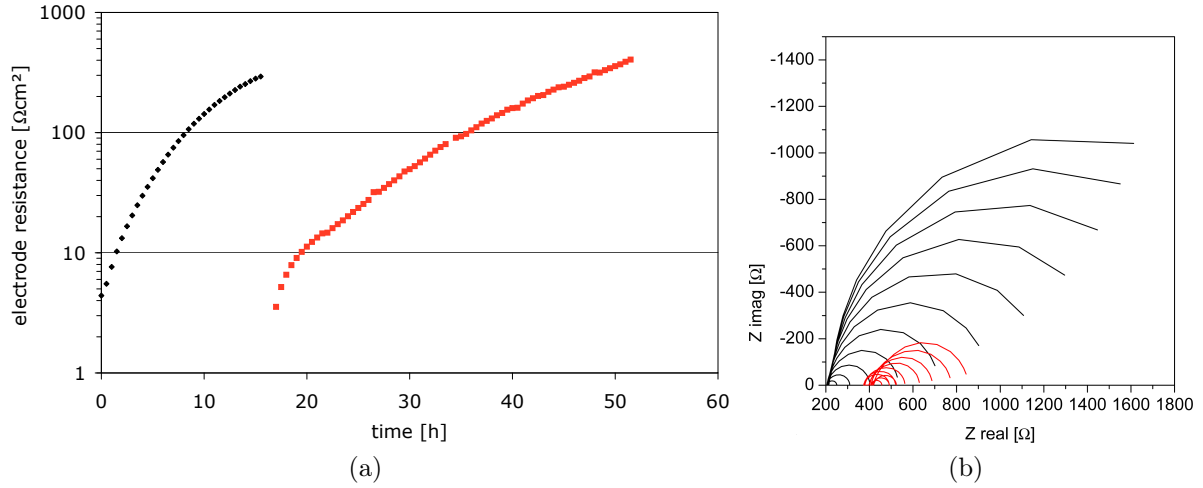


Figure 4.34: a) Electrode resistance as a function of time at 600°C of a 40 nm 650° C deposited sample (black) and etched for 20 seconds with diluted HCl (red) (a) and corresponding impedance spectra (b); measured macroscopically.

atures. This further proves that the electrode resistance is caused by a process taking place on the surface.

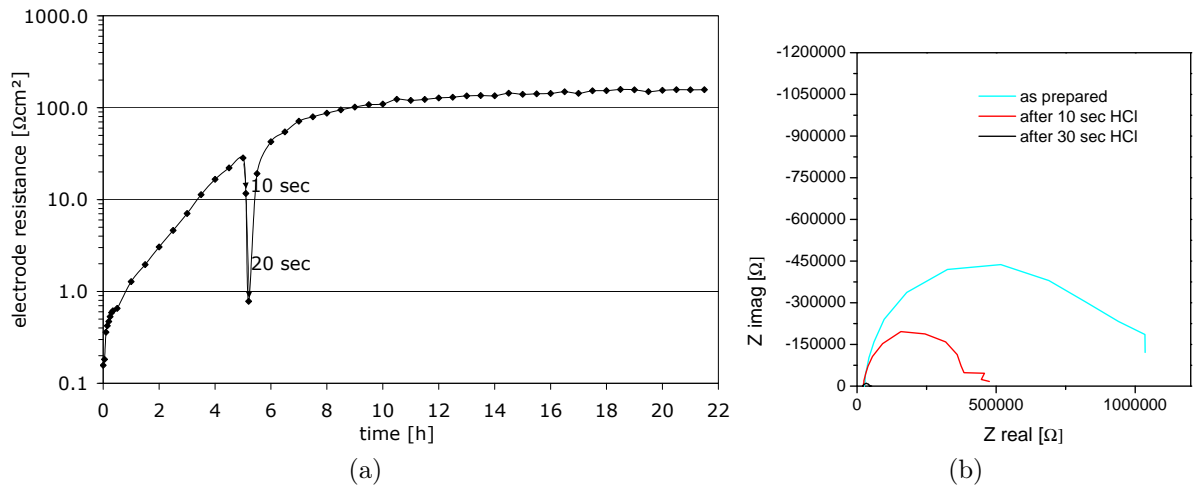


Figure 4.35: Electrode resistance of a LSC thin film (deposited at 520°C, 40 nm) as a function of time at 600°C and etched for 10 and then for 20 seconds with diluted HCl (a) and corresponding impedance spectra (b); measured microscopically.

The bulk resistance of 200 Ω (fig. 4.34) is already increased compared to an expected value of 70 Ω for the pure YSZ conductivity. After chemical etching the bulk resistance further increased from 200 to 400 Ω in the macroscopic set up. This can be related to an additional increase in lateral sheet resistance owing to the decreased film thickness.

This sheet resistance was usually of no importance for micro-structured electrodes as the distance between the place of oxygen incorporation and current supply is much smaller. The very fast degradation after etching, in the microscopic set up, was also observed after the activation by voltage. As activation experiments by voltage are not straightforward in the macroscopic set up, no comparison with voltage activation in the microscopic set up is possible. Anyway there is a strong indication that micro-structured samples seem to degrade faster than samples measured in the macroscopic set up. This is not explainable by structure and crystallinity changes as the thin film and the temperature are the same. Possibly different impurities in the microscopic set up cause this stronger increase.

4.1.3 LEIS

Thin films deposited at 450 and 650°C (100 nm thickness) before and after a heat treatment of 3 days at 600°C were investigated with LEIS. The sample parameters and names are shown in table 4.4. To measure impurities 3 keV Helium primary ions were used, as lighter elements are not visible when using Neon primary ions. 5 keV Neon primary ions were used to measure the La/Sr ratio of the first monolayer. The intensity of primary ions was that small that only 2 % of the first monolayer were removed. The LEIS spectra measured with Neon and Helium are shown in fig. 4.36 and fig. 4.37.

Table 4.4: Samples and sample numbers in the LEIS spectra (100 nm thickness)

Sample deposited at	$^4\text{He}^+$	$^{20}\text{Ne}^+$
450°C	<i>LSC_18_0</i>	<i>LSC_14_0</i>
450°C after 3 days at 600°C	<i>LSC_19_0</i>	<i>LSC_15_0</i>
650°C	<i>LSC_20_0</i>	<i>LSC_16_0</i>
650°C after 3 days at 600°C	<i>LSC_21_0</i>	<i>LSC_17_0</i>

The sensitivity of this method is different for every element. The sensitivity for lanthanum for example is higher compared to the sensitivity for strontium. For a better quantification reference samples have to be prepared and investigated. However, a first estimate is possible by comparing the strontium to lanthanum signal ratio of different samples. In table 4.5 the ratio of the peak integrals are shown. The sample with the lowest Sr/La ratio is the thin film deposited at 450°C. The sample deposited at 650°C has a 3 times higher Sr/La ratio. During the heat treatment the Sr/La ratio increased for both samples.

Table 4.5: Peak integrals of the Ne spectrum in counts/nC.

Sample deposited at	Sr- integral	peak- integral	La- integral	peak- integral	Ratio Sr/La
450°C	1202		712		1.7
450°C after 3 days at 600°C	2021		378		5.3
650°C	1530		580		2.6
650°C after 3 days at 600°C	1792		260		6.9

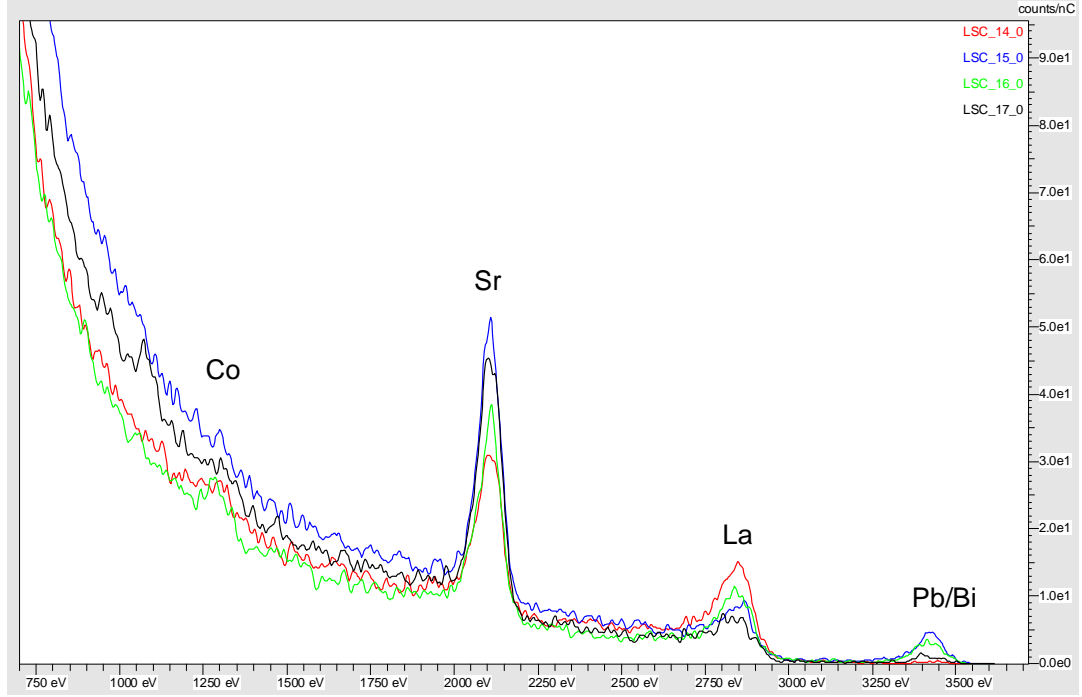


Figure 4.36: LEIS spectra recorded with 5 kV Ne primary ions.

Comparing this behavior to that of the electrode resistances it is obvious that thin films which have the lowest resistances (450°C deposited sample, as prepared, and both samples after chemical etching) have also the lowest Sr/La ratio. During degradation the electrode resistance is increasing and also the Sr/La ratio is increasing. So a correlation between the Sr/La ratio and the electrode resistance is found in LEIS measurements. The Sr segregation on the surface after long term degradation was already reported in literature for LSC [82], LSCF [83] and for LSM [81]. However, whether the Sr segregation to the surface is sufficient to explain all effects observed in the electrochemical measurements is still an open question.

Table 4.6: Peak integrals of the He spectrum in counts/nC

Sample deposited at	F	Na/Mg	K/Ca	Co	Pb/Bi
450°C	27	0	0	0	12
450°C after 3 days at 600°C	24	22	11	41	232
650°C	29	0	0	0	174
650°C after 3 days at 600°C	33	79	84	84	54

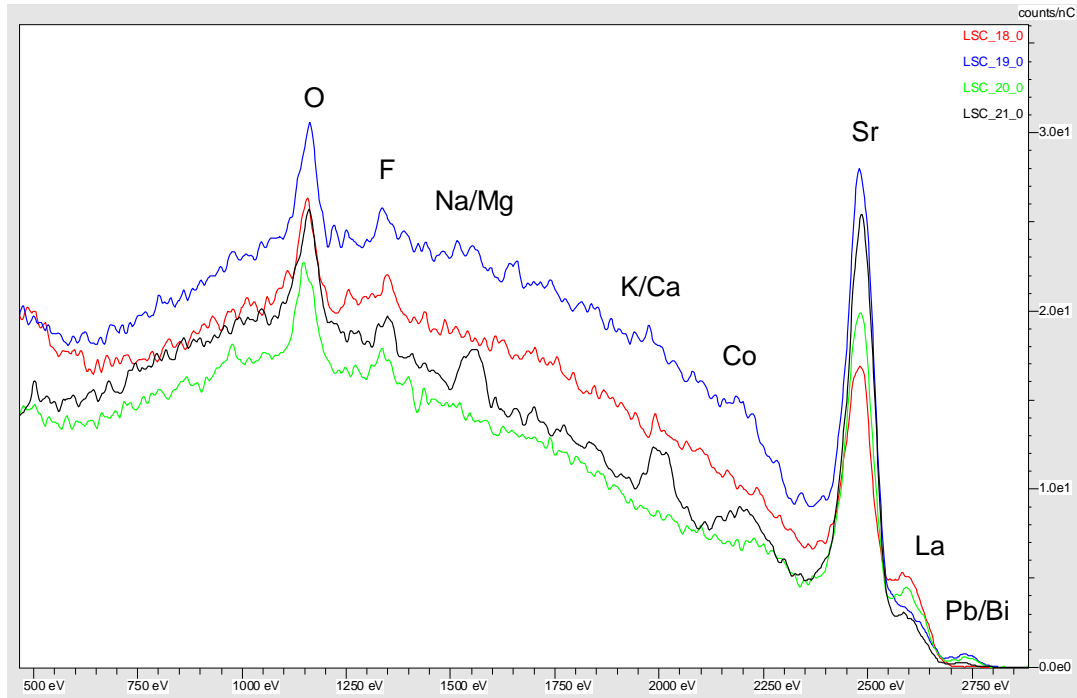


Figure 4.37: LEIS spectra recorded with 3 kV He primary ions.

In addition to strontium and lanthanum, significant amounts of other elements such as F, Na/Mg, K/Ca and Pb/Bi have been found. At this point of evaluation no differentiation between Na and Mg, K and Ca can be made. F is observed on all samples without significant differences in concentration. Na/Mg and K/Ca are only measured on the heat-treated samples. Most probably Pb is found on all samples though Bi cannot completely be excluded. Impurities such as Na/Mg and K/Ca are almost unavoidable in a normal environment and LEIS is especially sensitive to these elements. The samples are most probably polluted during the heat treatment in the furnace by these elements. The contamination with Pb (or Bi) is quite unexpected. In the laboratory lead zirconate

titanate (PZT) is used and may have caused these contaminations. All results are summarized in table 4.6.

A very interesting fact is that traces of Co are found only in the heat-treated samples. The as prepared samples have no Co in the first monolayer on the surface. As Co is the only element in LSC having the opportunity to change it's valence state it is supposed to play an important role in the oxygen reduction. The absence of this element on the surface is quite surprising. Anyway LEIS gives no absolute information about the second and third layer of the surface.

4.2 Different A and B-site compositions

In this chapter the different strontium doping concentrations and the influence of iron replacing Co on the B-site of the perovskite lattice are investigated. With the same preparation route as the $\text{La}_{0.6}\text{Sr}_{0.4}\text{CoO}_{3-\delta}$ was synthesized [59] targets with the composition $\text{La}_x\text{Sr}_{1-x}\text{CoO}_{3-\delta}$ with $x=0.8, 0.6, 0.4$ and $\text{La}_{0.6}\text{Sr}_{0.4}\text{Co}_y\text{Fe}_{1-y}\text{O}_{3-\delta}$ with $y=1, 0.7, 0.5, 0.3, 0$ were prepared. LSC powder with 80% strontium was synthesized but it was not possible to compact it into a target. Then PLD thin films were prepared with the same set up as the standard LSC composition.

4.2.1 Thin film characterization

In fig. 4.38 the diffraction patterns of a $\text{La}_{0.8}\text{Sr}_{0.2}\text{CoO}_{3-\delta}$ LSC82 (blue) and a $\text{La}_{0.4}\text{Sr}_{0.6}\text{CoO}_{3-\delta}$ LSC46 (green) thin film, both deposited at 650°C , are shown. The $\text{La}_{0.8}\text{Sr}_{0.2}\text{CoO}_{3-\delta}$ thin film has the same main orientation in $[1\ 1\ 0]$ as the LSC thin film with 60% lanthanum. The $(1\ 1\ 0)$ peak is at 33.3° and the $(2\ 2\ 0)$ peak at 69.7° . The texture of the $\text{La}_{0.4}\text{Sr}_{0.6}\text{CoO}_{3-\delta}$ thin film is mainly $[1\ 0\ 0]$. The corresponding peaks are the $(1\ 0\ 0)$ peak at 23.4° and the $(2\ 0\ 0)$ peak at 47.8° . All other peaks correspond to the single crystalline YSZ substrate.

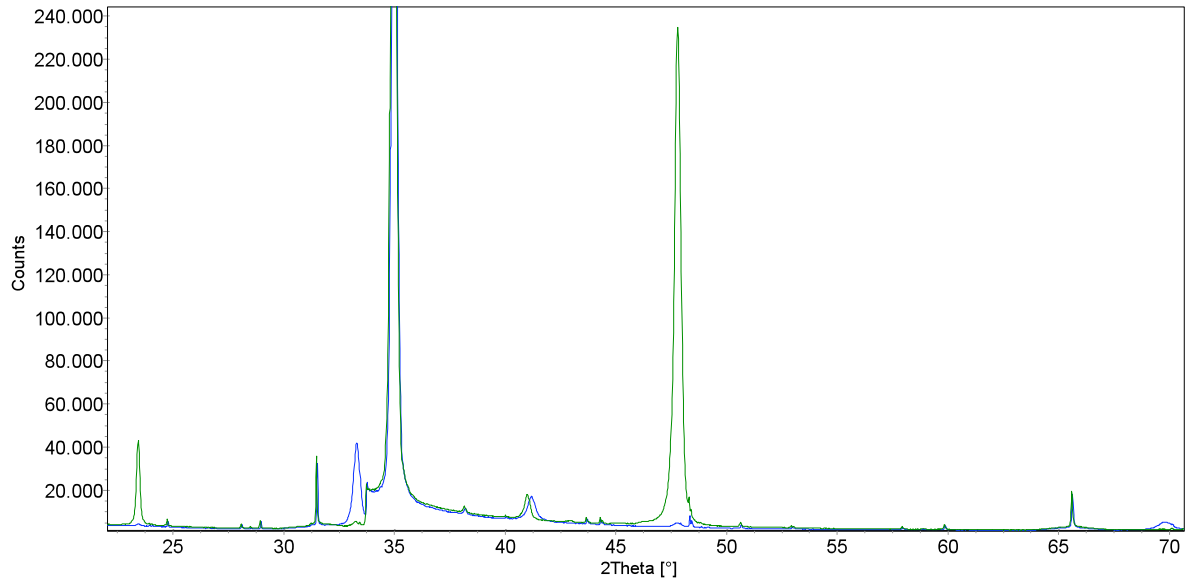


Figure 4.38: XRD pattern of LSC82 (blue) and LSC46 (green) deposited at 650°C on single crystalline YSZ.

4.2.2 Electrochemical characterization

Single crystalline YSZ substrates were on both sides coated by LSC and the impedance was measured once per hour at 600°C (fig. 4.39). LSC thin films with 80% lanthanum (LSC82) exhibit the highest resistances. Thin films deposited at higher deposition temperatures show higher electrode resistances. For thin films with 40% lanthanum and 60% strontium (LSC46) the lowest resistance values are measured. Again the higher deposited samples have higher resistance values but the distribution is much narrower and the values are smaller compared to thin films with 60% and 80% lanthanum. The capacitances of the main arc for LSC82 is around 3 mF/cm² and for LSC46 between 20 and 30 mF/cm². They are independent from deposition temperature and annealing time at 600°C. Since thicknesses are similar for all films, this means the chemical capacitance (per volume) is lowest for 20 % strontium.

However, nearly all LSC thin films shown in this work have a very good performance towards oxygen reduction compared to literature [9]. Degradation is observed for all compositions and seems to be unaffected by changing the La/Sr-ratio in the whole film. It is further notable, that the LSC46 thin films have a different crystallographic orientation (1 0 0) than LSC64 and LSC82. So even though the texture is changing, the performance of the electrodes is not changing. However, it has to be considered that only

a small percentage of the films is crystalline and the measured texture only refers to this small crystalline amount of the thin films. It is not possible to evaluate from these XRD measurements whether the major part of the thin films is crystallographically similar for all compositions.

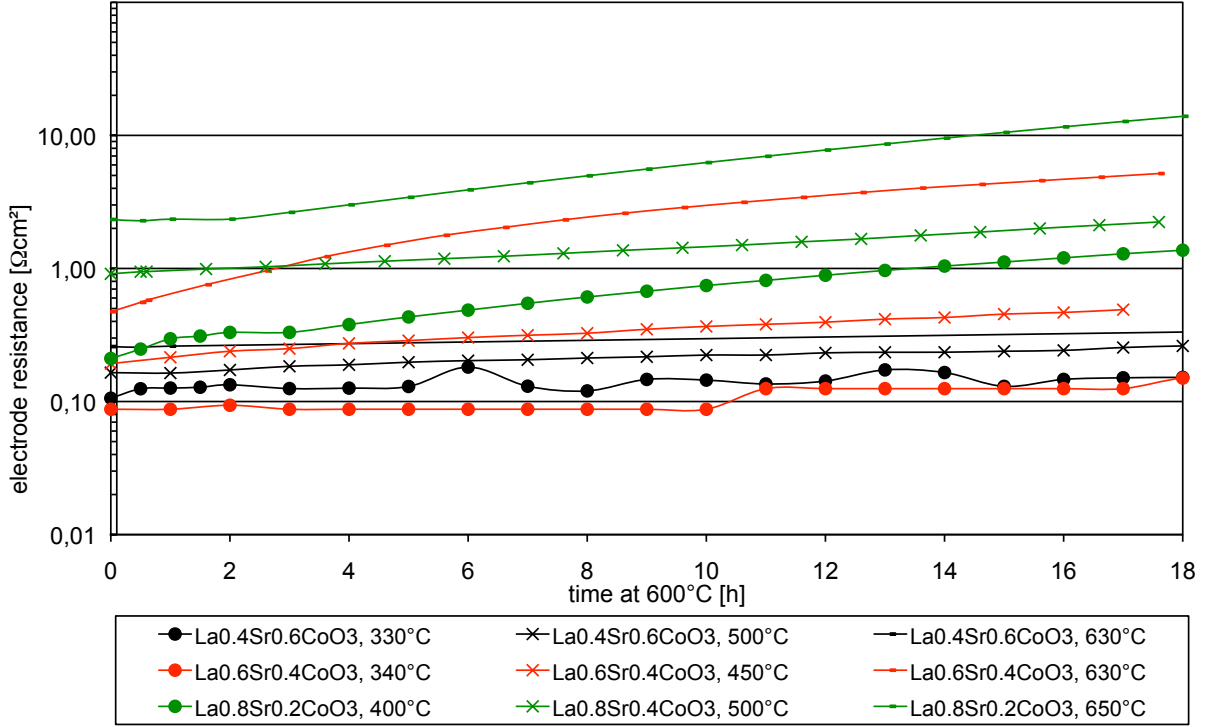


Figure 4.39: Electrode resistance as a function of time at 600°C for LSC82, LSC64 and LSC46 thin films (around 200 nm) deposited at different temperatures; measured macroscopically.

The bulk resistances obtained from macroscopic measurements on LSC46 and LSC82 range from 120 to 130 Ω for the lowest deposited samples (330-400°C), between 80 and 100 Ω for the intermediate deposition temperatures (500°C) and between 60 and 70 Ω for the highest deposition temperatures (630-650°C). These values are in accordance with the results obtained for LSC64 (see chapter Electronic conductivity and bulk resistance).

The LSCF and LSF thin films deposited on single crystalline YSZ have a very bad performance and are most of the time measurable just above 700°C due to the high resistance values. After several hours at 600°C and 700°C LSCF6437 the electrodes become measurable in the applied frequency range but exhibit resistance values much higher than identically prepared LSC electrodes (fig. 4.40a). The resistance values of lower deposited LSCF6437 of 130 Ωcm^2 at 700°C is significantly higher than 10 Ωcm^2 at

700°C reported for high temperature deposited LSCF6428 in literature [21]. Pure LSF exhibits even much higher electrode resistance when deposited at 550°C (fig. 4.40b) and is much above 20 Ωcm^2 as reported in literature [21].

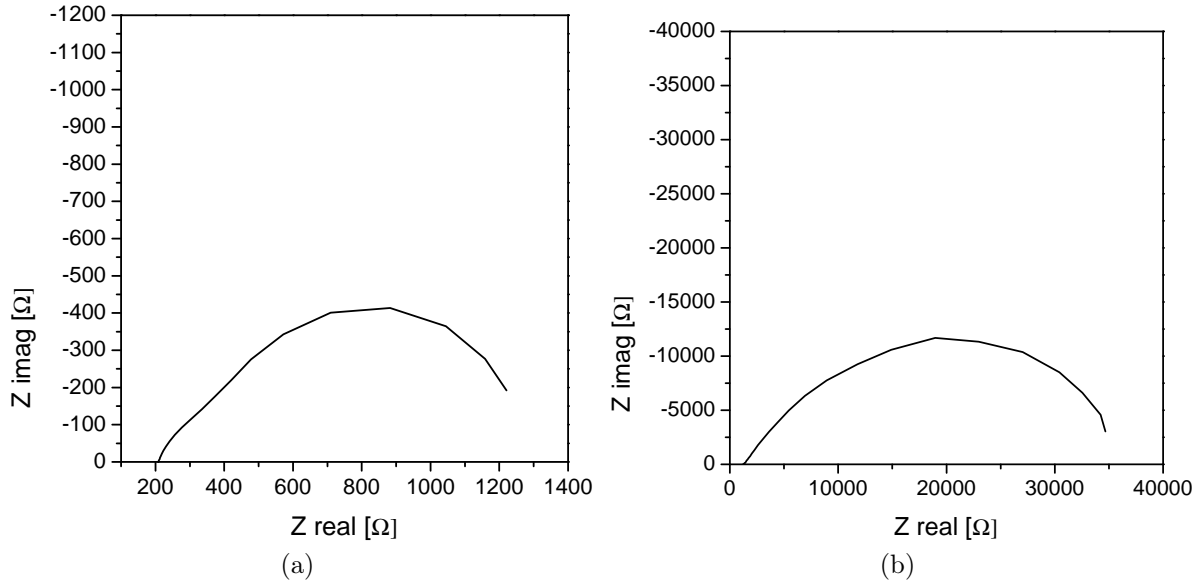


Figure 4.40: Impedance spectra macroscopically recorded at 700°C on 200nm thick LSCF6437 film deposited at 550°C after 2 days at 600°C (a) and on a LSF thin film deposited at 550°C after 2 days at 700°C (b).

The bulk resistances are by far larger than the expected values of pure YSZ (above several hundred Ω instead of 70 Ω). So the electronic conductivity seems to be much lower in not fully crystalline LSF and LSCF thin films than in not fully crystalline LSC thin films. This is in accordance with the different electronic conductivity of LSF and LSC found for crystalline material [27, 36]. The low electronic conductivity have a strong influence on the measured electrode resistance but the particular reason for the bad performance of LSCF and LSF is not known yet. However, cobalt seems to play an important role for the very fast oxygen reduction and is strongly indicating the importance of the electronic structure for the process of oxygen reduction. The best performance of all investigated compositions was found for LSC46.

4.3 LSC thin films on polycrystalline YSZ and GDC

4.3.1 Thin film characterization

In fig. 4.41 the diffraction pattern of a LSC thin film deposited at 410°C (700 nm thickness) on polycrystalline YSZ is shown.

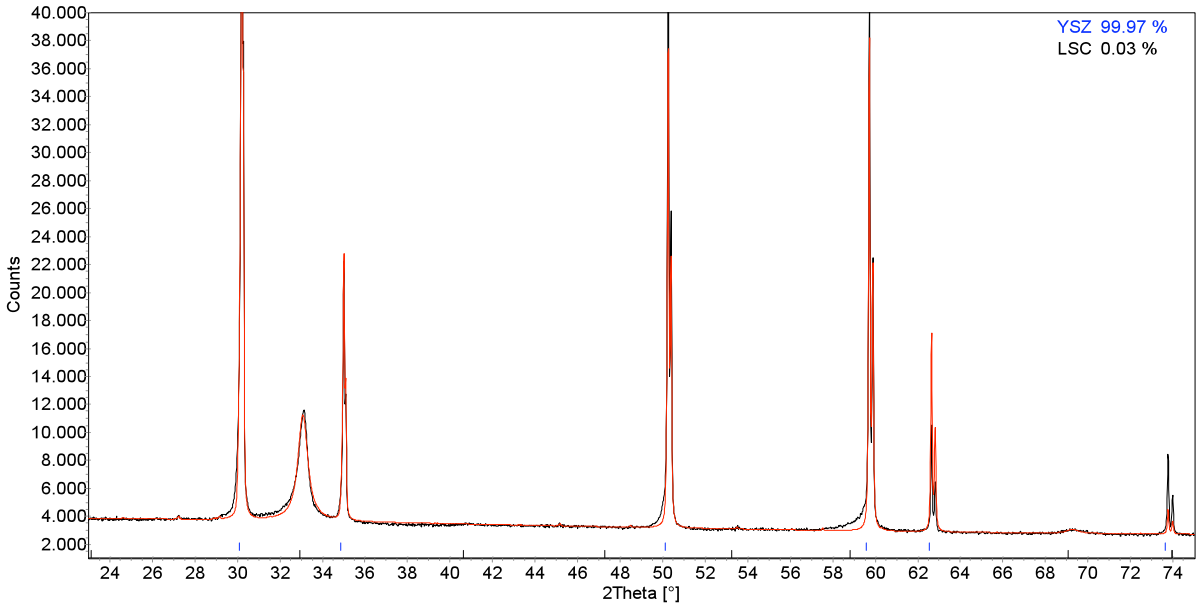


Figure 4.41: XRD pattern of a 700 nm thick LSC film deposited at 410°C on polycrystalline YSZ.

The LSC film is textured mainly in $[1\ 1\ 0]$ direction. Due to the low deposition temperature no further peaks are observed. The corresponding peaks are at 33.3° and 69.7°. The other peaks can be related to polycrystalline YSZ. The diffraction pattern of a thin film deposited at 410°C (1000 nm) on polycrystalline GDC (10mol% Gd_2O_3) is shown in fig. 4.42. As the peaks of the GDC have the same positions in the diffraction pattern as most LSC peaks, very little crystallographic information can be achieved. Only peaks in $[1\ 0\ 0]$, $[1\ 1\ 1]$ or $[2\ 1\ 1]$ orientation can be excluded, which is in accordance to former results. All peaks in the diffraction pattern are in accordance with the pattern for pure GDC. More crystallographic information was found in TEM measurements with selected area diffraction.

Although Rietveld analysis was done for all XRD pattern no reliable information about the crystallite size of the samples was found.

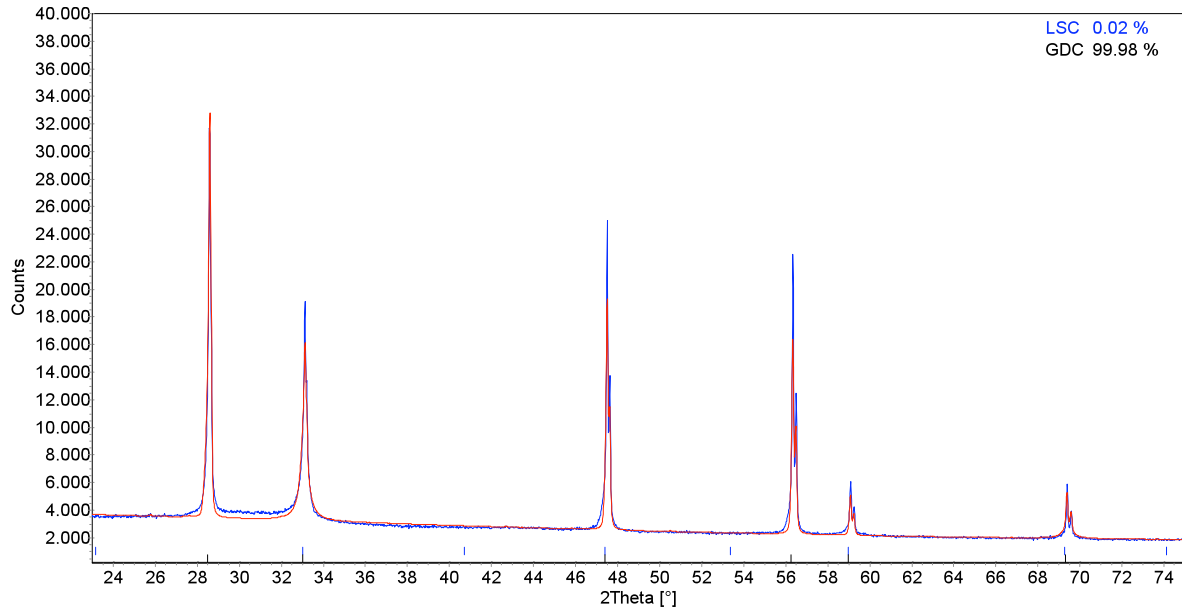


Figure 4.42: XRD pattern of a 1000 nm thick LSC film deposited at 410°C on polycrystalline GDC.

A TEM cross section image of LSC on polycrystalline YSZ deposited at 410°C is shown in fig. 4.43a. The top layer on the 700 nm thick LSC film is a protection layer needed during the preparation. A columnar growth of LSC and several pores along the grain boundaries are observable. The red circles in the image sign the aperture spots for the SAD analysis.

The SAD pattern of area 1 (near the surface) and area 2 (near the interface) are quite similar (fig. 4.43b). Both show light spots corresponding to highly textured crystalline areas in the film and rings corresponding to randomly oriented nanocrystalline and amorphous regions, as they are not sharp. So there seems to be no significant crystallographic difference between the surface and the interface region of the film.

The TEM cross section image of a 1000 nm thick LSC film on GDC deposited at 410°C (fig. 4.44a) shows also a columnar growth of the thin film on the substrate. The corresponding SAD pattern (fig. 4.44b) exhibit significant differences. The SAD pattern 2 (near the surface) shows broad rings indicating that most of the LSC is amorphous. The SAD pattern 1 recorded near to the interface is much more similar to the SAD pattern of LSC on polycrystalline YSZ. Broad rings indicate again an amorphous amount of LSC but the sharp spots correspond to crystalline LSC.

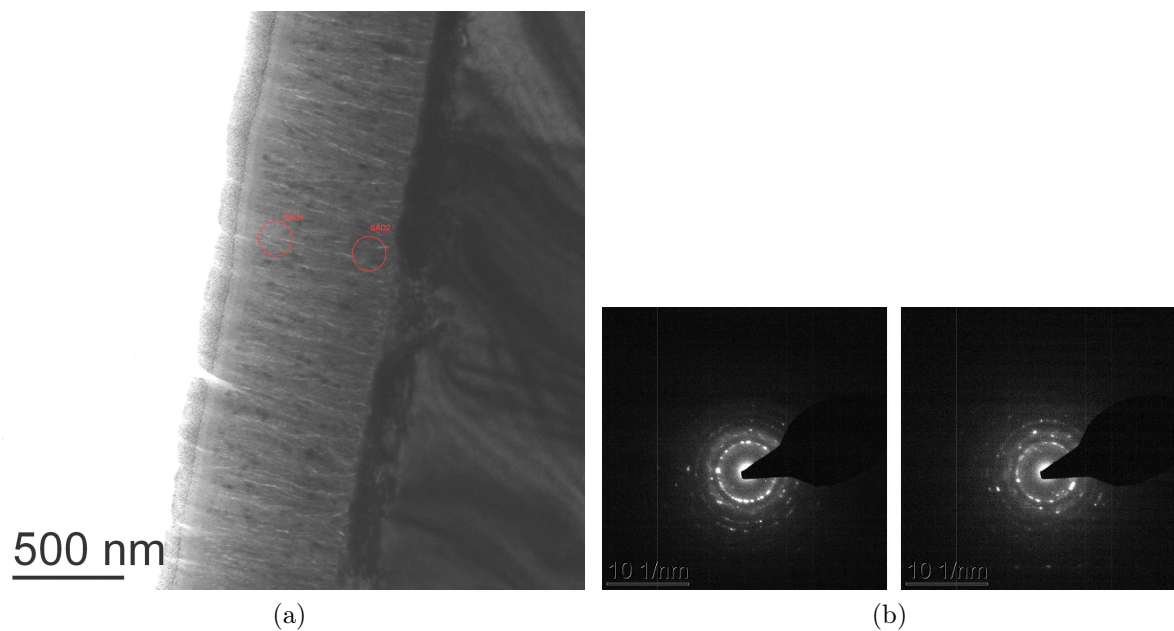


Figure 4.43: a) TEM image of a LSC thin film deposited on polycrystalline YSZ.
b) SAD patterns of a LSC thin film deposited on polycrystalline YSZ (1 left, 2 right).

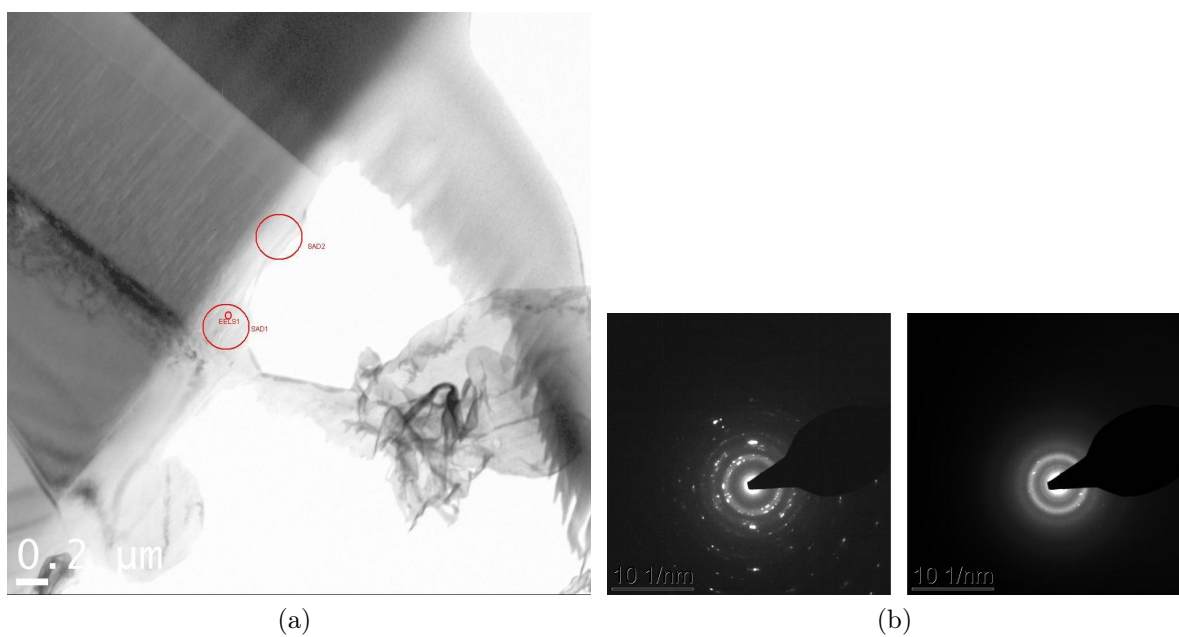


Figure 4.44: a) TEM image of a LSC thin film deposited on polycrystalline GDC.
b) SAD patterns of a LSC thin film deposited on polycrystalline GDC (1 left, 2 right).

4.3.2 Electrochemical characterization

LSC on polycrystalline YSZ exhibits only sometimes two well separated semicircles (fig. 4.46a). The low frequency arc has a capacitance of 170 mF/cm² and the intermediate frequency arc one of about 4 mF/cm². Impedance spectra of LSC electrodes with very small electrode resistances have a very low quality and the semicircles are not separated (fig. 4.45a). Further in some cases the quality is sufficient but the relaxation frequencies are too similar (fig. 4.45b).

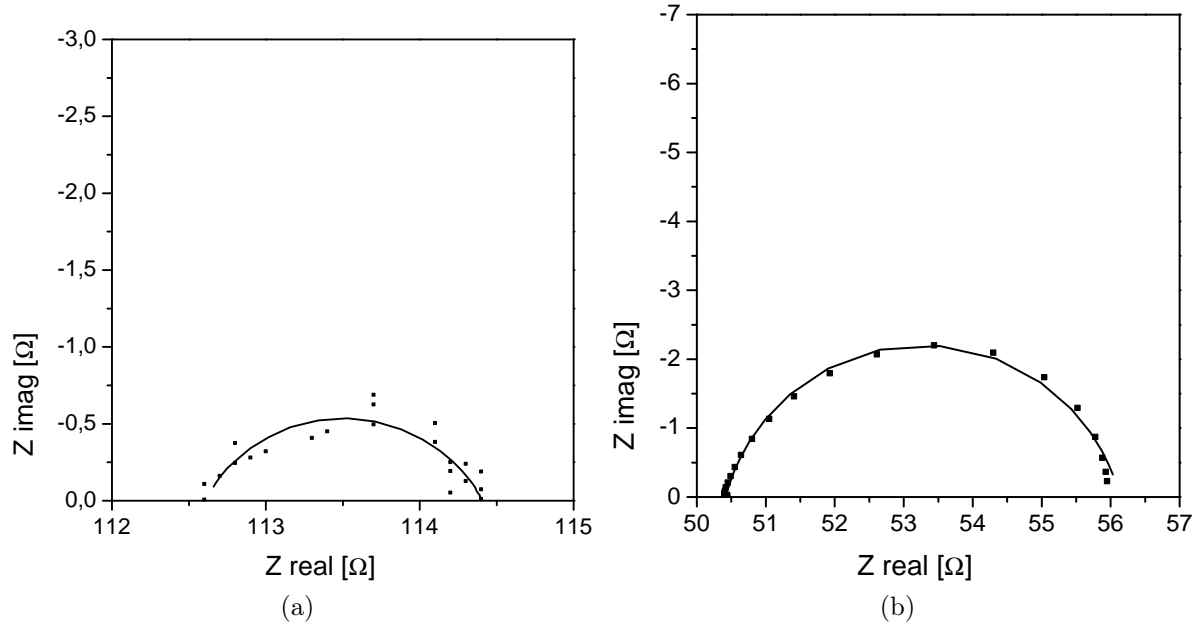


Figure 4.45: Impedance spectra of 150 nm thick LSC films on polycrystalline YSZ deposited at 350°C (a) and 650°C (b) measured at 600°C.

The impedance spectra of LSC on polycrystalline GDC (fig. 4.46b) exhibits one large semicircle at intermediate frequencies and one smaller semicircle at lower frequencies. This second arc is often not visible or separable (fig. 4.47 after 1 hour at 600°C (light green curve)) and appears not until keeping the sample at 600°C for several hours (fig. 4.47 after 20 hour at 600°C (red curve)). The capacitance of the low frequency semicircle is about 10 mF/cm². The capacitance of the main arc for most samples is between 25 and 100 nF/cm². This very small capacitance indicates existence of a very thick layer around 200 nm assuming a relative permittivity of 10-20. From the resistance of 70 Ωcm² at 600°C a conductivity of $3 \cdot 10^{-7}$ S/cm can be calculated for this layer. This value is independent of the film thickness and the deposition temperature. Microscopically

and macroscopically measured samples show the same results. Whether an „interface layer“ of 200 nm which is approximately the whole film thickness is realistic or not needs further considerations and investigations. Also the physical origin of this resistance is unknown.

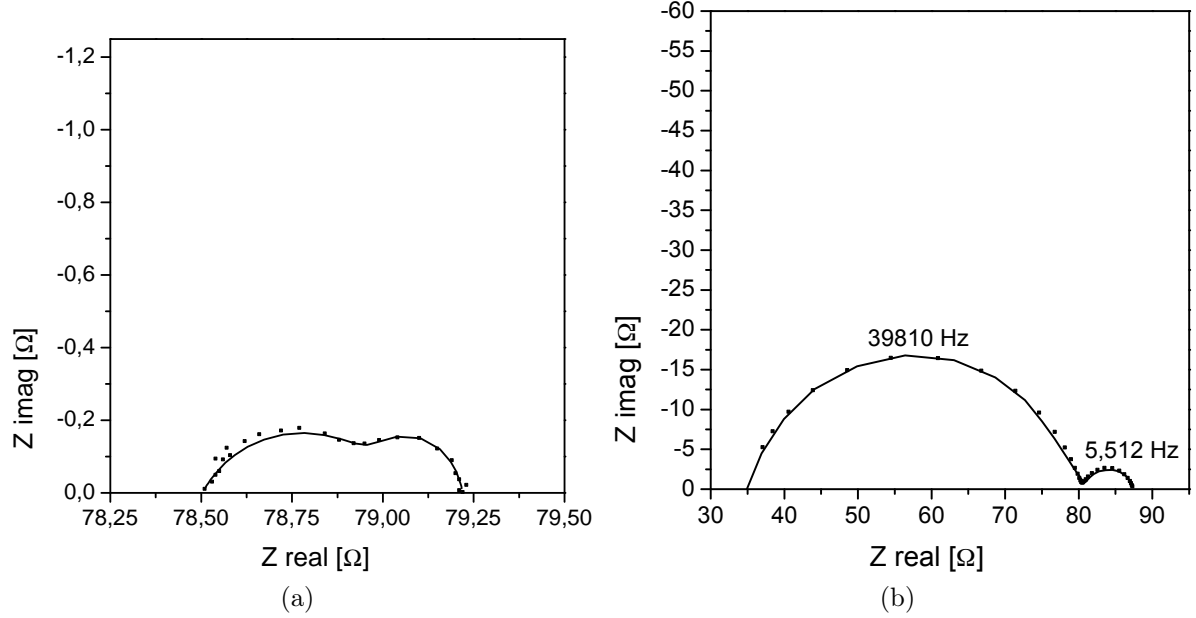


Figure 4.46: Impedance spectra of 150 nm thick LSC films deposited at 500°C on polycrystalline YSZ (a) and of 150 nm thick LSC films deposited at 350°C on polycrystalline GDC (b) both measured at 600°C.

The electrode resistance or the sum of the two resistances was scaled to the total surface area of the two equivalent electrodes. The dependence of the normalized electrode resistance on deposition temperature of LSC deposited on different substrates is shown in fig. 4.48. The solid line is a guide to the eye. Thin films deposited on (single- and polycrystalline) YSZ have electrode resistances of about 0.1 to 0.3 Ωcm^2 for deposition temperatures in the range of 340° - 510°C. Most films deposited at much lower or much higher temperatures show substantially higher electrode resistances. There is no significant difference between films deposited on single crystalline and polycrystalline YSZ substrates. In contrast thin films deposited on polycrystalline GDC exhibit much larger electrode resistances. A significant dependence of electrode resistance on the deposition temperature cannot be found. However, the scattering of the data indicate further other unknown parameters, which influence the results.

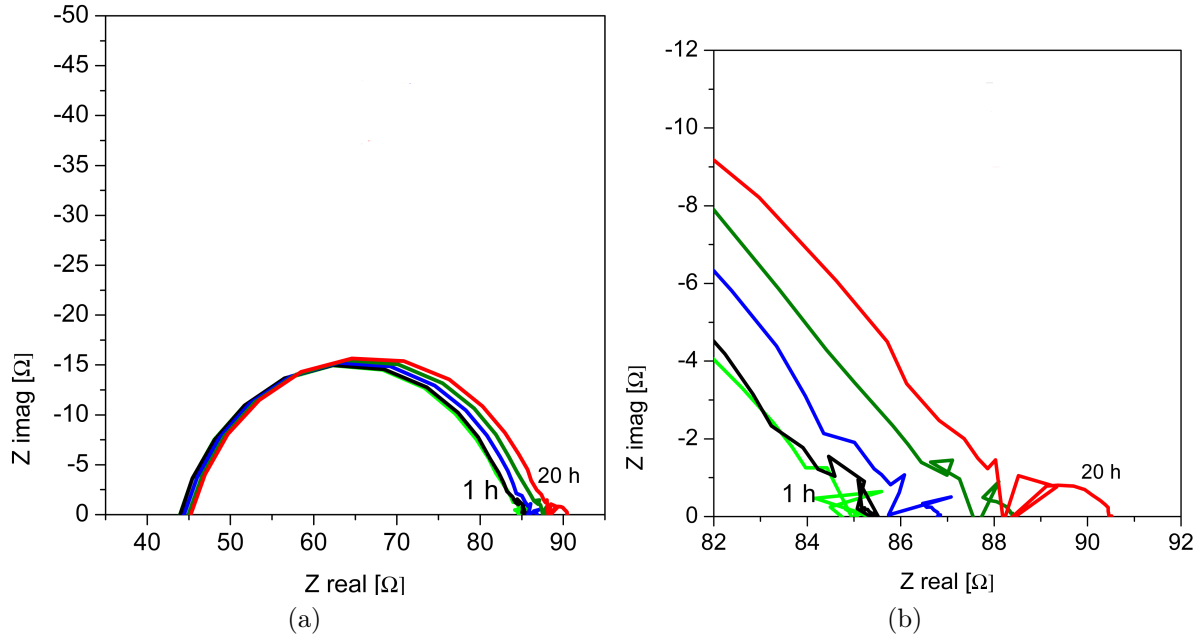


Figure 4.47: Impedance spectra of 150 nm thick LSC films deposited at 500°C on polycrystalline GDC measured at 600°C after 2 (light green), 6 (black), 10 (blue), 14 (green) and 20 (red) hours.

The electrode resistance of LSC thin films on YSZ increased while keeping the sample at 600°C or higher temperatures (degradation) (fig. 4.49). The degree of degradation strongly depends on the deposition parameters. The LSC thin film deposited at 630°C exhibits the highest electrode resistance and shows the strongest degradation of electrode resistance. Comparably little or almost no degradation within 20 hours is observed for thin films deposited at temperatures between 340 and 510°C. Between these lower deposition temperatures degradation behavior does not exhibit a clear systematic trend. However, LSC thin film electrodes deposited on polycrystalline YSZ as on single crystalline YSZ show the same electrochemical performance and degradation of resistance (see chapter PLD thin films on single crystalline YSZ). Also the capacitances of the semicircles are the same. Degradation is found in the same degree as for LSC on single crystalline YSZ. Activation of degraded electrodes with chemical etching was successful. There seems to be no significant difference in the electrochemical behavior of LSC, when deposited on different YSZ substrates.

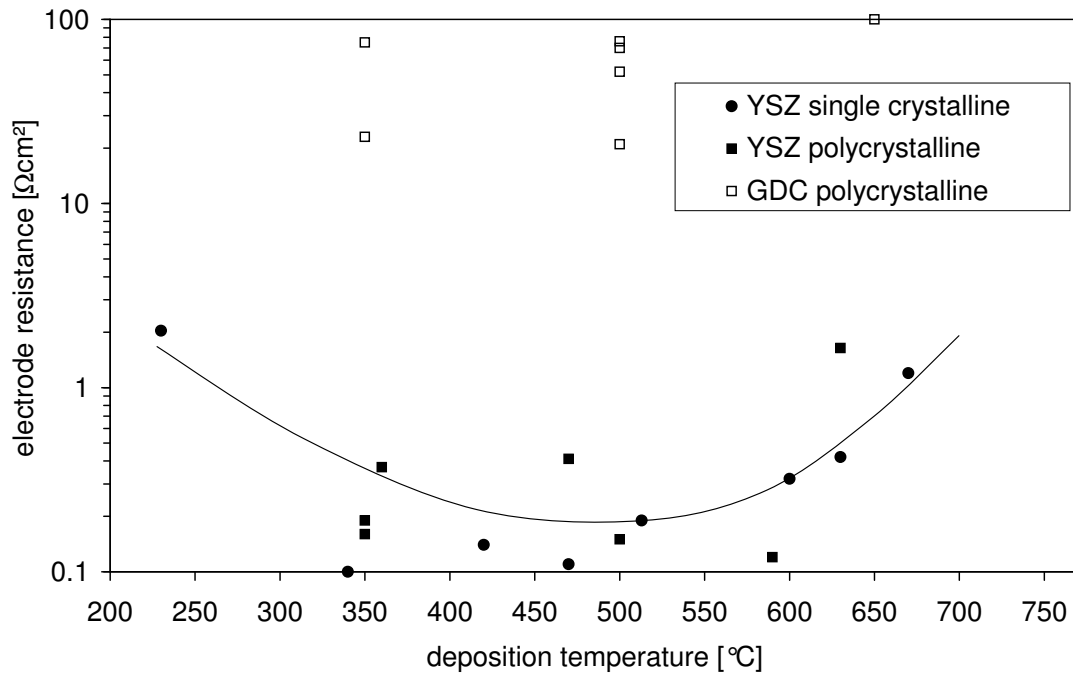


Figure 4.48: Dependence of the electrode resistance at 600 $^{\circ}\text{C}$ on the film deposition temperature for different substrates.

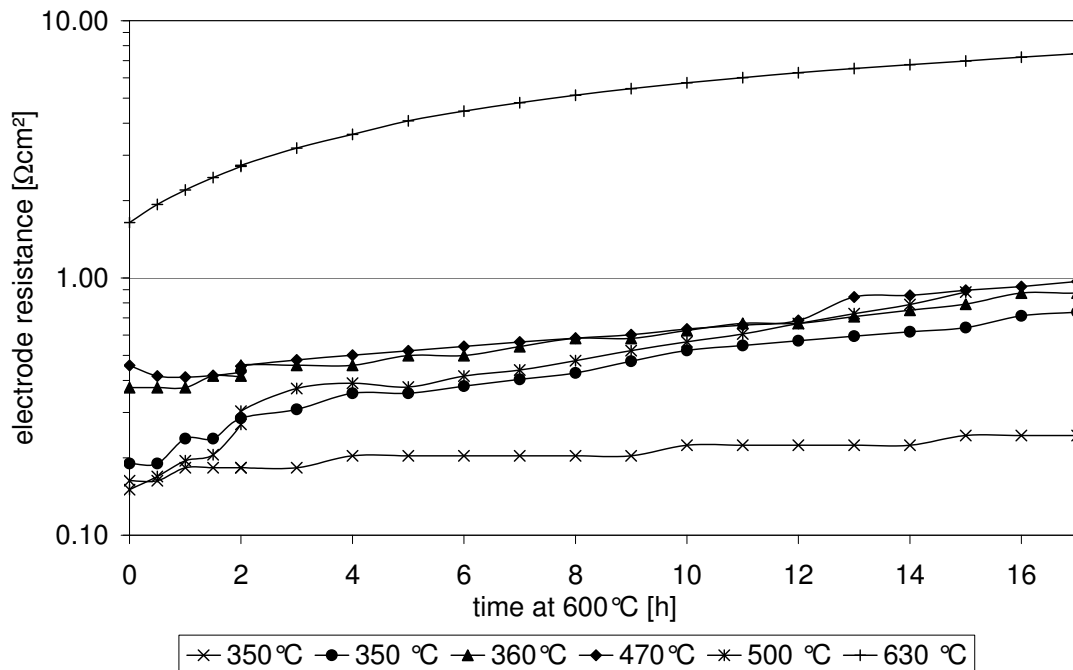


Figure 4.49: Electrode resistance as a function of time at 600 $^{\circ}\text{C}$ for LSC thin films (ca. 100 nm) deposited at different temperatures on polycrystalline YSZ.

LSC on polycrystalline GDC seems to have a different rate-determining step as the capacitance of the larger arc is several orders of magnitude smaller than of LSC on YSZ. This would also explain why the behavior of degradation is changed and no degradation is observable over 20 hours at 600°C. A decrease or change of resistance after a chemical etching with diluted HCl was not found. So the rate-determining step seems not to take place at the surface. If visible at all the surface incorporation is found to be quite fast (low frequency arc of ca. $1 \Omega\text{cm}^2$). There must be other processes than oxygen reduction in case of LSC on GDC, here causing higher resistances. In the SAD measurements it was shown that in contrast to LSC on YSZ the degree of crystallinity of the films is changed. The surface is more amorphous but still very active. As this LSC film on GDC was unusually thick the results may also be only partly representative. Further investigations are necessary to prove this observation.

4.4 LSC sol-gel thin films

4.4.1 Thin film characterization

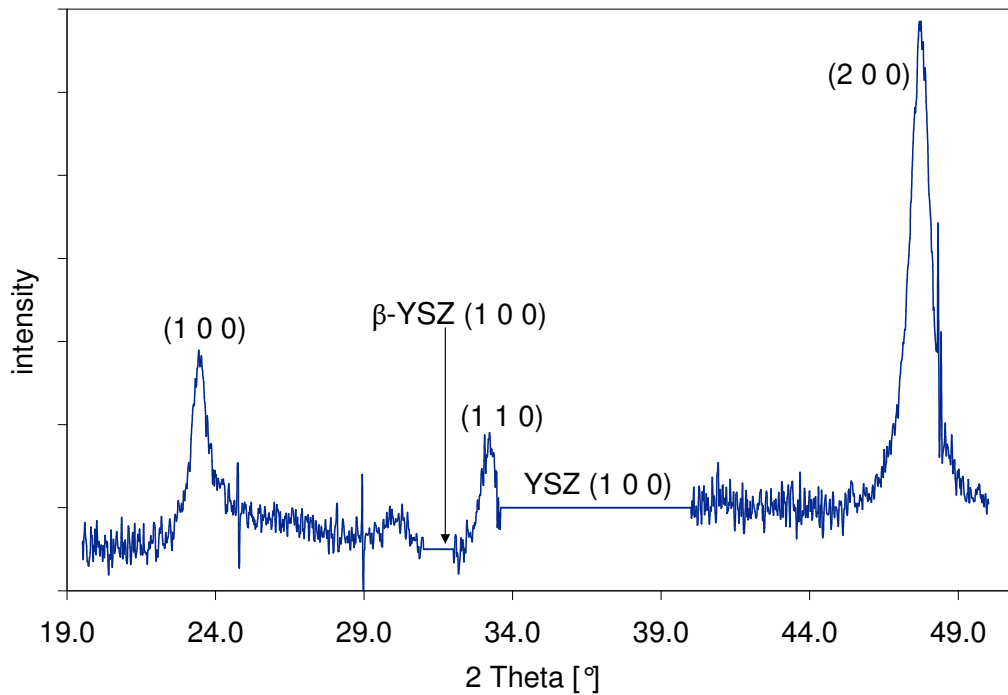


Figure 4.50: Difference of two diffraction patterns of a LSC electrode (2 sol-gel deposited layer) annealed at 600°C for 3 minutes and after 3 days at 600°C; the linearized regions correspond to the single crystalline YSZ substrate.

After annealing at 600°C or 700°C for 3 minutes and also after additional 15 minutes at 600°C the films did not show any signal of LSC in the diffraction pattern. After 3 days at 600°C however, diffraction peaks of rhombohedral (pdf 87-1081, R-3c) LSC can be observed (fig. 4.50).

The diagram was obtained by calibration and subtraction of two measurements, one after 3 minutes at 600°C and one after another 3 days at this temperature. The regions from 30 to 32° and 34 to 41° were excluded and linearized as they correspond to the single crystalline YSZ substrate. The resulting LSC thin film shows a preferential orientation along (1 0 0) and (1 1 0) in a hexagonal setting. So the thin films are XRD amorphous after short annealing but crystallize during the heat treatment at 600°C.

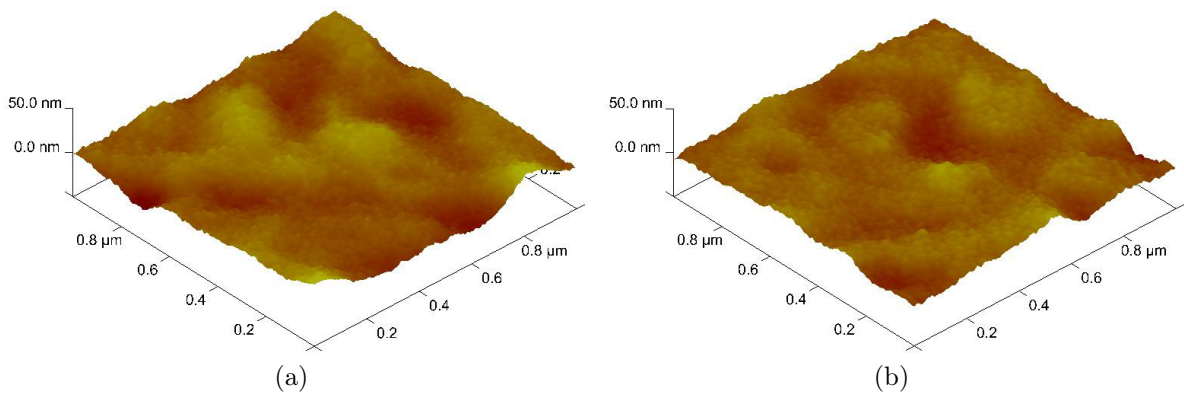


Figure 4.51: AFM images of LSC electrode annealed for 3 minutes at 500°C (a) and 700°C (b).

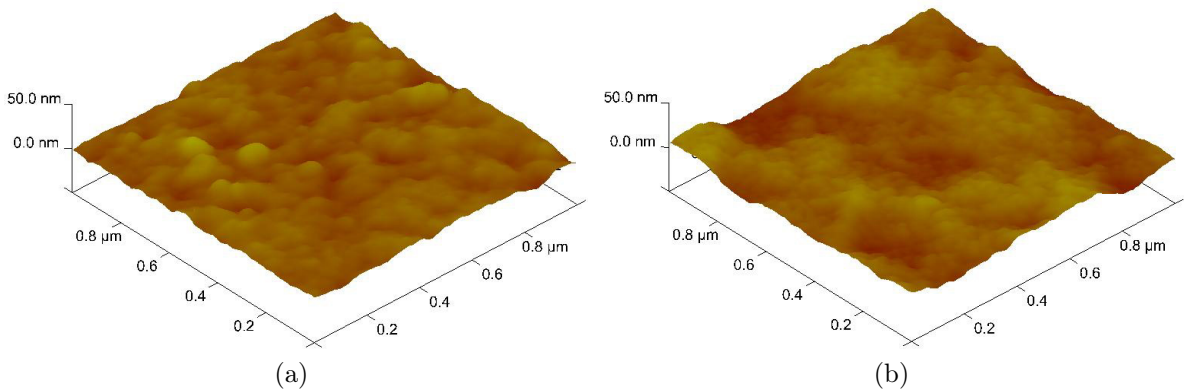


Figure 4.52: AFM images of LSC electrodes consisting of one (a) and two (b) sol-gel prepared layers thin film annealed at 600°C for 3 minutes.

AFM images of two-layer thin films annealed for 3 minutes at 500 (fig. 4.51a), 700°C

(fig. 4.51b) and 600°C (fig. 4.52b) are shown, respectively. The rms roughnesses of all two-layered thin films are between 3.5 and 6 nm and do not differ significantly for different annealing temperatures. After sol-gel processing of only one layer the annealed film has a slightly lower roughness value of 3 nm (fig. 4.52a). Some differences between one- and two-layered thin films are also visible in SEM images (fig. 4.54) with the two-layered thin film (fig. 4.54b) being rougher. Long-term annealing (3 days) even at 500°C lead to the growth of crystals on the surface (fig. 4.53).

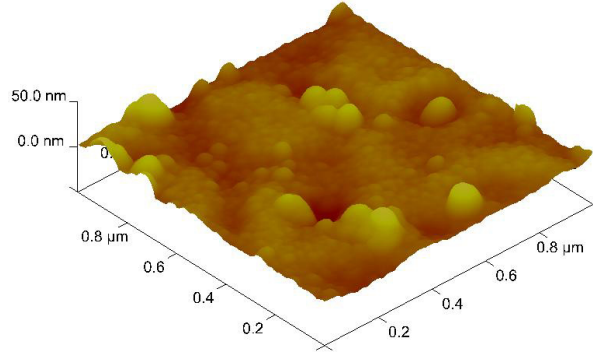


Figure 4.53: AFM image of a LSC electrode consisting of two sol-gel prepared layers annealed at 500°C for 3 minutes and then additional 3 days at 500°C.

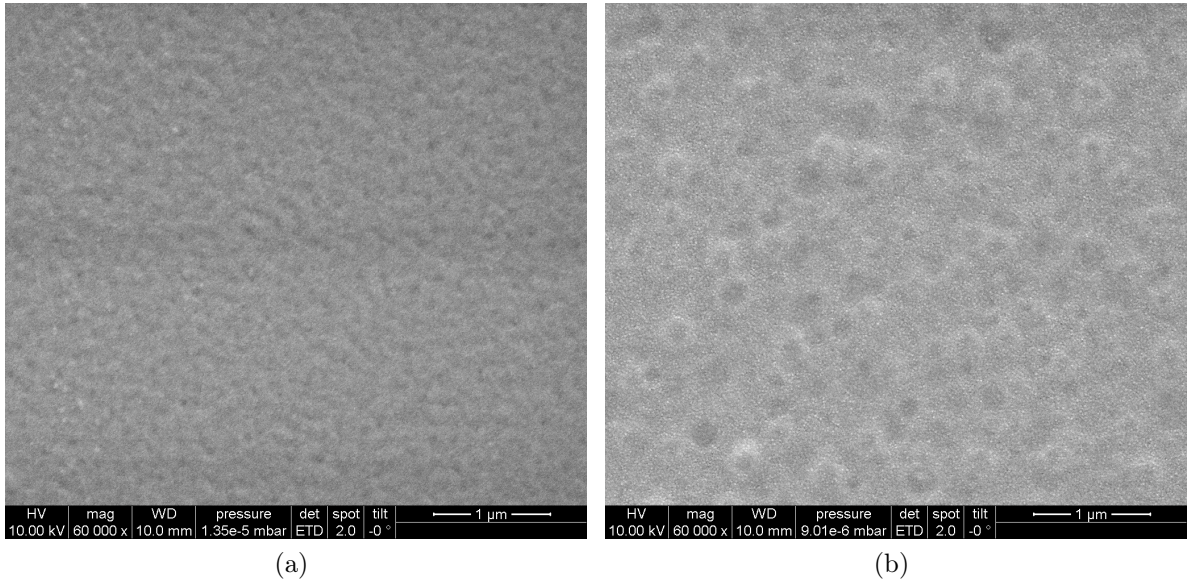


Figure 4.54: SEM images of LSC electrodes consisting of one (a) and two (b) sol-gel prepared layers annealed at 600°C for 3 minutes.

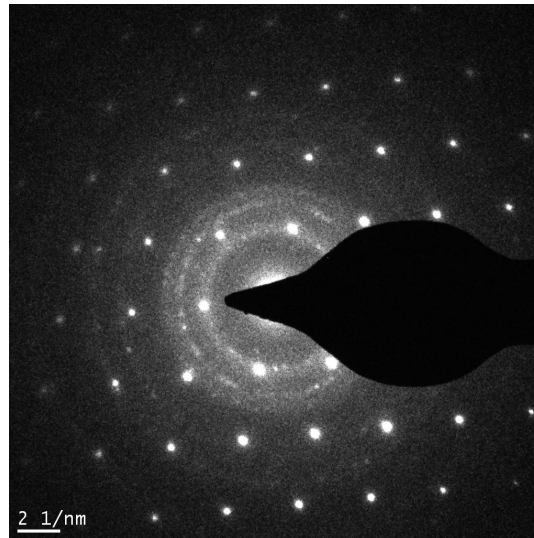


Figure 4.55: SAD pattern of a LSC electrode (two-layered) annealed for 3 minutes at 600°C.

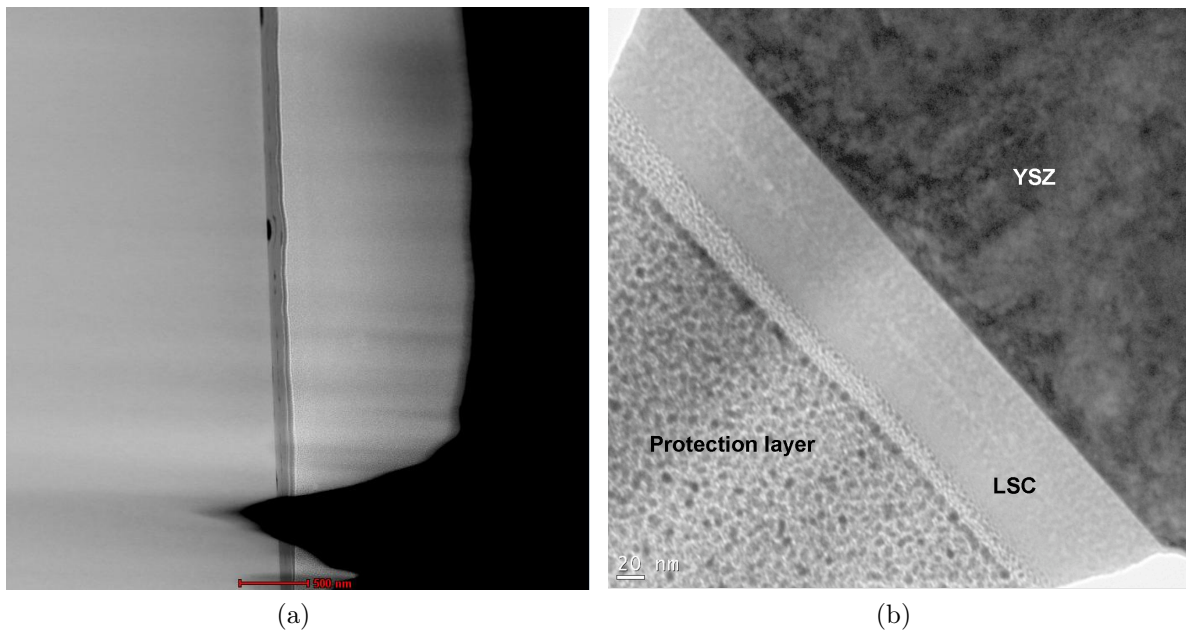


Figure 4.56: STEM image (a) and bright field image (b) of a two-layered LSC electrode annealed for 3 minutes at 600°C.

In the selected area diffraction pattern (fig. 4.55) the sharp spots correspond to the single crystalline YSZ substrate. The rings indicate amorphous and nanocrystalline LSC. Bright field TEM images (fig. 4.56a) and STEM images (fig. 4.56b) reveal a

constant thickness of the thin films over the entire length of the image. The interface between the two layers is still clearly visible with closed pores between the substrate and the first layer as well as between the first and second sol-gel prepared layer. The total film thickness is about 80 nm as one sol gel film has a thickness of 40 nm. No indication of pores in the individual sol-gel layers is found and thus an increased surface area due to open pores is not expected.

4.4.2 Electrochemical characterization

All electrochemical measurements were made on two-layered LSC thin film electrodes in microelectrode configuration. At 500°C, the impedance spectra exhibit one large semi-circle at low frequencies and a second smaller one, often overlapping with the first one, at intermediate frequencies (fig. 4.57).

After annealing at 600°C for 15 minutes only one semicircle remains observable, particularly for small polarization resistances. The fitted and calculated resistance and capacitance values of several samples are shown in table 4.7.

Polarization resistance at 500°C of LSC on single crystalline YSZ

The first impedances were measured at 500°C immediately after preparation (tab. 4.7). Electrodes on single crystalline YSZ have resistance values of about 50 Ωcm^2 . The thin film annealed at 700°C for 3 minutes has a much lower electrode resistance of 3.5 Ωcm^2 . All these resistance values are already smaller than those of LSC thin film electrodes PLD prepared and annealed at higher temperatures [9]. However, after 15 minutes at 600°C and cooling down back to 500°C the resistance values are even much smaller than before except for the sample first annealed at 700°C. Samples originally annealed at 500 and 600°C show a drastic decrease in resistance to about 1 Ωcm^2 at 500°C while the resistance of the 700°C sample stayed almost constant. A similar effect was already found for PLD deposited films (see chapter PLD thin films on single crystalline YSZ): High temperature deposited and thus more crystalline LSC thin films on YSZ have higher resistances compared to thin films prepared at lower temperature and lower crystallinity. The capacitance values (see tab. 4.7) corresponding to low frequency (lf) arcs of the LSC thin films are about 1-4 mF/cm². The capacitances for the intermediate frequency (if) arc is about 0.4 mF/cm². This capacitance values are in accordance with the PLD results reported by other groups [9,16] and fit to the well established model mentioned in section 2.3.3. The low frequency arc corresponds to the surface incorporation process of

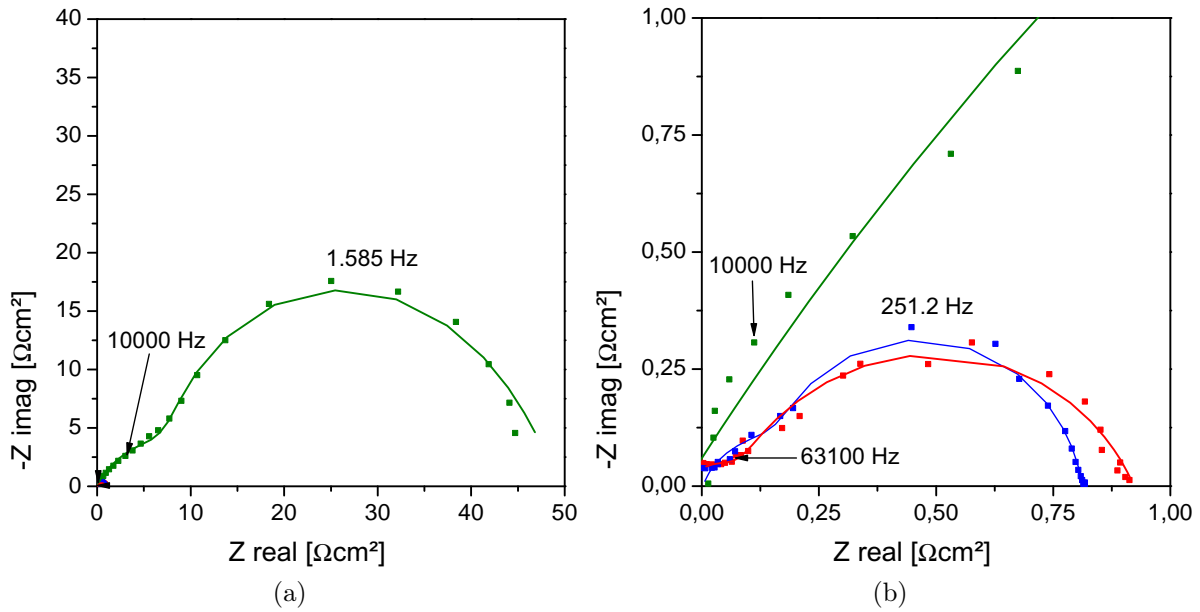


Figure 4.57: Impedance spectra of a LSC thin film (on single crystalline YSZ) annealed for 3 minutes at 500°C and measured at 500°C as prepared (green)(a), after 20 minutes at 600°C (blue), after 20 minutes at 600°C and 3 days at 500°C (red) (b). Bold lines are fit curves.

oxygen and the second, intermediate frequency arc to the interfacial process. If only one arc remains observable, e.g. often after 15 minutes annealing at 600°C, the dominating process is the surface incorporation of oxygen since the capacitance value is still about 1-4 mF/cm².

Most thin film electrodes show little or almost no degradation after 3 days at 500°C. The strongest degradation is observable for the thin film electrode first annealed at 700°C. In AFM images a growth of crystals of about 200 nm in length is becomes visible (fig. 4.53). However, these segregates seem to not affect the polarization resistances in this case, possibly because they cover only a small fraction of the entire surface of the samples after 3 days at 500°C (fig. 4.53).

Polarization resistance at 600°C of LSC on singlecrystalline YSZ

In fig. 4.58 the impedance spectra measured at 600°C in 2 minute intervals show the decrease of the electrode resistance in situ for an electrode first annealed for 3 minutes at 600°C. The reason could be a burning off and removing of residual organic compounds from the sol-gel preparation process. The fact that the film annealed for 3 minutes at 700°C is the only sample not showing this effect is also fitting to this explanation. After

some minutes at 600°C all sol gel thin films have very low resistance values between 0.1 and 0.5 Ωcm^2 (see tab. 4.7) with the thin film first annealed (3 min) at 700°C having the highest resistance. This sequence is in accordance with the results at 500°C. The high frequency intercept corresponding to the oxygen ion conduction in the electrolyte was not changed during this heat treatment. The electrode polarization resistances are again about two orders of magnitude lower than those reported for PLD films deposited and annealed above 750°C [21]. However, the values are comparable to those obtained for PLD films prepared at low deposition temperatures of 400-500°C (see chapter PLD thin films on single crystalline YSZ).

These results thus demonstrate that the effect of very low polarization resistances can be achieved with different preparation methods. Moreover it suggests that pores partly found in the low-temperature deposited PLD LSC electrodes are not the main origin of the low R_e values. Pores increasing the electrode surface area are not visible for these sol-gel prepared films (fig. 4.56b). Hence, the very low polarization resistance seems to be an intrinsic property of LSC films which have never been exposed to temperature much higher than 600°C. As the pores between the two individual sol-gel prepared LSC layers are closed, they are not increasing the real surface area of the electrodes and must not be taken into account when scaling the electrode resistance to the surface area. Also AFM images do not indicate a strong increase of the thin film surface due to roughness. Sol-gel films with a short annealing time at 500°C and 600°C do not show any significant XRD signals. As during a heat treatment the crystallinity is expected to increase this is in accordance with the PLD results, where more crystallized thin films showed a stronger degradation compared to thin films with already a very low degree of crystallinity (see chapter Degradation of electrode resistance). The LSC thin films with already very low degree of crystallinity were quite stable and less prone to crystallize compared to thin films with a higher degree of crystallinity. This could be the reason why the 700°C annealed sample shows stronger degradation compared to thin films annealed at 500 and 600°C. So there seems to be a correlation between crystallinity and electrode resistance. A change of the surface composition is a further possible explanation (see chapter XPS measurements). Moreover a change in electronic structure or different defect structures on the surface can be reasons for this very good performance towards oxygen reduction.

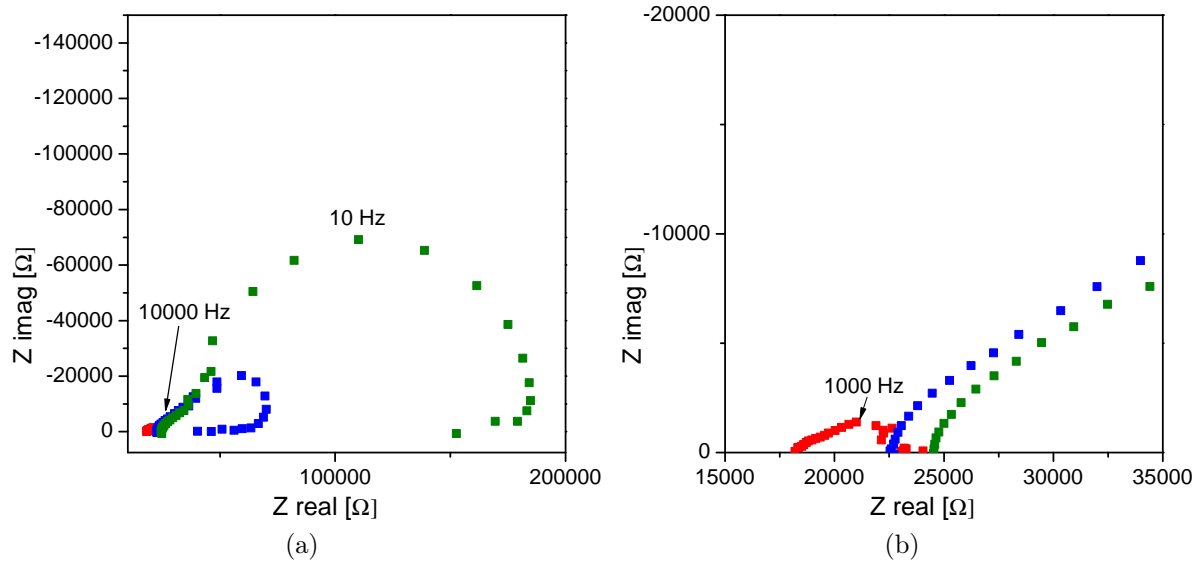


Figure 4.58: Impedance spectra of a LSC thin film on polycrystalline YSZ annealed at 600°C for 3 minutes and measured at 600°C after heating (green) and then every 2 minutes (blue, red). Spectra were recorded from high to low temperature with the loop indicating film changes during the measurement (a) and magnification of it (b).

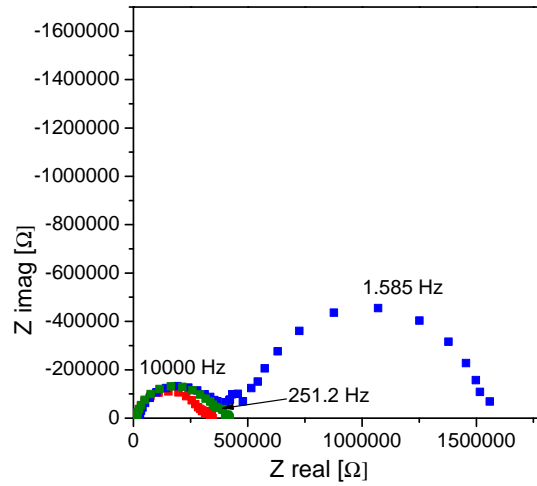


Figure 4.59: Impedance spectra of a LSC thin film on polycrystalline GDC annealed at 600°C for 3 minutes and measured at 500°C as prepared (blue), after 20 minutes at 600°C (red), after 20 minutes at 600°C and 3 days at 500°C (green).

Polarization resistance at 600°C of LSC on polycrystalline YSZ and GDC

After annealing at 600°C for 3+15 minutes thin films on polycrystalline YSZ have resistance values of about $0.15 \Omega\text{cm}^2$ at 600°C (tab. 1). These and all values obtained at other temperatures or annealing times show that there is no significant difference in polarization resistance between films on polycrystalline and single-crystalline YSZ. Further the capacitance values corresponding to low frequency (lf) and intermediate frequency (if) arc are very similar for both polycrystalline and single-crystalline YSZ. Hence it is possible to conclude that preparation of very active LSC electrodes is also possible on polycrystalline YSZ. This was also found for LSC films prepared by PLD (see chapter LSC thin films on polycrystalline YSZ and GDC).

However, the LSC electrode on polycrystalline GDC behaves very differently. Minimum values of R_e achievable at 500°C or 600°C are about an order of magnitude higher than those on YSZ. This, however, does not mean that the corresponding LSC surface is less active than on YSZ. The remaining low frequency arc after 15 min at 600°C annealing shows similarly low polarization values (about $1.5 \Omega\text{cm}^2$ at 500°C).

Table 4.7: Electrode resistance in Ωcm^2 of different sol-gel samples measured at different temperatures. (* after 15 minutes at 600°C)

Sample	500°C	600°C	(after 15 min at 600°C) 500°C	(after 3 days at 500°C) 500°C	Capacitances
LSC on single crystalline YSZ (500°C annealed)	46.6	0.10*	0.81	1.12	ca. 0.4 mF/cm^2 (if) and $1-4 \text{ mF/cm}^2$ (lf)
LSC on single crystalline YSZ (600°C annealed)	54.6	0.15*	1.00	1.32	ca. 0.4 mF/cm^2 (if) and $ca.1-4 \text{ mF/cm}^2$ (lf)
LSC on single crystalline YSZ (700°C annealed)	3.5	0.50	2.86	4.04	ca. 0.4 mF/cm^2 (if) and $ca. 1-4 \text{ mF/cm}^2$ (lf)
LSC on poly crystalline YSZ (600°C annealed)	53.9	0.14*	1.60	1.59	ca. 0.4 mF/cm^2 (if) and $ca. \text{ mF/cm}^2$ (lf)
LSC on poly crystalline GDC (600°C annealed)	37.2	2.00*	8.8	11.6	ca. $2 \mu\text{F/cm}^2$ (if) and $ca. 1 \text{ mF/cm}^2$ (lf)

Interestingly there is also a difference in capacitances between thin films on GDC and YSZ. The capacitance values of the thin films on the polycrystalline GDC are $0.5-2 \text{ mF/cm}^2$ for the low frequency arc and $1.6-2.2 \mu\text{F/cm}^2$ for the intermediate frequency

arc (tab. 4.7). After 15 minutes at 600°C the disappearing arc in the spectra of LSC on GDC is the low frequency arc with the 0.5-2 mF/cm² capacitance (fig. 4.59) judging from the capacitance value. This arc refers to the surface incorporation of oxygen. The remaining larger arc thus corresponds to an interfacial process at the electrode-electrolyte interface and its capacitance in the range of $\mu\text{F}/\text{cm}^2$ is much smaller than those for LSC on YSZ. This is quite surprising as normally YSZ is supposed to cause an interface resistance due to the formation of insulating zirconate between LSC and YSZ [5]. The very low interfacial capacitance suggests that a relatively thick layer at the CGO/LSC interface causes a polarization resistance. Assuming a relative permittivity of 10-20 for this layer it is expected to be ca. 5-10 nm thick (calculated from C_i) and has a conductivity of about 10^{-7} S/cm. The conductivity is the same as found for LSC on GDC prepared by PLD (see Electrochemical characterization of chapter LSC thin films on polycrystalline YSZ and GDC) but the thickness of the layers differ significantly. Again the origin of this resistive layer is not known yet. It might be a second phase or LSC exhibiting strongly different defect densities or mobilities due to the growth on GDC.

4.5 XPS measurements

As LEIS is a method limited or specialized to the first monolayer of the surface, additional XPS measurements were performed to investigate the surface composition and the valence states of different LSC thin films. PLD samples with different deposition temperatures (450 and 650°C) and different deposition times (25 and 50 minutes), before and after a heat treatment (in the following denoted as HT) and after chemical etching (10 seconds 0.14 mol/L HCl) are investigated. Further a 450°C LSC thin film on polycrystalline YSZ and a LSC sol-gel thin film on single crystalline YSZ annealed at 500°C were chosen as representative samples. The deposition time of 50 minutes lead to a film thickness of only about 70 nm. All samples and parameters are listed in table 4.8.

The first focus of evaluation was the chemical composition of the surface. In fig. 4.60 the ratio of Sr to the total A-site concentration (Sr+La) on the surface is shown for different samples. The number 60 denotes the more surface sensitive measurements. Much more C and O contamination signal observed in this measuring mode, confirms that the 60 degree mode is more surface sensitive. The Sr/(Sr+La) ratio seems to be pretty uniform within the XPS sampling depth and there are no significant differences between the

Table 4.8: XPS samples

Sample	Growth technique	Growth temperature	Heat treated	Deposition time	Substrate
450C	PLD	450°C	no	50 min	YSZ single
450 HT	PLD	450°C	3 days at 600°C	50 min	YSZ single
450C thin	PLD	450°C	no	25 min	YSZ single
650C	PLD	650°C	no	50 min	YSZ single
650 HT	PLD	650°C	3 days at 600°C	50 min	YSZ single
450 poly	PLD	450°C	no	50 min	YSZ poly
500 SG	Sol gel	500°C	no		YSZ single

different samples and the different sampling depths. However, also in XPS like in LEIS no absolute concentrations of the elements are achievable without standards or exact theoretical considerations about LSC. For the evaluation the peak area for the different elements was divided by their sensitivity factor given by Omicron. Looking at the A/B ratio (fig. 4.61) more differences are observable. For all samples a much higher A/B ratio than 1 is found. Furthermore the relative Co-content of electrodes exhibiting low resistances is higher compared to electrodes exhibiting higher polarization resistances. An exception is the 650°C annealed sample which shows no significant change in terms of surface cation composition upon annealing compared to the as prepared state. However, the general trend is consistent as Co with its more flexible valence states is considered to play a key-role in the electron transfer from the electrode to the oxygen atoms or molecules. Imanishi et al. found a correlation between an increased cobalt concentration on the surface and a decreasing polarization resistance [75].

The exception of the annealed sample could be explainable if the degradation of the polarization resistance was caused by a different effect than the differences in resistance of the as prepared electrodes. That degradation and the differences of as prepared samples in resistance arise from different processes fits with the results for the activation energies. The activation energy for as prepared and degraded 450°C deposited samples is always about 1.34 eV while for a 650°C deposited sample it was 1.77 eV. After a heat treatment of 3 days at 600°C an activation energy of 2.43 eV was calculated for a higher temperature regime. The latter increase may also be related to different temperature regimes and has certainly to be reproduced on more samples. The differences between the

activation energies of 450 and 650°C deposited samples without any heat treatment may indicate different processes but have to be also reproduced for more profound discussions. This would fit with the explanation that differences due to deposition temperature and the behavior of degradation are related to different processes.

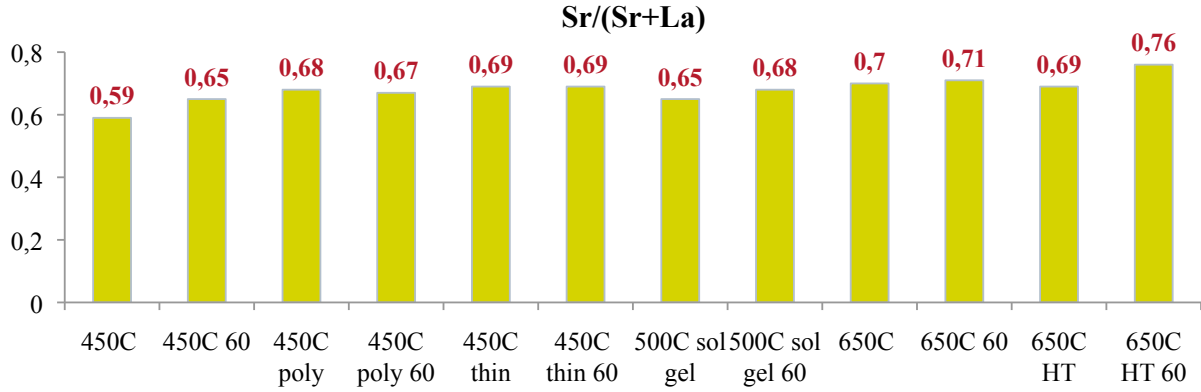


Figure 4.60: Sr/(Sr+La) ratio considering all Sr species.

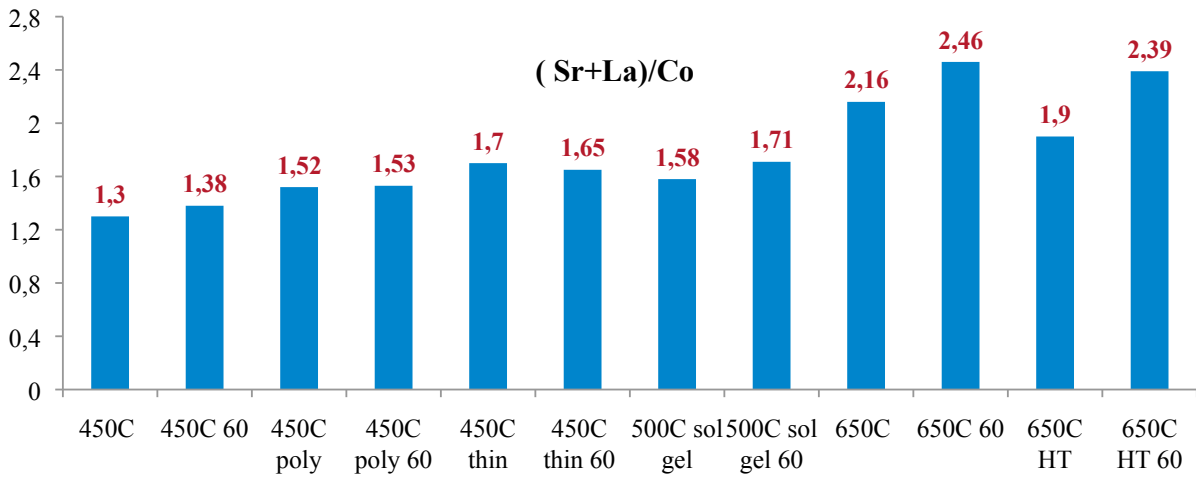


Figure 4.61: (Sr+La)/Co ratio considering all Sr species.

When analyzing the shape and structure of the peaks additional information on the valence state and chemical bondings becomes available. In fig. 4.62 a high intensity Sr 3d peak at ca. 2eV -higher than the lattice Sr peaks- was found, suggesting existence of Sr-OH or Sr – CO₃ groups (even after cleaning the samples in air furnace at 600°C for 1.5 hours) [84]. When dividing the peak shape into surface and lattice Sr an evaluation of the Sr/(Sr+La) and A/B ratio only considering lattice Sr can be made.

This does not influence the trends qualitatively seen in fig. 4.60 and 4.61. Again no significant differences in Sr/(Sr+La) ratio and increased A/B ratios for electrodes with lower performance are found (fig. 4.63 and 4.64).

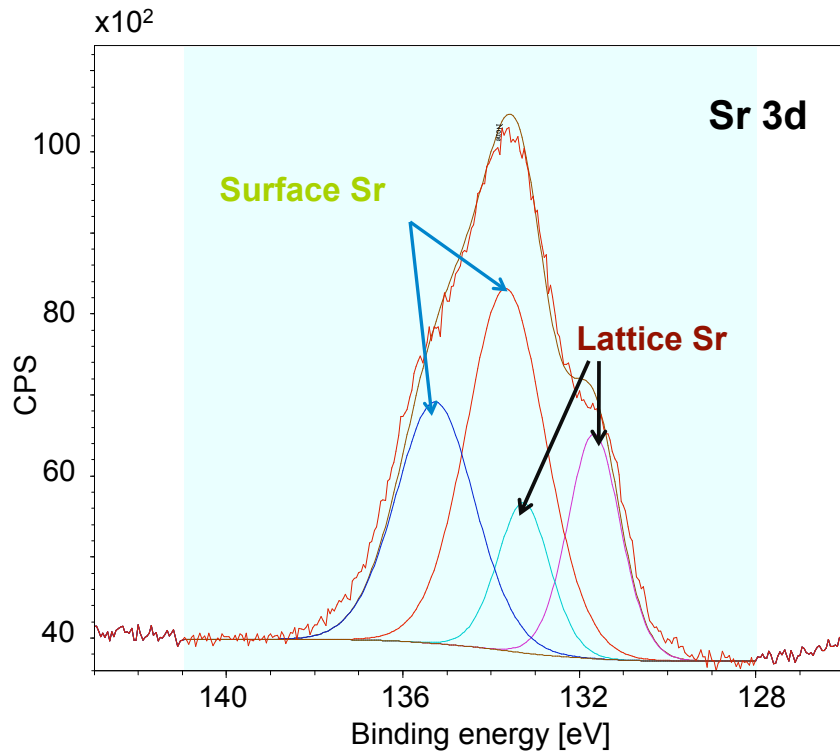


Figure 4.62: (Sr 3d peak with contributions from lattice and surface Sr.

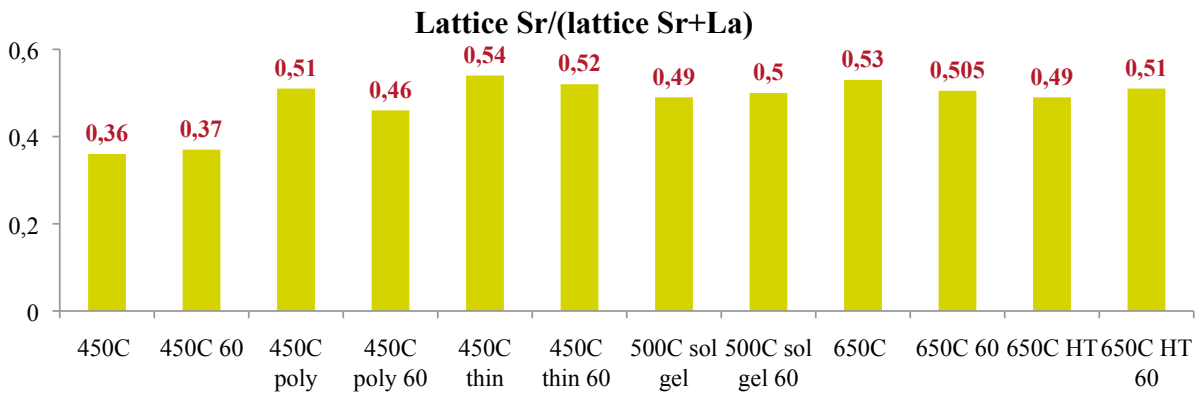


Figure 4.63: Sr/(Sr+La) ratio only considering surface Sr.

The Co 2p peaks of films grown at 650°C and 450°C showed differences in the existence of satellite peaks (fig. 4.65), which might suggest different ratios of Co^{3+} and Co^{2+} in

these films. For pure LaCoO_3 with pure Co^{2+} state no satellite peaks are found [85]. The appearance of a weak satellite peak (at 790 eV) is characteristic for Co_3O_4 where mixed Co^{3+} and Co^{2+} valence states are present [85]. So there are differences in Co 2p peaks between electrodes exhibiting very low and very high polarization resistances. For the interpretation also the role of surface roughness and the observed growth of crystallites on the surface during a heat treatment has to be considered.

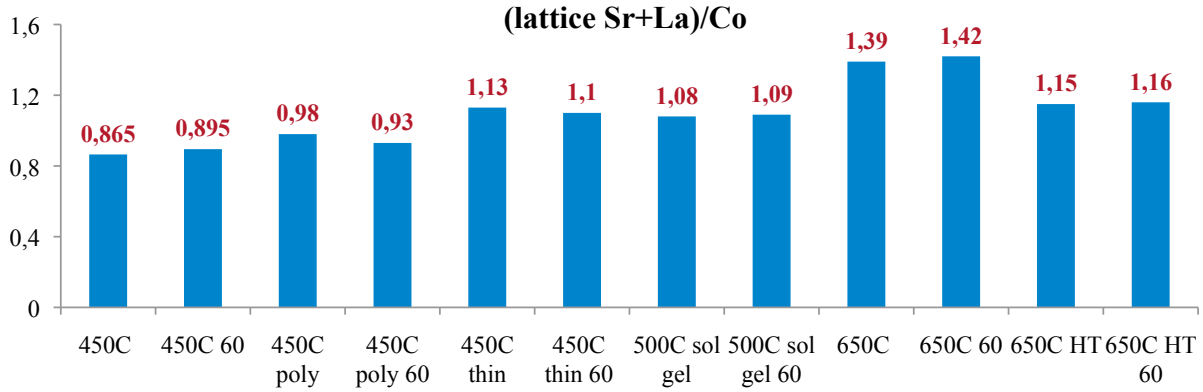


Figure 4.64: (Sr+La)/Co ratio only considering surface Sr.

The differences to LEIS results need to be discussed. Possibly the increased Sr content in the first monolayer found in the LEIS measurements corresponds to the SrCO_3 on the surface found on all samples, including the 450°C samples. Moreover all XPS samples were kept 1 1/2 hours at 600°C for cleaning before the samples were measured. Maybe after this time Sr already segregated to the surface. In LEIS all samples were measured as prepared.

XPS surface sensitivity is always exponentially higher at the surface compared to sub-surface, even though the sampling comes from a finite depth (definitely beyond the top 1-2 layers). Co is much more surface sensitive because it is at much lower kinetic energy. The low angle measurements are a strong means for making the collected data more surface sensitive, but this best applies if the samples are smooth which is only partially the case. However, clear differences in the surface Sr content through SrCO_3 in the XPS data as a function of angle is found.

In XPS and LEIS a real quantification of the results is not possible without external standards. However, the question arises if the cation composition is sufficient to explain most results of this thesis. The chemical environment and valence states especially of Co and the oxygen vacancy concentration on the surface are certainly also very important factors governing the oxygen reduction. Also the nature of a SrO or SrCO_3 segrega-

tion as separated crystals or as dense film with a certain thickness needs to be further investigated.

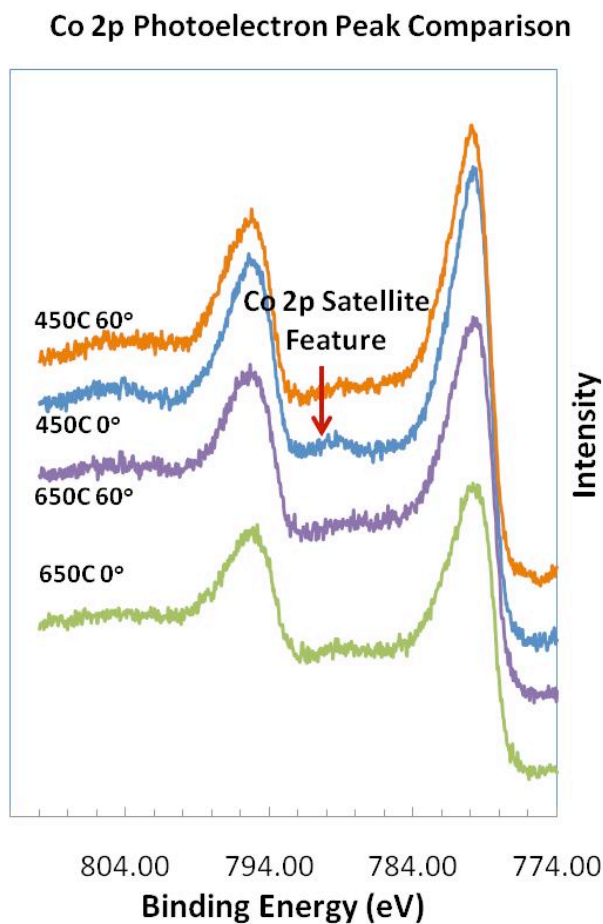


Figure 4.65: Co peak shape comparison on the LSC films deposited at 450°C and 650°C indicating different Co oxidation states.

5 Conclusions

In this thesis $\text{La}_{0.6}\text{Sr}_{0.4}\text{CoO}_{3-\delta}$ thin films were prepared by PLD and a simple sol-gel route. The electrochemical performance towards oxygen reduction was investigated by impedance spectroscopy. Structural and morphological investigations were performed using XRD, SEM, AFM and TEM. The surface composition was investigated by LEIS and XPS. From that data several structure-property relations were found.

The structure and electrochemical performance of $\text{La}_{0.6}\text{Sr}_{0.4}\text{CoO}_{3-\delta}$ thin-film electrodes prepared by PLD on single crystalline YSZ strongly depends on the deposition temperature of the films. As expected, films become less crystalline when depositing at lower YSZ substrate temperature. Surprisingly, 40 and 200 nm thin films deposited at rather low temperatures (340-510°C) and exhibiting hardly any signal in Bragg-Brentano XRD patterns showed the best electrochemical performance. It was possible to prepare LSC film electrodes with polarization resistances as low as $0.1 \Omega\text{cm}^2$ at 600°C. Many electrodes showed a pronounced degradation when operating between 500 and 700°C. Interestingly, the films exhibiting the lowest resistances showed the lowest degradation within a few days of operation.

The activation energy of the polarization resistance was found to be 1.34 eV for thin films deposited around 450°C and 1.77 for a thin film deposited at 650°C. After 3 days at 600°C an activation energy of 2.43 eV for the higher deposited thin film (measured in a different temperature regime) was found.

The electronic conductivity becomes smaller with decreasing deposition temperature and thus decreasing degree of crystallinity. However, several hundred S/cm are still measured for XRD-amorphous films.

An activation by chemical etching and voltage was found for several samples. The activation by chemical etching was not observed for LSC electrodes deposited on polycrystalline GDC. Accordingly the fast oxygen incorporation and its degradation of LSC on YSZ is thought to be related to changes of surface structure and chemistry.

The Sr doping concentration influences the electrochemical performance with the highest polarization resistances found for the lowest Sr content. A substitution of Co by Fe

was investigated. The performance of amorphous $\text{La}_{0.6}\text{Sr}_{0.4}\text{Co}_{1-y}\text{Fe}_y\text{O}_{3-\delta}$ electrodes was decreasing with increasing y and measurable impedance spectra were achieved most of the time only above 700°C , i. e. after a certain crystallization.

When depositing the same electrodes on polycrystalline YSZ instead of single crystalline YSZ no significant difference in electrochemical performance was found. However, the deposition of LSC on polycrystalline GDC results in higher resistances most probably related to a different rate determining step as profound differences in the corresponding capacitances are found.

It was possible to employ a sol-gel route to prepare electrodes with the same performance as the electrodes prepared by PLD. Again it seems that there is a correlation between the degree of crystallinity and the resistance. An annealing temperature of 500°C is not sufficient for good electrodes but annealing thin films at 600°C lead to very low polarization resistances. Thin films annealed at 700°C have higher resistance values. The choice of substrate again influences the resistance. On (single and polycrystalline) YSZ, thin film electrodes have smaller electrode resistances compared to thin films grown on polycrystalline GDC. The corresponding capacitances with the resistance values are in accordance to the PLD-grown LSC on polycrystalline GDC. So also the LSC thin films prepared by a sol-gel route seem to have a different rate determining step.

As the sol-gel thin films are smooth and dense and have no open porosity this extremely fast oxygen reduction cannot be attributed to a strongly increased surface area. It seems to be related to the lower crystallinity or a consequence of the lower crystallinity. So most effects found in this thesis are reproducible with two completely different preparation methods.

The surface composition was investigated by LEIS and XPS. Different results concerning the surface composition of as prepared and heat treated samples deposited at 450°C and 650°C are achieved. In LEIS a correlation between increased Sr/La ratio and higher resistance values was found. Further, LEIS indicates absence of Co in the first monolayer of the surface. In XPS no variation in the $\text{Sr}/(\text{Sr}+\text{La})$ ratio for different samples was found. However, all samples were heat treated for 1.5 hours at 600°C for cleaning and possibly this already influenced the surface composition. Also different measuring depths and sensibilities of the different methods have to be taken into account. A full explanation of the results is thus not possible at the moment.

From these results several conclusions can be drawn regarding the application of mixed conducting electrodes in solid oxide fuel cells: i) Surfaces of LSC film electrodes and conventional porous LSC electrodes are usually exposed to temperatures which cause

full crystallisation and thus probably a distinct thermal deactivation of the surfaces. This thesis showed that LSC surfaces could be orders of magnitude more active when prepared at sufficiently low temperatures. ii) It may thus be promising to fabricate porous or infiltrated electrodes, exclusively at low temperatures by a sol-gel route without full crystallization of the electrodes. By avoiding any subsequent high temperature treatment the resulting surfaces may exhibit very fast oxygen exchange kinetics. Porous electrodes having the same surface properties as the best films of this thesis ($0.1 \Omega\text{cm}^2$ at 600°C and below $1\Omega\text{cm}^2$ at 500°C) might operate satisfactorily at temperatures below 500°C . Results in accordance with these conclusions were also reported by Peters et al. [64] iii) There is a reasonable chance for fabricating stable thin film electrodes of sufficient electrochemical activity at operation temperatures below 600°C which may, for example, be applicable in micro fuel cells for which preparation procedures compatible with standard (Si-) micro technology are desirable. The values of about $0.1 \Omega\text{cm}^2$ are two to three orders of magnitude smaller than resistances reported in literature for high temperature deposited LSC films [9]. It should also be emphasized that these extremely low resistances were obtained for dense (sol-gel) electrode films rather than for porous electrodes with strongly enhanced true surface area per given electrolyte base area.

6 List of Abbreviations

AFM	atomic force microscope
BF	bright field
CE	counter electrode
FEGSEM	field emission gun scanning electron microscope
FIB	focussed ion beam
GADDS	general area detector diffraction system
GDC	gadolinia doped ceria
IS	impedance spectroscopy
LEIS	low energy ion scattering
LOM	light optical microscope
LSC	generally: lanthanum strontium cobaltite; in this thesis: $\text{La}_{0.6}\text{Sr}_{0.4}\text{CoO}_{3-\delta}$
LSC82	$\text{La}_{0.8}\text{Sr}_{0.2}\text{CoO}_{3-\delta}$
LSC64	$\text{La}_{0.6}\text{Sr}_{0.4}\text{CoO}_{3-\delta}$
LSC46	$\text{La}_{0.4}\text{Sr}_{0.6}\text{CoO}_{3-\delta}$
LSCF	lanthanum strontium cobalt iron oxide
LSCF6437	$\text{La}_{0.6}\text{Sr}_{0.4}\text{Co}_{0.3}\text{Fe}_{0.7}\text{O}_{3-\delta}$
LSF	generally: lanthanum strontium iron oxide; in this thesis: $\text{La}_{0.6}\text{Sr}_{0.4}\text{FeO}_{3-\delta}$
LSM	lanthanum strontium manganite
ME	measuring electrode
PLD	pulsed laser deposition
rds	rate determining step
rms	root mean square
SAD	selected area diffraction
SEM	scanning electron microscope
SOFC	solid oxide fuel cell
STEM	scanning transmission electron microscope
TEM	transmission electron microscope
TOF SIMS	time of flight secondary ion mass spectrometry
XPS	x-ray photoelectron spectroscopy
XRD	x-ray diffraction
YSZ	yttria stabilized zirconia

7 List of Symbols

δ	oxygen nonstoichiometry
μ	mobility of charge carriers
σ	conductivity
ω	angular frequency
ω_r	relaxation frequency
C	capacitance
C_{chem}	chemical capacitance
C_i	interfacial capacitance
c_O	total concentration of lattice oxygen
D	diffusion coefficient
e	elementary charge
E_a	activation energy
H	Haven ratio
k	oxygen exchange coefficient
k_B	Boltzmann constant
n	exponent in Q-C relation characterizing the deviation of Q from an ideal capacitance or concentration of excess electrons
p	concentration of electron holes
p_{O_2}	oxygen partial pressure
Q	constant phase element
R	resistance
R_b	bulk resistance
R_i	interface resistance
R_e	electrode resistance (sum of all resistances corresponding to the electrode)
R_s	surface resistance
T	temperature
$T_{\text{dep.}}$	deposition temperature
x	A side ratio of the perovskite composition
y	Bside ratio of the perovskite composition
z	charge number
Z_{imag}	imaginary part of the complex impedance plane
Z_{real}	real part of the complex impedance plane
Z_{RC}	total complex impedance
Z_Q	impedance of the capacitance

Bibliography

- [1] W. R. Grove. *Philos. Mag.*, 14:127–130, 1839.
- [2] S. B. Adler. *Chemical Reviews*, 104:4791–4843, 2004.
- [3] J.M. Vohs and R.J. Gorte. *Advanced Materials*, 21:1–14, 2009.
- [4] T. Kawada and H. Yokokawa. *Key Engineering Materials*, 125-126:187–248, 1997.
- [5] O. Yamamoto, Y. Takeda, R. Kanno, and M. Noda. *Solid State Ionics*, 22:241–246, 1987.
- [6] A. Endo, H. Fukunaga, C. Wen, and K. Yamada. *Solid State Ionics*, 135(1-4):353–358, 2000.
- [7] T. Kawada, M. Sase, J. Suzuki, K. Masuda, K. Yashiro, A. Kaimai, Y. Nigara, J. Mizusaki, K. Kawamura, and H. Yugami. *Proceedings - Electrochemical Society*, 2001-16(Solid Oxide Fuel Cells VII):529–538, 2001.
- [8] Y. L. Yang, A. J. Jacobson, C. L. Chen, G. P. Luo, K. D. Ross, and C. W. Chu. *Applied Physics Letters*, 79(6):776–778, 2001.
- [9] F. S. Baumann, J. Fleig, H.-U. Habermeier, and J. Maier. *Solid State Ionics*, 177:1071–1081, 2006.
- [10] N. Pryds, B. Toftmann, J. Schou, P.V. Hendriksen, and S. Linderorth. *Applied Surface Science*, 247:466–470, 2006.
- [11] X. Chen, S. Wang, Y. L. Yang, L. Smith, N. J. Wu, B.-I. Kim, S. S. Perry, A. J. Jacobson, and A. Ignatiev. *Solid State Ionics*, 146(3,4):405–413, 2002.
- [12] N. Imanishi, T. Matsumura, Y. Sumiya, K. Yoshimura, A. Hirano, Y. Takeda, D. Mori, and R. Kanno. *Solid State Ionics*, 174(1-4):245–252, 2004.

- [13] D. Mori, H. Oka, Y. Suzuki, N. Sonoyama, A. Yamada, R. Kanno, Y. Sumiya, N. Imanishi, and Y. Takeda. *Solid State Ionics*, 177:535–540, 2006.
- [14] M. Sase, J. Suzuki, K. Yashiro, T. Otake, A. Kaimai, T. Kawada, J. Mizusaki, and H. Yugami. *Solid State Ionics*, 177(19-25):1961–1964, 2006.
- [15] E. Koep, C. Jin, M. Haluska, R. Das, R. Narayan, K. Sandhage, R. Snyder, and M. Liu. *Journal of Power Sources*, 161:250–255, 2006.
- [16] T. Kawada, J. Suzuki, M. Sase, A. Kaimai, K. Yashiro, Y. Nigara, J. Mizusaki, K. Kawamura, and H. Yugami. *Journal of the Electrochemical Society*, 149(7):E252–E259, 2002.
- [17] Y. L. Yang, C. L. Chen, S. Y. Chen, C. W. Chu, and A. J. Jacobson. *Journal of the Electrochemical Society*, 147(11):4001–4007, 2000.
- [18] X. Chen, N. J. Wu, and A. Ignatiev. *Journal of the European Ceramic Society*, 19(6-7):819–822, 1999.
- [19] H. D. Bhatt, R. Vedula, S. B. Desu, and G. C. Fralick. *Thin Solid Films*, 350:249–257, 1999.
- [20] L. G. Coccia, G. C. Tyrrell, J. A. Kilner, D. Waller, R. J. Chater, and I. W. Boyd. *Applied Surface Science*, 96-98:795–801, 1996.
- [21] F. S. Baumann, J. Fleig, G. Cristiani, B. Stuhlhofer, H. U. Habermeier, and J. Maier. *Journal of the Electrochemical Society*, 154(9):B931–B941, 2007.
- [22] F. S. Baumann, J. Fleig, M. Konuma, U. Starke, H.-U. Habermeier, and J. Maier. *Journal of the Electrochemical Society*, 152(10):A2074–A2079, 2005.
- [23] F. S. Baumann, J. Maier, and J. Fleig. *Solid State Ionics*, 179(21-26):1198–1204, 2008.
- [24] J. Fleig. *Habilitation, Universität Ulm*, 2002.
- [25] J. Maier. *Solid State Ionics*, 112(3-4):197–228, 1998.
- [26] J. Maier. John Wiley and Sons, 1st edition edition, 2004.
- [27] L. W. Tai, M. M. Nasrallah, H. U. Anderson, D. M. Sparlin, and S. R. Sehlin. *Solid State Ionics*, 76(3,4):273–83, 1995.

- [28] J. Ovenstone, J. S. White, and S. T. Misture. *Journal of Power Sources*, 181(1):56–61, 2008.
- [29] R. H. E. van Doorn and A. J. Burggraaf. *Solid State Ionics*, 128:65–78, 2000.
- [30] F.A. Kröger and H. J. Vink. *Solid State Physics Advances in Research and Applications*, volume 3, p 307. Academic, New York, 1957.
- [31] S. Wang, M. Katsuki, M. Dokiya, and T. Hashimoto. *Solid State Ionics*, 159(1-2):71–78, 2003.
- [32] J. Fleig and J. Maier. *Journal of the European Ceramic Society Electroceramics VIII*, 24(6):1343–1347, 2004.
- [33] T. Kawada, K. Masuda, J. Suzuki, A. Kaimai, K. Kawamura, Y. Nigara, J. Mizusaki, H. Yugami, H. Arashi, N. Sakai, and H. Yokokawa. *Solid State Ionics*, 121(1-4):271–279, 1999.
- [34] E. Bucher, W. Jantscher, A. Benisek, W. Sitte, W. Preis, I. Rom, and F. Hofer. *Solid State Ionics*, 141-142:375–380, 2001.
- [35] A. N. Petrov, V. A. Cherepanov, and A. Yu Zuev. *Journal of Solid State Electrochemistry*, 10(8):517–537, 2006.
- [36] L. W. Tai, M. M. Nasrallah, H. U. Anderson, D. M. Sparlin, and S. R. Sehlin. *Solid State Ionics*, 76(3,4):259–71, 1995.
- [37] E. Bucher, W. Sitte, I. Rom, I. Papst, W. Grogger, and F. Hofer. *Solid State Ionics*, 152-153:417–421, 2002.
- [38] W. Bao, Q. Chang, R. Yan, and G. Meng. *J. Membr. Sci.*, 252(1-2):175–181, 2005.
- [39] R. Eason. *Pulsed Laser Deposition of Thin Films*. John Wiley and Sons, New Jersey, 2007.
- [40] J. Brinker. *Sol-Gel Science: The Physics and Chemistry of Sol-Gel Processing*. Academic Press, Inc., New York, 1990.
- [41] J. E. Bauerle. *J. Phys. Chem. Solids*, 30:2657, 1969.
- [42] J. Fleig. *Solid State Ionics*, 150:181–193, 2002.

- [43] J. Jamnik and J. Maier. *Phys. Chem.*, 3, 2001.
- [44] V. Brichzin, J. Fleig, H. U. Habermeier, G. Christiani, and J. Maier. *Solid State Ionics*, 152-153:499–507, 2002.
- [45] H. Fukunaga, M. Koyama, N. Takahashi, C. Wen, and K. Yamada. *Solid State Ionics*, 132(3,4):279–285, 2000.
- [46] A. Bieberle-Huetter and H. L. Tuller. *Journal of Electroceramics*, 16(2):151–157, 2006.
- [47] A. Ringuede and J. Guindet. *Ionics*, 3(3 and 4):256–260, 1997.
- [48] L. Dieterle, D. Bach, R. Schneider, H. Stoermer, D. Gerthsen, U. Guntow, E. Ivers-Tiffée, A. Weber, C. Peters, and H. Yokokawa. *Journal of Materials Science*, 43(9):3135–3143, 2008.
- [49] J. Pagnaer, A. Hardy, D. Mondelaers, G. Vanhoyland, J. D’Haen, M. K. Van Bael, H. Van den Rul, J. Mullens, and L. C. Van Poucke. *Materials Science and Engineering, B: Solid-State Materials for Advanced Technology*, B118(1-3):79–83, 2005.
- [50] G. Westin, M. Ottoson, and A. Pohl. *Thin Solid Films*, 516(15):4673–4678, 2008.
- [51] H. J. Hwang, A. Towata, M. Awano, and K. Maeda. *Scripta Materialia*, 44(8/9):2173–2177, 2001.
- [52] B. J. Kim, J. Lee, and J. B. Yoo. *Thin Solid Films*, 341(1,2):13–17, 1999.
- [53] K.-S. Hwang, H.-M. Lee, S.-S. Min, and B.-A. Kang. *Journal of Sol-Gel Science and Technology*, 18(2):175–180, 2000.
- [54] L. M. Liu, T. H. Lee, L. Qiu, Y. L. Yang, and A. J. Jacobson. *Materials Research Bulletin*, 31 (1):29–35, 1996.
- [55] B. Fultz and J. M. Howe. *Transmission Electron Microscopy and Diffractometry of Materials*. Springer, Berlin, 3rd edition edition, 2007.
- [56] G. Binnig, C. F. Quate, and Ch. Gerber. Atomic force microscope. *Physical Review Letters*, 56(9):930 LP – 933, 1986.
- [57] D. Sarid. *Scanning Force Microscopy*. Oxford University Press, Oxford, 1994.

- [58] J. M. Walls. Cambridge University Press, Cambridge, UK, 1989.
- [59] M.; Pechini. Us patent. No.3.330.697, 1967.
- [60] X. Zhu, S. Li, X. Yang, and J. Qiu. *Applied Surface Science*, 254(2):532–537, 2007.
- [61] J. Fleig and A. Opitz. *Solid State Ionics*, 181:684–693, 2010.
- [62] L. J. van der Pauw. *Phillips Research Reports*, 13(1):1–9, 1958.
- [63] D. Grientschnig and W. Sitte. *Zeitschrift für Physikalische Chemie*, 168:134–159, 1990.
- [64] C. Peters, A. Weber, and E. Ivers-Tiffée. *Journal of the Electrochemical Society*, 155(7):B730–B737, 2008.
- [65] F. S. Baumann, J. Fleig, H.-U. Habermeier, and J. Maier. *Solid State Ionics*, 177:3187–3191, 2006.
- [66] M. Prestat, A. Infortuna, S. Korrodi, S. Rey-Mermet, P. Muralt, and L. J. Gauckler. *Journal of Electroceramics*, 18(1-2):111–120, 2007.
- [67] M. Sase, F. Hermes, K. Yashiro, K. Sato, J. Mizusaki, T. Kawada, N. Sakai, and H. Yokokawa. *Journal of the Electrochemical Society*, 155(8):B793–B797, 2008.
- [68] A. Ringuede and J. Fouletier. *Solid State Ionics*, 139:167–177, 2001.
- [69] A. Bieberle-Huetter, M. Sogaard, and H. L. Tuller. *Solid State Ionics*, 177(19-25):1969–1975, 2006.
- [70] W. Sitte, E. Bucher, and W. Preis. *Solid State Ionics*, 154-155:517–522, 2002.
- [71] X. Chen, N. J. Wu, D. L. Ritums, and A. Ignatiev. *Thin Solid Films*, 342:61–66, 1999.
- [72] X. Chen, N. Wu, A. Ignatiev, Z. Zhang, and W.-K. Chu. *Thin Solid Films*, 350(1,2):130–137, 1999.
- [73] D. Brodoceanu, A. Manousaki, I. Zergioti, A. Klini, M. Dinescu, and C. Fotakis. *Applied Physics A: Materials Science and Processing*, 79(4-6):911–914, 2004.
- [74] D. Waller, L. G. Coccia, J. A. Kilner, and I. W. Boyd. *Solid State Ionics*, 134(1,2):119–125, 2000.

- [75] N. Imanishi, Y. Sumiya, K. Yoshimura, T. Matsumura, A. Hirano, Y. Takeda, D. Mori, and R. Kanno. *Solid State Ionics*, 177(19-25):2165–2173, 2006.
- [76] S. P.; Jiang. *Journal of Solid State Electrochemistry*, 11:93–102, 2007.
- [77] A. A. Vance and S. McIntosh. *Journal of the Electrochemical Society*, 155(1):B1–B7, 2008.
- [78] M. Backhaus-Ricoult, K. Adib, T. St. Clair, B. Luerssen, L. Gregoratti, and A. Barinov. *Solid State Ionics*, 179(21-26):891–895, 2008.
- [79] M. Backhaus-Ricoult. *Solid State Sciences*, 10(6):670–688, 2008.
- [80] F. S. Baumann. *PhD thesis, MPI Stuttgart*, 2006.
- [81] N. Caillol, M. Pijolat, and E. Siebert. *Applied Surface Science*, 253(10):4641–4648, 2007.
- [82] M. Sase, D. Ueno, K. Yashiro, A. Kaimai, T. Kawada, and J. Mizusaki. *Journal of Physics and Chemistry of Solids*, 66(2-4):343–348, 2005.
- [83] S. P. Simmer, M. D. Anderson, M. H. Engelhard, and J. W. Stevenson. *Electrochemical and Solid-State Letters*, 9(10):A478–A481, 2006.
- [84] P. A. W. Van der Heide. *Surface and Interface Analysis*, 33:414–425, 2002.
- [85] C. A. F. Vaz, D. Prabhakaran, E. I. Altman, and V. E. Henrich. *Phys. Rev. B*, 80(15):155457, 2009.

List of Figures

1.1	SOFC concept-oxygen and hydrogen react via a dense, oxide ion-conducting electrolyte (YSZ or GDC). [24]	3
2.1	Schematic illustration of the surface path (a) and of the bulk path (b).	5
2.2	a) Perovskite structure b) Brownmillerite structure: Oxygen ions (white) in octahedral (O) and tetrahedral (T) coordination of the Co ions (black). Oxygen vacancies are shown as squares. [29]	7
2.3	Image of working PLD.	10
2.4	Equivalent circuit for a mixed conducting electrode on a solid electrolyte derived (a), simplified circuit (b) and circuit used in this thesis (c). [9]	14
2.5	Image of a microstructured sample contacted with tips.	15
3.1	Schematic illustration of the PLD process.	20
3.2	Schematic illustration of the sol-gel process.	21
3.3	Schematic illustration of the photolithography process. As prepared sample; spin coating of the photo resist; illumination under the UV lamp; sample before treatment with developer; sample after treatment with developing solution; ion beam etching; sample after etching; sample after removing the photo resist in acetone.	22
3.4	Cross-sectional view of an AFM image (a) and digital holographic microscope image of a sol-gel film consisting of three layers after microstructuring and chemical etching (b).	23
3.5	Sampling depth in XPS for different angles.	25
3.6	Impedance spectra of the same sample recorded at 500°C in an open set-up (red) and a closed set-up (black).	26
3.7	Schematic illustration of the microscopic set up.	26
3.8	Schematic illustration of the macroscopic set up.	27

4.1	X-ray diffraction (XRD) patterns of 200 nm LSC films deposited on single crystalline YSZ at 630°C (red and black) and 470°C (blue and green) before (red and blue) and after (black and green) heat treatment at 600°C for 72 h.	28
4.2	a) Scanning electron microscopy (SEM) images (cross-sectional and top views) of 200 nm LSC films deposited at 470°C before (top) and after (bottom) annealing for 72 h at 600°C. b) Scanning electron microscopy (SEM) images (cross-sectional and top views) of 200 nm LSC films deposited at 630°C before (top) and after (bottom) annealing for 72 h at 600°C.	30
4.3	SEM images of a 40 nm LSC film deposited at 520°C before (left) and after (right) annealing at 700°C 22 h.	31
4.4	SEM images of a 160 nm thick LSC film deposited at 420°C (a) and of a 270 nm thick LSC film deposited at 650°C (b).	31
4.5	SEM images of a 160 nm thick LSC film deposited at 420°C after an annealing of 500 hours at 600°C (a) and of a 270 nm thick LSC film deposited at 650°C after an annealing of 140 hours at 600°C (b).	32
4.6	FIB cut and cross-sectional view of a 360 nm LSC thin film deposited at 440°C.	32
4.7	3D AFM image of a PLD thin film deposited at 410°C (a) and at 610°C (b).	33
4.8	AFM images of a 40 nm LSC thin film deposited at 540°C (left) and 730°C (right).	33
4.9	AFM images of a 40 nm LSC thin film deposited at 540°C (left) and 730°C (right) after 20 hours at 700°C.	34
4.10	Cross section of the AFM images of a 40 nm LSC thin film deposited at 540°C (left) and 730°C (right) both after 20 hours at 700°C.	34
4.11	AFM images of a 40 nm LSC thin film deposited at 540°C as prepared (left), after +3 V (middle) and -3 V (right) for 15 minutes.	35
4.12	AFM images of a 40 nm LSC thin film deposited at 730°C as prepared (left), after +3 V (middle) and -3 V (right) for 15 minutes.	35
4.13	HRTEM image (a) and STEM image (b) of a 80 nm thick LSC film deposited at 440°C.	36
4.14	SAD pattern of 80 nm thick LSC films deposited at 440°C (a) and 720°C (b).	37

4.15	HRTEM image (a) and STEM image (b) of a LSC thin film deposited at 720°C.	37
4.16	HAADF STEM images with profile of 80 nm thick LSC films deposited at 440°C (a) and 720°C (b).	38
4.17	Impedance spectra recorded at 600°C on 200 nm LSC thin films deposited at 510°C (red) and 630°C (black) as prepared (a) and of thin films deposited at 500°C (black) and 630°C(red) after several hours at 600°C (b).	39
4.18	a) Schematic illustration of the oxygen reduction on LSC and b) complex and c) simplified equivalent circuits used to fit the data.	40
4.19	Area scaled impedance spectra of LSC electrodes deposited at 420°C measured microscopically (red) and macroscopically (black) at 600°C.	40
4.20	Dependence of the electrode resistance at 600°C on the deposition temperature for 200nm and 40nm films. (All measured macroscopically.)	41
4.21	Arrhenius plot of a LSC layer deposited at 420°C after 3 days at 600°C; measured macroscopically.	43
4.22	Arrhenius plot of a LSC layer deposited at 650°C; measured microscopically.	44
4.23	Arrhenius plot of a LSC layer deposited at 650°C after 3 days at 600°C; measured microscopically.	44
4.24	Arrhenius plot of YSZ (bulk resistance); measured macroscopically.	45
4.25	High-frequency intercept (R_b) of the impedance spectra in macro measurements at 600°C for 200 and 40nm LSC films deposited at different temperatures.	46
4.26	Electronic conductivity measured in van-der-Pauw geometry for a 470°C (white spots), 630°C (black spots), 340°C (white squares) deposited sample (320 nm) as a function of temperature.	47
4.27	Impedance spectra for 200 nm LSC electrodes deposited at 630°C recorded once per hour while keeping the sample at 600°C (macro measurements).	48
4.28	Degradation of the electrode resistance at 600°C for 40 nm LSC films deposited at temperatures between 250° and 650°C.	49
4.29	Degradation of the electrode resistance at 600°C for 200 nm LSC films deposited at temperatures between 230° and 670°C.	50
4.30	Degradation of the electrode resistance at 500°C, 600°C and 700°C of a 160 nm thick LSC film deposited at 420°C.	51
4.31	Degradation of the electrode resistance at 500°C, 600°C and 700°C of a 270 nm thick LSC film deposited at 650°C.	51

4.32	Electrode resistance as a function of time of a 40 nm thick LSC electrode deposited at 730°C and measured at 700°C. After 1200 minutes -2V were applied for 5 minutes.	53
4.33	a) Darkening of microelectrodes under the microscope b) Impedance spectra of a 40 nm thick LSC film deposited at 730°C and measured at 700°C as prepared and after applying bias.	54
4.34	a) Electrode resistance as a function of time at 600°C of a 40 nm 650° C deposited sample (black) and etched for 20 seconds with diluted HCl (red) (a) and corresponding impedance spectra (b); measured macroscopically.	56
4.35	Electrode resistance of a LSC thin film (deposited at 520°C, 40 nm) as a function of time at 600°C and etched for 10 and then for 20 seconds with diluted HCl (a) and corresponding impedance spectra (b); measured microscopically.	56
4.36	LEIS spectra recorded with 5 kV Ne primary ions.	58
4.37	LEIS spectra recorded with 3 kV He primary ions.	59
4.38	XRD pattern of LSC82 (blue) and LSC46 (green) deposited at 650°C on single crystalline YSZ.	61
4.39	Electrode resistance as a function of time at 600°C for LSC82, LSC64 and LSC46 thin films (around 200 nm) deposited at different temperatures; measured macroscopically.	62
4.40	Impedance spectra macroscopically recorded at 700°C on 200nm thick LSCF6437 film deposited at 550°C after 2 days at 600°C (a) and on a LSF thin film deposited at 550°C after 2 days at 700°C (b).	63
4.41	XRD pattern of a 700 nm thick LSC film deposited at 410°C on polycrystalline YSZ.	64
4.42	XRD pattern of a 1000 nm thick LSC film deposited at 410°C on polycrystalline GDC.	65
4.43	a) TEM image of a LSC thin film deposited on polycrystalline YSZ. b) SAD patterns of a LSC thin film deposited on polycrystalline YSZ (1 left, 2 right).	66
4.44	a) TEM image of a LSC thin film deposited on polycrystalline GDC. b) SAD patterns of a LSC thin film deposited on polycrystalline GDC (1 left, 2 right).	66
4.45	Impedance spectra of 150 nm thick LSC films on polycrystalline YSZ deposited at 350°C (a) and 650°C (b) measured at 600°C.	67

4.46	Impedance spectra of 150 nm thick LSC films deposited at 500°C on polycrystalline YSZ (a) and of 150 nm thick LSC films deposited at 350°C on polycrystalline GDC (b) both measured at 600°C.	68
4.47	Impedance spectra of 150 nm thick LSC films deposited at 500°C on polycrystalline GDC measured at 600°C after 2 (light green), 6 (black), 10 (blue), 14 (green) and 20 (red) hours.	69
4.48	Dependence of the electrode resistance at 600°C on the film deposition temperature for different substrates.	70
4.49	Electrode resistance as a function of time at 600°C for LSC thin films (ca. 100 nm) deposited at different temperatures on polycrystalline YSZ. . . .	70
4.50	Difference of two diffraction patterns of a LSC electrode (2 sol-gel deposited layer) annealed at 600°C for 3 minutes and after 3 days at 600°C; the linearized regions correspond to the single crystalline YSZ substrate.	71
4.51	AFM images of LSC electrode annealed for 3 minutes at 500°C (a) and 700°C (b).	72
4.52	AFM images of LSC electrodes consisting of one (a) and two (b) sol-gel prepared layers thin film annealed at 600°C for 3 minutes.	72
4.53	AFM image of a LSC electrode consisting of two sol-gel prepared layers annealed at 500°C for 3 minutes and then additional 3 days at 500°C.	73
4.54	SEM images of LSC electrodes consisting of one (a) and two (b) sol-gel prepared layers annealed at 600°C for 3 minutes.	73
4.55	SAD pattern of a LSC electrode (two-layered) annealed for 3 minutes at 600°C.	74
4.56	STEM image (a) and bright field image (b) of a two-layered LSC electrode annealed for 3 minutes at 600°C.	74
4.57	Impedance spectra of a LSC thin film (on single crystalline YSZ) annealed for 3 minutes at 500°C and measured at 500°C as prepared (green)(a), after 20 minutes at 600°C (blue), after 20 minutes at 600°C and 3 days at 500°C (red) (b). Bold lines are fit curves.	76
4.58	Impedance spectra of a LSC thin film on polycrystalline YSZ annealed at 600°C for 3 minutes and measured at 600°C after heating (green) and then every 2 minutes (blue, red). Spectra were recorded from high to low temperature with the loop indicating film changes during the measurement (a) and magnification of it (b).	78

4.59 Impedance spectra of a LSC thin film on polycrystalline GDC annealed at 600°C for 3 minutes and measured at 500°C as prepared (blue), after 20 minutes at 600°C (red), after 20 minutes at 600°C and 3 days at 500°C (green).	78
4.60 Sr/(Sr+La) ratio considering all Sr species.	82
4.61 (Sr+La)/Co ratio considering all Sr species.	82
4.62 (Sr 3d peak with contributions from lattice and surface Sr.	83
4.63 Sr/(Sr+La) ratio only considering surface Sr.	83
4.64 (Sr+La)/Co ratio only considering surface Sr.	84
4.65 Co peak shape comparison on the LSC films deposited at 450°C and 650°C indicating different Co oxidation states.	85

List of Tables

4.1	Electrode resistance values in Ωcm^2 of a sample deposited at 420°C . . .	53
4.2	Electrode resistance values in Ωcm^2 of a sample deposited at 650°C . . .	53
4.3	Electrode resistances in Ωcm^2 measured at 600°C of two 40 nm thick LSC samples deposited at 540°C and 730°C, before and after 20 hours at 700°C	54
4.4	Samples and sample numbers in the LEIS spectra (100 nm thickness) . .	57
4.5	Peak integrals of the Ne spectrum in counts/nC.	58
4.6	Peak integrals of the He spectrum in counts/nC	59
4.7	Electrode resistance in Ωcm^2 of different sol-gel samples measured at dif- ferent temperatures. (* after 15 minutes at 600°C)	79
4.8	XPS samples	81

8 Acknowledgment

Zuerst möchte ich natürlich meinem Betreuer Prof. Jürgen Fleig für die interessante Aufgabenstellung, die wissenschaftliche Anleitung und die Möglichkeit die Resultate auf vielen Kongressen einem internationalen Publikum vorzustellen, danken.

Auch unsere stetig wachsende und sich wandelnde Arbeitsgruppe hat sehr zum Erfolg dieser Arbeit beigetragen. Da wären die Urgesteine wie Martin, Elmar, Alex, Matthias und Till, aber auch "jüngere" Kollegen wie Lukas, Steffi, Markus und einige andere, denen ich zu Dank für Hilfe in praktischen Dingen, Diskussionen, eine lustige Konferenzbegleitung und schöne Gespräche dankbar bin. Auch dem Team im Sekretariat und natürlich Udo und Kurt bin ich für ihre Unterstützung, aber auch ihren Humor dankbar.

Natürlich möchte ich mich auch herzlich bei Michael Stöger-Pollach und Johannes Bernardi für die gute Zusammenarbeit mit dem USTEM bedanken. Besonders Michael war mir eine grosse Hilfe bei meinen TEM Untersuchungen. Gernot Friedbacher danke ich für die Hilfe am AFM und die netten Gespräche, Elisabeth Eitenberger für die kompetente, schnelle und nette Hilfe am REM, Frank Kubel für die vielen XRD Messungen und deren Auswertungen.

Prof. Werner Sitte und Dr. Edith Bucher möchte ich für die aufschlussreichen van-der-Pauw-Messungen danken, die meine Ergebnisse sehr schön abgerundet haben. Ein weiterer Dank geht auch an die Firma IONTOF, die sich bereit erklärt hat einige unserer Proben mit LEIS zu untersuchen.

Thank you also to Prof. Bilge Yildiz for inviting me to MIT. It was a pleasure to work together with you. Thank you also to Zhuhua for all her work and for feeling me welcome. It was a great stay and I hope we will keep in touch.

Und natürlich sei auch meinen Eltern und meinem Bruder Markus für ihre Unterstützung und Liebe gedankt.

Zu allerletzt, wie es eben immer ist, möchte ich aber einem weiteren Urgestein unserer Arbeitsgruppe, der aber in den letzten drei Jahren nur noch an meiner Seite und nicht mehr in der Gruppe tätig war, danken.

Danke, David, für deine Liebe, Unterstützung und v.a. Geduld mit mir. Ich hoffe wir meistern die Zukunft genauso.

9 Curriculum vitae

Contact Information

Name: Dipl.-Ing. Judith Januschewsky

Adresse: Pilgramgasse 22/2/30, A-1050 Wien

Telephone: +43 650 4320940

E-mail: j.januschewsky@tuwien.ac.at

Personal Information

Date of Birth: June 7th 1984

Place of Birth: Salzburg/Austria

Citizenship: Austria

Employment History and Education

Jan 2009- Jan 2011	Employed as University Assistant of Prof. J. Fleig, Institute of Chemical Technologies and Analytics (E164), Vienna UT. PhD thesis.
Nov 19 th 2007	Finished Dipl.-Ing. Studies in Chemistry, Concentrations: Metallurgy.
Jan-Nov 2007	Diploma Thesis: "Synthese und Charakterisierung von Nanostrukturen aus Wolfram-, und Molybdänoxiden auf Silizium". Advisor: Ass. Prof. Dr. C. Edtmaier and Prof. W.-D. Schubert, Institute of Chemical Technologies and Analytics (E164), Vienna UT.
June 19 th 2006	Second diploma examination in Chemistry.
Nov 24 th 2003	First diploma examination in Chemistry.
Oct 2002-2007	Study of Technical Chemistry at the Vienna University of Technology, Austria.
June 20 th 2002	A-Levels with distinction.
1998-2002	Participant in the Chemistry Olympiad.
1994-2002	Secondary School Nonntal in Salzburg/Austria.
1990-1994	Elementary School Plainfeld/Salzburg/Austria.